creative commons

C O M M O N S D E E D

저작자표시-비영리-변경금지 2.0 대한민국

이용자는 아래의 조건을 따르는 경우에 한하여 자유롭게

- 이 저작물을 복제, 배포, 전송, 전시, 공연 및 방송할 수 있습니다.

다음과 같은 조건을 따라야 합니다:

저작자표시. 귀하는 원저작자를 표시하여야 합니다.

비영리. 귀하는 이 저작물을 영리 목적으로 이용할 수 없습니다.

변경금지. 귀하는 이 저작물을 개작, 변형 또는 가공할 수 없습니다.

- 귀하는, 이 저작물의 재이용이나 배포의 경우, 이 저작물에 적용된 이용허락조건을 명확하게 나타내어야 합니다.
- 저작권자로부터 별도의 허가를 받으면 이러한 조건들은 적용되지 않습니다.

저작권법에 따른 이용자의 권리는 위의 내용에 의하여 영향을 받지 않습니다.

이것은 이용허락규약(Legal Code)을 이해하기 쉽게 요약한 것입니다.

Disclaimer

dCollection

이학박사 학위논문

Plasmonic Nanoparticles on Lipid Bilayer for Nano-Bio Detection and Computing

지질 이중층 상 플라즈모닉 나노입자 기반 나노바이오 검지 및 컴퓨팅

2019년 2월

서울대학교 대학원

화학부 무기화학

김 선 기

Plasmonic Nanoparticles on Lipid Bilayer for Nano-Bio Detection and Computing

지도교수 남좌민

이 논문을 이학박사 학위논문으로 제출함
2018년 12월

서울대학교 대학원
화학부 무기화학
김선기

김선기의 이학박사 학위논문을 인준함
2018년 12월

위원장 이동환 (인)

부위원장 남좌민 (인)

위원 김성근 (인)

위원 김지환 (인)

위원 이진석 (인)

Abstract

Plasmonic Nanoparticles on Lipid Bilayer for Nano-Bio Detection and Computing

Sungi Kim
Department of Chemistry
The Graduate School
Seoul National University

Supported lipid bilayer is a two-dimensional lipid bilayer self-assembled on a hydrophilic substrate with two-dimensional fluidity. By introducing plasmonic nanoparticles with strong scattering signals into the supported lipid bilayer, it is possible to observe and track thousands of nanoparticles and their interactions at a single-nanoparticle level in real time. In this thesis, I expand the nanoparticle-lipid bilayer platform by engineering plasmonic nanoparticles to construct a complex nanoparticle network system and develop multiplexed bio-detection and bio-computing strategies.

Chapter 1 describes a supported lipid bilayer platform incorporating plasmonic nanoparticles. Section 1 introduces the optical properties and biosensing application of plasmonic nanoparticles, and Section 2 introduces tethering technique, characteristics, and advantages for introducing nanoparticles into supported lipid bilayer platforms. In Chapter 2, I introduce a system that can distinguish nine types of nanoparticle assembly reactions occurring simultaneously by introducing optically encoded plasmonic nanoparticles that scatter red, blue, and green light into supported lipid bilayers. I performed multiplexed detection of nine types of microRNAs, which are important gene regulators and cancer cell biomarker. In Chapter 3, I develop a bio-computing platform that recognizes molecular inputs, performs logic circuits, and generates nanoparticle assembly/disassembly output signals. Complex logic circuits are designed and implemented by combining two strategies: (i) interfacial design that constructs a logic circuit through DNA functionalization of the interface of nanoparticles, and (ii) a network design that connects assembly/disassembly reactions. In Chapter 4, I develop a bio-computing calculator capable of performing arithmetic logic operations. I use the nanoparticle-lipid bilayer platform as the hardware that stores, processes, and outputs information, and constructs software that contains logic circuit functions through DNA solution. An information storage nanoparticle stores solution-phase molecular input signals on the surface of nanoparticles. The bio-computing lipid nanotablet recognizes an arithmetic logic circuit programmed with DNA information and generates outputs a result of a kinetic difference between nanoparticle assembly reaction according to the storage state of the input signal.

Keywords: supported lipid bilayer, plasmonic nanoparticle, multiplexed detection, molecular computing, nanoparticle network

Student Number: 2013-20258

Table of Contents

Chapter 1. Introduction: Plasmonic Nanoparticle-Tethered Supported Lipid Bilayer Platform 1

1.1. Plasmonic Nanoparticles and Their Bio-Applications 2
1.1.1. Introduction 4
1.1.2. Fundamentals of Plasmonic Nanoparticles 8
1.1.3. Plasmonic Nanoparticle Engineering for Biological Application 11
1.1.4. Plasmonic Nanoparticles for Rayleigh Scattering-Based Biosensing 16
1.1.5. References 21

1. 2. Supported Lipid Bilayer as a Dynamic Platform 24
1.2.1. Introduction 26
1.2.2. Basic Setups and Strategies 29
1.2.3. Nanoparticle-Tethering Techniques 33
1.2.4. Real-Time Imaging and Tracking of Single Nanoparticles on SLB 39
1.2.5. Observation of Interactions between Single Nanoparticles 44
1.2.6. References 50

Chapter 2. Multiplexed Biomolecular Detection Strategy 53
2.1. Introduction 55
2.2. Experimental Section 60
2.3. Results and Discussion 66
2.4. Conclusion 77
2.5. Supporting Information 79
2.6. References 83

Chapter 3. Nano-Bio Computing on Lipid Bilayer 84
3.1. Introduction 85
3.2. Experimental Section 88
3.3. Results and Discussion 98
3.4. Conclusion 120
3.5. Supporting Information 124
3.6. References 161

Chapter 4. Development of Nanoparticle Architecture for Biomolecular Arithmetic Logic Operation 163
4.1. Introduction 165
4.2. Experimental Section 167
4.3. Results and Discussion 171
4.4. Conclusion 177
4.5. References 179

Abstract in Korean 180

Chapter 1

Introduction: Plasmonic Nanoparticle-Tethered Supported Lipid Bilayer Platform

1.1. Plasmonic Nanoparticles and Their Bio-Applications

Metal nanoparticles, whose size is smaller than the wavelength of light, exhibit unique optical properties from their properties in bulk scale. When they interact with light inside dielectric medium, free electrons move collectively in one direction, creating an electric dipole moment. This, in turn, generates a restoring force and induces oscillation of free electrons. Delocalized free electrons is called surface plasmon and the coherent oscillation of electrons is called localized surface plasmon resonance (LSPR).

Plasmonic nanoparticles are useful for harnessing light and enhancing near field through strong light-matter interaction, thus providing diverse optical properties. Their properties can be tuned by changing the size, shape and composition, and further inducing plasmonic coupling via particle assembly. Among them, noble metal nanoparticles, gold and silver nanoparticles, are intriguing material for biological application because of their strong LSPR in visible region, structural controllability, high stability, and facile surface modification. In this section, I will introduce the basics of plasmonic nanoparticles and their application using scattering properties.

Chapter 1.1 was published in part as:

Sungi Kim+, Jae-Myoung Kim+, Jeong-Eun Park+, Jwa-Min Nam, "Nonnoble-Metal-Based Plasmonic Nanomaterials: Recent Advances and Future Perspectives." *Adv. Mater.* 30, 1704528 (2018) and

Amit Kumar, Sungi Kim, Jwa-Min Nam, “Plasmonically Engineered Nanoprobes for Biomedical Application” *J. Am. Chem. Soc.* 131, 14509-14525 (2016).

+ represents equal contribution.

1.1.1 Introduction

Many of metal nanoparticles (NPs) such as AuNPs, AgNPs and CuNPs possess promising properties such as high surface area, controllability of a variety of nanoscale structural features and availability of conjugation sites on surface. More interestingly, these metal NPs can confine and amplify the light within an ultrasmall volume of a particle due to the localization and coupling of surface plasmons (collective oscillation of free electrons) with electromagnetic waves [this is called as the localized surface plasmon resonance (LSPR)] (1). Augmented electromagnetic field near the surface of a metal NP modulates and promotes a variety of physicochemical processes and applications such as nonlinear optics (2), surface-enhanced vibrational spectroscopies (3), photovoltaics (4), metamaterials (5), photothermal transduction (6), plasmonic catalysis (7), and “hot electron-hole” pair generation (8). In particular, these NPs are quite useful for biomedical applications. In this regard, these particles provide strong, controllable optical properties, high controllability in composition and structure, availability of various synthetic schemes in forming targeted nanostructures in a high yield, reliable bioconjugation chemistries, implantability of multifunctionality in a single particle, high stability, and biocompatibility (9). Among these, designing and tuning the plasmonic properties of these particles, including enhanced optical, photothermal and photoacoustic properties have been of special interest recently. However, precise engineering of these plasmonic properties on nanometer (nm) scale and designing principles of these plasmonic bioprobes for the clinical applications are still ongoing subjects and under heavy scrutiny (10).

The LSPR-dependent properties can be engineered based on the judicious selection of the size, shape, composition and coupling of plasmonic NPs. Syntheses and proper use of such plasmonically engineered nanoprobes based on the detailed, correct understanding of these probes for a specific biomedical application are key to successful development of plasmonic bioprobes (11). In deciding the plasmonic properties, nanoscale structural features such as junction, hollowness, sharp edge, pointed tip, flat interface and symmetry along with strong plasmonic coupling-inducing plasmonic nanogap are critical and allow for controlling the plasmonic properties and augmenting the electromagnetic field of plasmonic nanostructures (12). Further, small organic molecules, surfactants, polymers, biomolecules such as DNA and proteins and DNA origamis have been utilized to modulate and facilitate the formation of targeted structures with targeted plasmonic features, and these cause crystallographic surface strain for lattice mismatch and different metal growth kinetics (13). It should be noted that inter-particle distances between plasmonic NPs or plasmonic gap size and shape largely affect the plasmonic properties. Controlling these distances on nm or sub-nm scale is critical for tuning their optical and other plasmonic properties (11). Another important part is the symmetry of nanostructures, and the symmetry breaking of plasmonic nanoparticles can generate higher electromagnetic field, multipolar plasmon modes and new plasmonic properties such as Fano resonances and plasmon-induced transparency (14). From the perspective of synthetic accessibility of many different plasmonic nanostructures, the intrinsic crystallographic symmetry of NP seeds normally exhibits epitaxial symmetrical growth. However, playing with factors such as morphology, reducing agents, crystallographic mismatch, choice of the capping ligands, and control of kinetic and thermodynamic conditions can result in various non-spherical, asymmetric structures (15, 16). Further, biomolecule-mediated assemblies of plasmonic nanoparticles into chiral configurations give rise to the chiroplasmonic response that can be used as a highly sensitive and selective signaling tool for biodetection (17, 18). Also, the shift in chiroplasmonic absorption wavelength upon interaction with chiral biomolecules such as proteins gives secondary and tertiary structural in-formation (19).

Designing and integrating nanoprobes with plasmon-induced beneficial features for biomedical applications is a challenging task due the complexity in structure design, synthesis and understanding in the properties for a variety of applications under different in vitro and environments in (Figure 1) (20, 21). This challenging goal, designing, synthesizing and validating plasmonic nanoparticles for a specific application are of foremost importance. In this section, I provide basic concepts of plasmonic nanostructures, and review their Rayleigh scattering-based application for biological labels and biosensing.

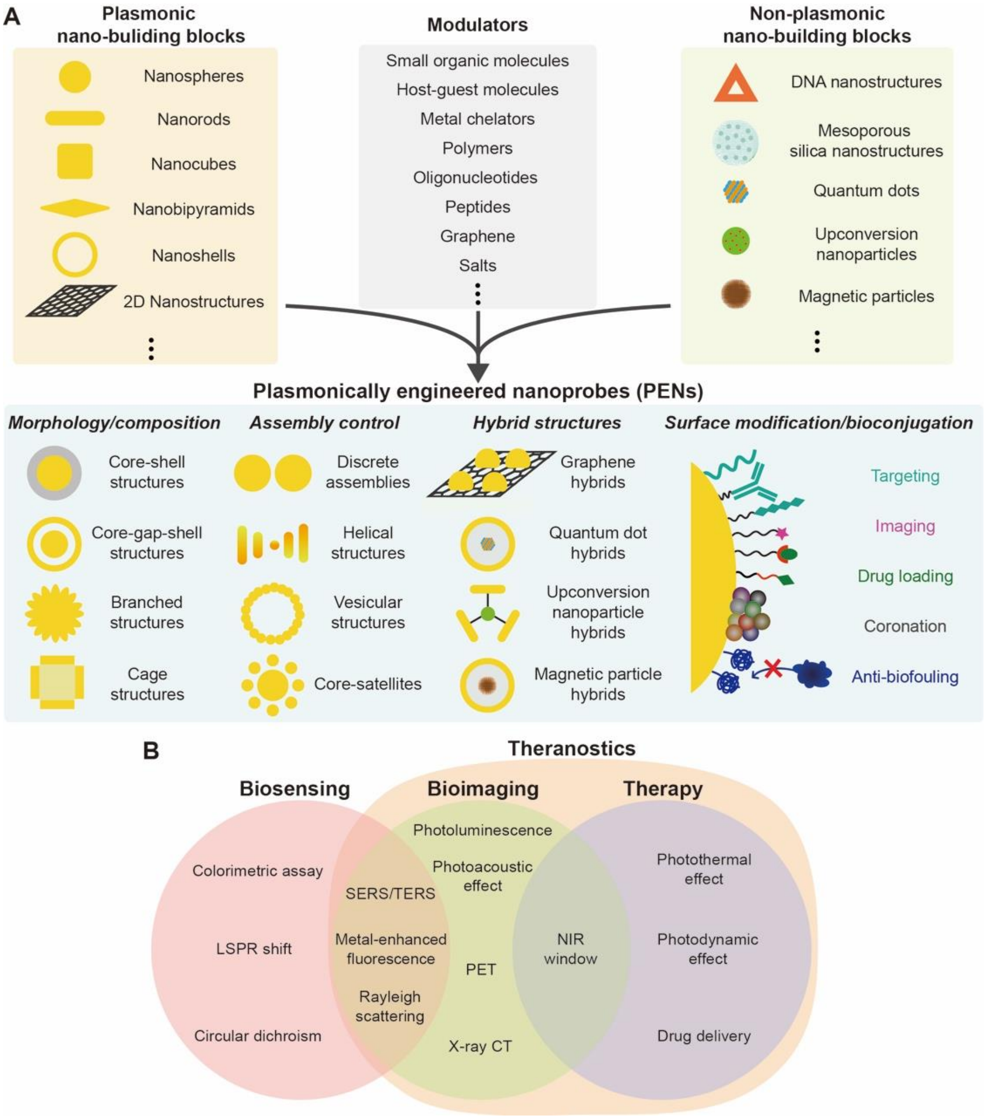

Figure 1. Plasmonically engineered nanoprobes for biomedical applications. (a) Tuning and combining plasmonic building blocks, non-plasmonic building blocks and modulators and formation of plasmonic nanoprobes via engineering particle morphology, composition, assembly, hybrid and surface modification and bioconjugation. (b) Representative biomedical applications of plasmonic nanoprobes.

1.1.2. Fundamentals of Plasmonic Nanoparticles

Dielectric function, the ability of material to resist an electric flux, describes the interaction between light and matter. The complex dielectric function of a metal depends on the response of electrons with an external electromagnetic wave. This yields the dielectric function as a function of the incident light frequency ω, can be represented by a combination of three components: dielectric constant for infinite frequency (ε_∞), intraband transition contribution ($\varepsilon_{intra}(\omega)$), and interband transition contribution ($\varepsilon_{inter}(\omega)$).

$$\varepsilon(\omega) = \varepsilon_\infty + \varepsilon_{intra}(\omega) + \varepsilon_{inter}(\omega) \qquad (1)$$

The intraband transition is an electronic transition within the conduction band and can be described by the Drude model, which treats the conduction electrons as free electron gas. The interband transition is an electronic transition between the valence band and the conduction band, which can be explained by Lorentz oscillators. Using a combination of these models, the dielectric function can be described as

$$\varepsilon(\omega) = \varepsilon_\infty - \frac{\omega_p^2}{\omega(\omega + i\gamma)} + \frac{G_0\omega_0^2}{\omega_0^2 - \omega^2 - i\Gamma\omega} = \varepsilon_r(\omega) + i\varepsilon_i(\omega) \qquad (2)$$

where γ is the Drude decay constant, ω_p is the Drude plasma frequency which is proportional to the square root of density of free electrons, G_0 is the oscillator strength, ω_0 is the resonance frequency, and Γ is the Lorentz decay constant.

That can be written as a combination of $\varepsilon_r(\omega)$ that corresponds to the real part of the dielectric constant, and $\varepsilon_i(\omega)$ that corresponds to the imaginary part. The real part of the dielectric function describes the extent of polarization by an external electric field, and the imaginary part of the dielectric function describes the loss and absorption of metal. The interband transition mainly contribute to the imaginary part of the dielectric constant which induces significant damping and hampers efficient plasmonic behavior.

Mie theory describes an optical behavior of a spherical particle by an analytical calculation of Maxwell's equations using the dielectric constants of the particles and the surrounding medium at specific wavelength. According to the Mie theory, the quasistatic extinction cross-section (C_{ext}) of a spherical particle is given by

$$C_{ext}(\omega) = \frac{12\pi\omega R^3 {\varepsilon_m}^{3/2}}{c} \frac{\varepsilon_i(\omega)}{(\varepsilon_r(\omega)+2\varepsilon_m)^2+\varepsilon_i(\omega)^2} \qquad (3)$$

where ε_m is the dielectric constant of the medium, *c* is the speed of light, and *R* is the particle radius. Thus, the optical extinction of a spherical metal nanoparticle has maximum at the dipolar resonance condition at $\varepsilon_r(\omega) = -2\varepsilon_m$. The spectral position of plasmonic resonance of metal is determined by the real part of the dielectric function, while the imaginary part determines the spectral line width. The efficient plasmonic extinction of a nanoparticle is generated with large negative $\varepsilon_r(\omega)$ and small $\varepsilon_i(\omega)$ values.

As described above, the intrinsic dielectric function of metal determines the plasmonic and optical properties of nanoparticles. Metal nanoparticles exhibit a negative real dielectric function over a wide frequency range due to containing a large number of free electrons, showing plasmonic responses in UV to near-infrared (NIR) range. Au and Ag offering high-quality-factor plasmonic performance in the visible range. Au exhibits negative $\varepsilon_r(\omega)$ above 480 nm and relatively small $\varepsilon_i(\omega)$ window from 500 nm to 800 nm for exhibiting plasmonic properties. Au suffers from relatively high $\varepsilon_i(\omega)$ at wavelengths below 500 nm due to the occurrence of interband transitions, whereas Ag exhibits negative $\varepsilon_r(\omega)$ and small $\varepsilon_i(\omega)$ values above 320 nm, enabling effective plasmonic behavior throughout the visible region**.**

1.1.3. Plasmonic Nanoparticle Engineering for Biological Application

Well-defined assemblies of plasmonic NPs where individual nanostructures such as spherical NPs and AuNRs are grouped in particular orientations and with definite inter-particle distances are more challenging and have a larger scope and usage in a variety of applications including biosensing and bioimaging (Figures 1a and 1b) (22). Typically, the close assembly of NPs where inter-particle spacing is less than 2.5 times the particle diameter causes plasmonic coupling (23, 24). Generating and controlling a nm gap between two NP units in plasmonic nanoparticle assemblies is crucial for harnessing ultra-strong electromagnetic field through plasmonic coupling. For this purpose, DNA (25), bifunctional organic ligands (26), streptavidin-biotin conjugate (27), thin layer of polymer (28), silica coating (29) and single-layered graphene (30) have been used as nanoscale molecular separators. Plasmonic coupling between metallic nanostructures can be understood by the analogy of atomic orbital coupling leading to molecular orbitals (31). This plasmon hybridization model can be used to simulate complex nanostructures by theoretically disintegrating them in to simple constituent structures and hybridizing the plasmon modes of each geometry. The optical properties of multimeric systems can also be influenced by the symmetries and orientations of individual NPs (32, 33). A periodic chart of plasmonic NPs can be designated as ‘plasmonic atoms’ in different rows and columns, taking their shapes and geometrical parameters into account (11, 34). The assembly of such plasmonic atoms results in the formation of organized nanostructures (plasmonic molecules) under energetically favorable conditions, with the effect of directing agents/templates and/or by externally applying other stimuli such as forces (electrostatic, magnetic, flow, etc.) (13, 35). This assembly can be applied to build, tune and alter the nanostructures and their corresponding plasmonic properties.

For bio-applications of plasmonic nanoparticles, particle surface modification and bioconjugation chemistry should be considered (Figure 1a). Understanding and engineering organic corona around plasmonic NPs is critical for providing the desired functionalities on the surface for various plasmonic nanoparticles and eventual in vivo fate of plasmonic nanoparticles. The structural features of stabilizing organic ligands on metal NPs play very important roles in their directed assembly and particle stability, and specific intermolecular interactions such as hydrogen bonding and electrostatic interactions among organic ligands affect aggregation, self-assembly and targeting of plasmonic nanoparticles. Metal NP building blocks resulting from site-selective functionalization with a desired number of organic ligands on particle surface are profoundly useful for making targeted plasmonic nanoparticles accessible in a high yield (36).

Highly designable and tunable biomolecules can be used as synthetic modulators and templates for plasmonic nanoparticles. Among them, single-stranded DNA (ssDNA) has been extensively used as ligands for well-defined and controllable 1D, 2D, and 3D plasmonic assemblies. This is because ssDNA enables tuning of the number of DNA strands on each metal NP building block, base sequence, length/structure of oligonucleotides and modification of functional moieties such as thiol and fluorophore (37-39). DNA molecules can serve as programmable ligands to fine-tune the morphologies of nanomaterials depending on the shape of the seed and sequence of DNA used (40-42). DNA molecules were found to play important roles by influencing diffusion of the Au precursor to the seed and modulating the growth through differences in DNA desorption, density, and mobility on the seed surface. It was also reported binding of a thiolated DNA, modified on AuNPs-surface can facilitate the formation of an interior nanogap while forming Au shells on DNA-modified AuNPs (43). Thiolated DNA-modified AuNPs have also been used to form Au–Ag head–body nanosnowman structures (44). The nanojunction between Au head and Ag body can be finely tuned by varying the salt conditions and amount of Ag precursor, respectively. It was also shown that DNA strands can self-assemble into a stiff “nanomold” that contains a user-specified 3D cavity and encloses a nucleating gold “seed” (45). Under mild conditions, this seed grows into a larger cast structure that fills and thus replicates the cavity, resulting in a metallic nanostructure of chosen shape and size. Another more intuitive method for constructing plasmonic nanostructures is to assemble isolated plasmonic NPs (plasmonic atoms) into well-defined discrete assemblies (plasmonic molecules) with close inter-particle distances in specific configurations. DNA serves as an ideal connector or bond between plasmonic atoms for such assemblies because of its highly specific and controllable molecular recognition capability and controllable length (11, 25, 46).

Further, advancements in DNA nanotechnology have resulted in the generation of a variety of DNA superstructures solely from DNA, utilizing the DNA tiles and DNA origamis, and these DNA nanostructures can act as ‘template networks’ for the well-defined assembly of metal NPs (46-48). Recently, specifically designed 2D DNA origami has been utilized to develop a precise and removable templating platform that can transfer 2D oligonucleotide patterns onto the surface of AuNPs through an engineered toehold-initiated DNA displacement reaction (49). This strategy can be used to precisely control the number of valence and valence angles of AuNPs, and, further, these DNA-decorated AuNPs act as precursors for the construction of discrete AuNP clusters with desired configurations. Assembling plasmonic NPs into stereospecific 3D chiral configurations has wide applications in developing new classes of metamaterials and advanced biosensing platforms for chiral biomolecules. Recently, a 2D DNA origami template with an ‘X’ arrangement of DNA capturing strands on both sides was utilized to assemble AuNRs into left-handed and right-handed AuNR helices (50). Toroidal-shape chiral metamolecules, constructed from origami and spherical plasmonic NPs, showed strong chiroptical properties (51). A walking plasmonic AuNR was demonstrated on DNA origami as an active plasmonic system, in which AuNR with DNA strand feet can execute directional, progressive, and reverse nanoscale walking on a 2D or 3D DNA origami platform (52, 53). This plasmonic system may be useful for imaging dynamic biological phenomenon, which requires controlled motion at the nanoscale level, which is well below the optical diffraction limit. DNA aptamers can also act as targeting moieties that can specifically bind to one type of cell (54). More complex biomolecules such as peptides and their self-assembled supramolecular structures exhibit a wide range of functional groups and, depending on their amino acid sequences, can be used to both synthesize and assemble isotropic and anisotropic metal nanostructures in a controllable manner (55-60). Recently, peptides of different chiralities have been used to artificially create chiroplasmonic responses in AuNPs through peptide−NP interactions (61, 62).

1.1.4. Plasmonic Nanoparticles for Rayleigh Scattering-Based Biosensing

Multifunctional probes for ultrasensitive detection of multiple disease biomarkers have always been in demand. Among the various biosensing methods, nanotechnology-based optical biosensors, especially with plasmonic nanostructures, have drawn substantial interest (63, 64). In addition to the common advantages of nanotechnology-based sensors such as large surface area, versatile surface chemistry for bioconjugation, and biocompatibility, plasmonic nanoparticles have built-in signal transduction features because of their tunable LSPR-induced field enhancement, absorption, and scattering properties and targets can be detected with high sensitivity and selectivity, often in a multiplexed manner. Importantly, signal transduction for biosensing and biochemical applications can be well-controlled by tuning the size, shape and assembly of the plasmonic nanoparticles. In this section, we describe recent advancements in biosensing methods involving plasmonic nanoparticles based on their LSPR, light scattering.

Due to strong, controllable plasmonic coupling and large light absorption and scattering cross-section, plasmonic nanoparticles have been utilized as intense signal-generating labels for immunoassays, biochemical plasmonic sensors (65, 66). Biomolecule-mediated structural modification, assembly/disassembly or change in dielectric environment of plasmonic nanoparticles can cause shift in LSPR absorption wavelength and such label-free LSPR-based assays can be readily utilized for biosensing applications. Distance-dependent plasmonic coupling between metal nanostructures and corresponding change in light scattering properties has been exploited for characterizing and imaging biochemical processes, biomolecular interactions and specific bioreceptor-expressions (27).

Plasmonic nanoparticles can exhibit intense and controllable Rayleigh light scattering properties, and scattering cross-sections can be tuned by the shape and size of particles and the extent of plasmonic coupling. Two or more plasmonic NPs can be coupled together using biomolecules such as DNA or pep-tides, where the length of connecting molecules is the main factor in determining the distance between NPs. When two plasmonic NPs are brought into close proximity, the surface plasmon resonances of the individual NPs will couple, generating a light scattering spectrum that depends on their inter-particle distance (27). Light confinement in nanometer-scale volume by plasmonic nanoparticles allows for high spatial resolution up to the single-molecule level because of the large scattering cross-section of metal NPs and resulting high intensity of the scattered spectrum. The light scattering spectrum is typically time-invariant and can be continuously acquired in real-time for long imaging periods. These signals can be detected with dark-field microscopy, where non-scattered light is removed to build an image only with scattered wave components against dark background. In contrast, conventional fluorescence-based single-molecule methods are prone to photo-bleaching, blinking, and low signal-to-noise ratios.

A pair of $Zn_{0.4}Fe_{2.6}O_4$@SiO_2@Au core-shell plasmonic NPs connected by a caspase-3 cleavage peptide sequence was used to monitor anti-cancer drug-induced caspase-3 activity during apoptosis (Figure 2a) (67). The use of dielectric core

($Zn_{0.4}Fe_{2.6}O_4$@SiO_2)-shell (Au) structure provided more intense light scattering compared to solid AuNPs, and the magnetic core helped in purification during plasmonic ruler assembly. Caspase-3 activity was monitored by the decrease in light scattering intensity upon increase in inter-particle distance and diminishing plasmonic coupling.

The expression levels of cell surface receptors play crucial roles in cell signaling under normal or disease conditions and can act as diagnostic hallmarks for a number of diseases. One of the most interesting applications of plasmonic nanoparticles is the detection and quantification of cell membrane receptors on sub-diffraction limit length scales (68-70). Reinhard et al. successfully quantified the transmembrane proteins $ErbB_1$ and $ErbB_2$ in a variety of cancer cell lines using 40-nm AuNP immuno-labels exhibiting inter-particle distance-dependent differential plasmonic coupling upon increasing receptor density (71). Upon increasing receptor density, AuNPs were positioned very close to each other within a strong plasmonic coupling interparticle distance range (<5 nm), causing detectable wavelength red-shifts and enhancements in the intensity of scattered light. The information regarding the expression of these transmembrane proteins is crucial for monitoring and diagnosing various malignancies. In another report by Coronado et al., 90-nm AuNP immunolabels were used to determine the distribution and quantification of density of metabotropic glutamate receptor 1a on neuron cells at the sub-cellular scale (72). In a recent report by Irudayaraj et al., plasmonic nanoprobes (50 nm Au and Ag NPs) were used for single-cell quantitative epigenetic profiling (73). Utilizing hyper-spectral dark-field imaging, the detection of low-level cytosine modifications under different conditions, such as in different cell lines, at different cell phases, and even on a single chromosome, was achieved. Unlike fluorescence-based imaging methods, plasmonic nanoparticle-based methodology effectively circumvents limitations such as low resolutions, signal instability and complex instrumentation.

The research groups of Bissell and Alivisatos reported a reversible plasmon ruler, comprised of coupled AuNPs (30 nm) linked by a single aptamer (MMP-3 aptamer), capable of binding individual cell-secreted molecules (MMP-3) with high specificity (74). Quantification of secreted single molecules from cells, such as growth factors, proteases, and morphogens, within 3D cellular microenvironments can provide insight into how tissues form and become patterned during development and may suggest therapeutic strategies for repairing diseased tissues. plasmonic nanoparticle light scattering tags offer such a simple, convenient and reliable method for observing single molecules and corresponding biochemical events using relatively cheap bench-top dark-field microscopy setups, which are typically quite challenging to achieve. However, more advanced plasmonic nanoparticle probes should be designed and synthesized with better sensitivity, improved data reproducibility and multiple light-scattering color profiles, and well-controllable, reliable bioconjugation chemistry for varying nanostructures is needed to exploit the multiplexing capability of light-scattering plasmonic nanoparticles.

Fan group recently utilized the plasmonic nanoparticle as an optical label to study endocytosis and intracellular trafficking process inside the cell (Figure 2b). (75) They probe the intracellular transport and the clustering state by monitoring strong scattering signal and fluorescent signal of individual DNA-modified gold nanoparticles. The plasmonic nanoprobes showed multiple pathway for endocytosis process. Gold nanoparticles initially enters cell in the monomeric form and they get clustered as the vesicular transport matures from the early endosome to lysosome.

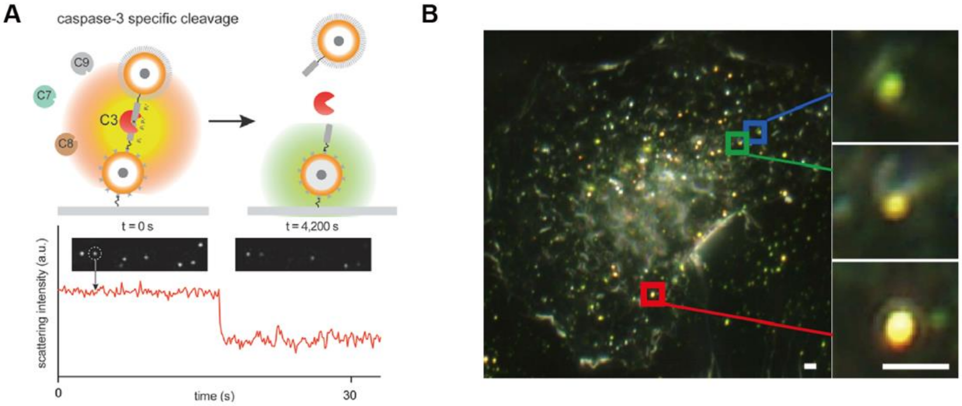

Figure 2. (a) Dark-field scattering-based monitoring of apoptotic drug-induced caspase-3 activity in leukemiacaspase-3 by selective cleavage of peptide linking $ZnO \cdot 4Fe_2 \cdot 6O_4@SiO_2@Au$ core-shell plasmonic NPs. (b) A representative dark-field microscopy image of the single plasmonic nanoparticles (blue rectangle), small clusters (green rectangle) and large clusters (red rectangle) inside the living cell. Scale bar, 2 μm.

1.1.5. References

1. Halas, N. J.; Lal, S.; Chang, W.-S.; Link, S.; Nordlander, P. *Chem. Rev.* **2011**, *111*, 3913−3961.
2. Kauranen, M.; Zayats, A. V. Nat. Photonics 2012, **6**, 737−748.
3. Wang, H.; Kundu, J.; Halas, N. J. *Angew. Chem., Int. Ed.* **2007**, *46*, 9040−9044.
4. Atwater, H. A.; Polman, A. *Nat. Mater.* **2010**, *9*, 205−213.
5. Luk'yanchuk, B.; Zheludev, N. I.; Maier, S. A.; Halas, N. J.; Nordlander, P.; Giessen, H.; Chong, C. T. *Nat. Mater.* **2010**, *9*, 707−715.
6. Herzog, J. B.; Knight, M. W.; Natelson, D. *Nano Lett.* **2014**, *14*, 499−503.
7. Christopher, P.; Xin, H.; Linic, S. *Nat. Chem.* **2011**, *3*, 467−472.
8. Brongersma, M. L.; Halas, N. J.; Nordlander, P. *Nat. Nanotechnol*. **2015**, *10*, 25−34.
9. Howes, P. D.; Rana, S.; Stevens, M. M. *Chem. Soc. Rev.* **2014**, *43*, 3835−3853.
10. Zhou, W.; Gao, X.; Liu, D.; Chen, X. *Chem. Rev.* **2015**, *115*, 10575−10636.
11. Tan, S. J.; Campolongo, M. J.; Luo, D.; Cheng, W. *Nat. Nanotechnol.* **2011**, *6*, 268−276.
12. Zhang, N.; Liu, Y. J.; Yang, J.; Su, X.; Deng, J.; Chum, C. C.; Hong, M.; Teng, J. *Nanoscale* **2014**, *6*, 1416−1422.
13. Jones, M. R.; Osberg, K. D.; MacFarlane, R. J.; Langille, M. R.; Mirkin, C. A. *Chem. Rev.* **2011**, *111*, 3736−3827.
14. Hao, F.; Sonnefraud, Y.; Van Dorpe, P.; Maier, S. A.; Halas, N. J.; Nordlander, P. *Nano Lett*. **2008**, *8*, 3983−3988.
15. Langille, M. R.; Personick, M. L.; Zhang, J.; Mirkin, C. A. *J. Am. Chem. Soc.* **2012**, *134*, 14542−14554.
16. Personick, M. L.; Mirkin, C. A. *J. Am. Chem. Soc*. **2013**, *135*, 18238−18247.
17. Wang, Y.; Xu, J.; Wang, Y.; Chen, H. *Chem. Soc. Rev.* **2013**, *42*, 2930−2962.
18. Wang, X.; Tang, Z. *Small* **2016**, *13*, 1601115
19. Tullius, R.; Karimullah, A. S.; Rodier, M.; Fitzpatrick, B.; Gadegaard, N.; Barron, L. D.; Rotello, V. M.; Cooke, G.; Lapthorn, A.; Kadodwala, M. *J. Am. Chem. Soc.* **2015**, *137*, 8380−8383.
20. Chen, G.; Roy, I.; Yang, C.; Prasad, P. N. *Chem. Rev.* **2016**, *116*, 2826−2885.
21. Heath, J. R. *Proc. Natl. Acad. Sci. U. S. A.* **2015**, *112*, 14436−14443.
22. Klinkova, A.; Choueiri, R. M.; Kumacheva, E. *Chem. Soc. Rev.* **2014**, *43*, 3976−3991.
23. Su, K. H.; Wei, Q. H.; Zhang, X.; Mock, J. J.; Smith, D. R.; Schultz, S. *Nano Lett.* **2003**, *3*, 1087−1090.
24. Jain, P. K.; Huang, W.; El-Sayed, M. A. *Nano Let*t. **2007**, *7*, 2080−2088.
25. Lim, D.-K.; Jeon, K.-S.; Kim, H. M.; Nam, J.-M.; Suh, Y. D. *Nat. Mater.* **2010**, *9*, 60−67.
26. Haidar, I.; Aubard, J.; Levi, G.; Lau-Truong, S.; Mouton, L.; Neuville, D. R.; Felidj, N.; Boubekeur-Lecaque, L. *J. Phys. Chem. C* **2015**, *119*, 23149−23158.
27. Sönnichsen, C.; Reinhard, B. M.; Liphardt, J.; Alivisatos, P. *Nat. Biotechnol.* **2005**, *23*, 741−745.
28. Chen, G.; Wang, Y.; Tan, L. H.; Yang, M.; Tan, L. S.; Chen, Y.; Chen, H. *J. Am. Chem. Soc*. **2009**, *131*, 218−4219.
29. Li, J. F.; Huang, Y. F.; Ding, Y.; Yang, Z. L.; Li, S. B.; Zhou, X. S.; Fan, F. R.; Zhang, W.; Zhou, Z. Y.; Wu, D. Y.; en, B.; Wang, Z. L.; Tian, Z. Q. *Nature* **2010**, *464*, 392−395.
30. Mertens, J.; Eiden, A. L.; Sigle, D. O.; Huang, F.; Lombardo, A.; Sun, Z.; Sundaram, R. S.; Colli, A.; Tserkezis, C.; Aizpurua, J.; Milana, S.; Ferrari, A. C.; Baumberg, J. J. *Nano Lett.* **2013**, *13*, 5033−5038.
31. Prodan, E.; Nordlander, P. J. *Chem. Phys.* **2004**, *120*, 5444−5454.
32. Jain, P. K.; El-Sayed, M. A. *Chem. Phys. Lett.* **2010**, *487*, 153−164.

33. Fan, J. a; Wu, C.; Bao, K.; Bao, J.; Bardhan, R.; Halas, N. J.; Manoharan, V. N.; Nordlander, P.; Shvets, G.; Capasso, F. *Science* **2010**, *328*, 1135−1138.
34. Tomalia, D. A.; Khanna, S. N. *Chem. Rev.* **2016**, *116*, 2705−2774.
35. Grzelczak, M.; Vermant, J.; Furst, E. M.; Liz-Marzán, L. M. *ACS Nano* **2010**, *4*, 3591−3605.
36. Xu, X.; Rosi, N. L.; Wang, Y.; Huo, F.; Mirkin, C. A. *J. Am. Chem. Soc.* **2006**, *128*, 9286−9287.
37. Cutler, J. I.; Auyeung, E.; Mirkin, C. A. *J. Am. Chem. Soc.* **2012**, *134*, 1376−1391.
38. Kumar, A.; Hwang, J.-H.; Kumar, S.; Nam, J.-M. *Chem. Commun*. **2013**, *49*, 2597−2609.
39. Chao, J.; Lin, Y.; Liu, H.; Wang, L.; Fan, C. *Mater. Today* **2015**, *18*, 326−335.
40. Wang, Z.; Zhang, J.; Ekman, J. M.; Kenis, P. J. A.; Lu, Y. *Nano Lett*. **2010**, *10*, 1886−1891.
41. Song, T.; Tang, L.; Tan, L. H.; Wang, X.; Satyavolu, N. S. R.; Xing, H.; Wang, Z.; Li, J.; Liang, H.; Lu, Y. *Angew. Chem., Int. Ed.* **2015**, *54*, 8114−8118.
42. Tan, L. H.; Yue, Y.; Satyavolu, N. S. R.; Ali, A. S.; Wang, Z.; Wu, Y.; Lu, Y. *J. Am. Chem. Soc.* **2015**, *137*, 14456−14464.
43. Oh, J.-W.; Lim, D.-K.; Kim, G.-H.; Suh, Y. D.; Nam, J.-M. *J. Am. Chem. Soc.* **2014**, *136*, 14052−14059.
44. Lee, J.-H.; Kim, G.-H.; Nam, J.-M. *J. Am. Chem. Soc.* **2012**, *134*, 5456−5459.
45. Sun, W.; Boulais, E.; Hakobyan, Y.; Wang, W. L.; Guan, A.; Bathe, M.; Yin, P. *Science* **2014**, *346*, 1258361.
46. Jones, M. R.; Seeman, N. C.; Mirkin, C. A. *Science* **2015**, *347*, 6224.
47. Seeman, N. C. *Nature* **2003**, *421*, 427−431.
48. Rothemund, P. W. K. *Nature* **2006**, *440*, 297−302.
49. Zhang, Y.; Chao, J.; Liu, H.; Wang, F.; Su, S.; Liu, B.; Zhang, L.; Shi, J.; Wang, L.; Huang, W.; Wang, L.; Fan, C. *Angew. Chem., Int. Ed.* **2016**, *55*, 8036−8040.
50. Lan, X.; Lu, X.; Shen, C.; Ke, Y.; Ni, W.; Wang, Q. *J. Am. Chem. Soc*. **2015**, *137*, 457−462.
51. Urban, M. J.; Dutta, P. K.; Wang, P.; Duan, X.; Shen, X.; Ding, B.; Ke, Y.; Liu, N. *J. Am. Chem. Soc*. **2016**, *138*, 5495−5498.
52. Zhou, C.; Duan, X.; Liu, N. *Nat. Commun*. **2015**, *6*, 8102.
53. Urban, M. J.; Zhou, C.; Duan, X.; Liu, N. *Nano Lett.* **2015**, *15*, 8392−8396.
54. Sefah, K.; Shangguan, D.; Xiong, X.; O’Donoghue, M. B.; Tan, W. *Nat. Protoc.* **2010**, *5*, 1169−1185.
55. Tan, Y. N.; Lee, J. Y.; Wang, D. I. C. *J. Am. Chem. Soc*. **2010**, *132*, 5677−5686.
56. Slocik, J. M.; Moore, J. T.; Wright, D. W. *Nano Lett.* **2002**, *2*, 169−173.
57. Naik, R. R.; Jones, S. E.; Murray, C. J.; McAuliffe, J. C.; Vaia, R. A.; Stone, M. O. *Adv. Funct. Mater.* **2004**, *14*, 25−30.
58. Naik, R. R.; Stringer, S. J.; Agarwal, G.; Jones, S. E.; Stone, M. O. *Nat. Mater*. **2002**, *1*, 169−172.
59. Djalali, R.; Chen, Y. F.; Matsui, H. *J. Am. Chem. Soc*. **2003**, *125*, 5873−5879.
60. Chen, C. L.; Zhang, P.; Rosi, N. L. *J. Am. Chem. Soc*. **2008**, *130*, 13555−13557.
61. Slocik, J. M.; Govorov, A. O.; Naik, R. R. *Nano Lett*. **2011**, *11*, 701−705.
62. Briggs, B. D.; Knecht, M. R. J. Phys. *Chem. Lett*. **2012**, *3*, 405−418.
63. Zhou, W.; Gao, X.; Liu, D.; Chen, X. *Chem. Rev.* **2015**, *115*, 10575−10636.
64. Zhang, Y.; Guo, Y.; Xianyu, Y.; Chen, W.; Zhao, Y.; Jiang, X. *Adv. Mater.* **2013**, *25*, 3802−3819.
65. Anker, J. N.; Hall, W. P.; Lyandres, O.; Shah, N. C.; Zhao, J.; Van Duyne, R. P. *Nat. Mater.* **2008**, *7*, 442−453.
66. Wang, Y.; Yan, B.; Chen, L. *Chem. Rev.* **2013**, *113*, 1391−1428.
67. Tajon, C. A.; Seo, D.; Asmussen, J.; Shah, N.; Jun, Y. W.; Craik, C. S. *ACS Nano* **2014**, *8*, 9199−9208.
68. Wang, H.; Rong, G.; Yan, B.; Yang, L.; Reinhard, B. M. *Nano Lett.* **2011**, *11*, 498−504.

69. Wang, J.; Boriskina, S. V.; Wang, H.; Reinhard, B. M. *ACS Nano* **2011**, *5*, 6619−6628.
70. Austin, L. a; Kang, B.; Yen, C.; El-sayed, M. A. *J. Am. Chem. Soc.* **2011**, *133*, 17594−17597.
71. Wang, J.; Yu, X.; Boriskina, S. V.; Reinhard, B. M. *Nano Lett.* **2012**, *12*, 3231−3237.
72. Fraire, J. C.; Masseroni, L.; Jausoro, I.; Perassi, E. M.; Diaz Añel, A. M.; Coronado, E. A. *ACS Nano* **2014**, *8*, 8942−8958.
73. Wang, X.; Cui, Y.; Irudayaraj, J. *ACS Nano* **2015**, *9*, 11924−11932.
74. Lee, S. E.; Chen, Q.; Bhat, R.; Petkiewicz, S.; Smith, J. M.; Ferry, V. E.; Correia, A. L.; Alivisatos, A. P.; Bissell, M. J. *Nano Lett.* **2015**, *15*, 4564−4570.
75. Liu, M.; Li, Q.; Liang, L.; Li, J.; Wang, K.; Li, J.; Lv, M.; Chen, N.; Song, H.; Lee, J.; Shi, J.; Wang, L.; Lal, R.; Fan, C. *Nature Commun.* **2017**, 8, 15646.

1.2. Supported Lipid Bilayer as a Dynamic Platform

Plasma membranes define the boundary of the cell from its extracellular environment. The cells constantly communicate with the environment through cell membrane where diverse membrane proteins functions. Lipids, the main components of plasma membrane, consist of hydrophilic heads and hydrophobic tail that self-assembles in water to form lipid bilayer vesicles or micelles to reduce the exposure of unfavorable hydrophobic tail to hydrophilic medium. The lipid bilayers have diverse state according to their composition and temperature. They show two-dimensional fluidity in liquid state above critical temperature, and they stay in gel phase below the critical temperature. The vesicle provides confined space from its outside, and the development of the lipid is critical event for the development of life. I envision the first form of so-called cell is self-replicating molecules (such as RNAs) in the vesicles, which encapsulate all the important key molecules and nutrients and provide safe place for replication.

Supported lipid bilayers (SLBs), self-assembled lipid bilayers on hydrophilic solid support, offer reconstituted model systems for cell membrane with controllable composition, high stability and lateral fluidity to mimic cell-cell junction and interactions. The SLBs also provides dynamic two-dimensional liquid-form surface for tethered particles, enabling dynamic interactions across 2D way. Observation of single plasmonic nanoparticles in reconstituted biological systems allows for obtaining the snapshots of dynamic processes between molecules/nanoparticles with unprecedented spatiotemporal resolution and single-molecule/single-particle-level data acquisition.

In this chapter, I introduce nanoparticle-tethered supported lipid bilayer platforms that allow the dynamic interaction for nanoparticles on a two-dimensional fluidic surface. The dark-field-based long-term, stable real-time observation of freely diffusing plasmonic nanoparticles on a lipid bilayer enables one to extract a broad range of information about interparticle and molecular interactions throughout the entire reaction period. I highlight important developments to provide ideas on how molecular interactions can be interpreted by monitoring dynamic behaviors and optical signals of laterally mobile nanoparticles.

Chapter 1.2 was published in parts as:

Kevin L. Hartman, Sungi Kim, Keunsuk Kim, Jwa-Min Nam, "Supported lipid bilayers as dynamic platforms for tethered particles" *Nanoscale* 2015, *7*, 66-76

and,

Young-Kwang Lee[+], Sungi Kim[+], Jwa-Min Nam, "Dark-Field-Based Observation of Single-Nanoparticle Dynamics on a Supported Lipid Bilayer for in situ Analysis of Interacting Molecules and Nanoparticles." *ChemPhysChem* 2015, *16*, 77-84.

[+] represents equal contribution

1.2.1. Introduction

Single-molecule fluorescence methods have addressed numerous biological questions by elucidating the heterogeneity and disorder in elementary molecular processes, which were inaccessible via ensemble measurements (1-8). Long-term, reliable observation is of practical importance to extract circumstantial information on fluctuating, dynamic reactions that occur on multiple time scales (9). This is, however, frequently limited by the undesirable photophysics of fluorescent molecules, i.e. blinking and bleaching (7, 10, 11). Metal nanoparticles have emerged as potential alternatives to organic fluorophores because they exhibit a higher optical cross-section and photostability, which benefit from localized surface plasmon resonance (LSPR) (12, 13). There have been extensive efforts in functionalizing the nanoparticles with biological molecules and utilizing them as optical probes in practical applications (14-16).

Single plasmonic metal nanoparticle experiments have frequently been accomplished, typically with dark-field-based imaging methods on reconstituted synthetic platforms to mimic and simplify complicated biological structures on a controllable and observable platform (17, 18). This enables us to observe molecular motions as well as enzymatic reactions at a single-molecule level. One would like to reliably monitor a large number of individual particles simultaneously for a long period to acquire sufficient data. For this, nanoparticles are, in most cases, immobilized on transparent glass surfaces to suppress three dimensional Brownian motion in solution and to continuously monitor them for an extended period of time. However, these immobilized nanoparticle-based strategies significantly restrict the applicability because these immobilized nanoparticles cannot offer dynamic information on the interactions between nanoparticles. It is furthermore difficult to monitor various dynamic molecular processes on immobilized nanoparticles. The most commonly used methods involve recording the spectral responses of immobile single plasmonic nanoparticles that display specific receptors to capture target molecules (19-21). When the target binds, the change in the local refractive index near the surface of the nanoparticle induces a LSPR frequency shift (22). These experiments, however, reconstruct only limited situations such as simple binding events with restricted particle mobility, and thus data reproducibility becomes a challenge. Molecular interaction-modulated nanostructures offer better signal to noise ratio and sensitivity but suffer from low synthetic yield for the targeted nanostructures (17, 23, 24). Recently developed liquid cell transmission electron microscopy (TEM) allows for the direct observation of single nanocrystal growth and interparticle coalescence events (25, 26). Although liquid cell TEM is a powerful tool for studying the growth of nanocrystals, it has intrinsic limitations such as the inevitable exposure to an electron flux that affects and damages biomolecules and nanoparticles, difficulty in real-time imaging of a large number of particles simultaneously, and limited accessibility. The bottom line is that none of these methods are able to completely visualize the interactions between nanoparticles (or molecules on nanoparticles) for a large number of particles: i) where nanoparticles/molecules come from, ii) how they behave before reactions, iii) when they associate and dissociate, iv) how assembled structures fluctuate during reactions, and v) if a single particle/molecule performs multiple successive reactions. In order to study such dynamic behaviors, freely diffusible plasmonic nanoprobes can be utilized rather than immobile ones to allow nanoparticles/molecules to undergo diverse reactions. The underlying details can be interpreted when the multiple nanoparticle movements and interactions are tracked for a sufficiently long period of time with single nanoparticle sensitivity. Introduction of diffusing particles also enables us to extend the scope of experimental design and data. For example, single particle tracking can determine physical changes and local heterogeneity of diffusion media induced by molecular reactions (27, 28). It is, therefore, highly desirable to develop a method that allows for in situ observation of the dynamic behavior of freely diffusing nanoparticles.

This chapter aims to introduce attempts to use nanoparticle-tethered lipid bilayers as an analytical platform to study a broad range of molecular interactions. The representative examples that are based on imaging and tracking of individual mobile nanoparticles on lipid bilayer surfaces will be presented in order to highlight how molecular reactions impact the dynamic behaviors of nanoparticles with dark-field microscopy system. This will provide insight into designing and analyzing more elaborate systems that require quantitative analysis of a whole range of physical characteristics of the nanoparticles in action.

1.2.2. Basic Setups and Strategies

Metal nanoparticles are effectively visualized via various microscopic techniques that mostly take advantage of a high scattering/absorption cross-section emerging from surface plasmon resonance (29). The spectral responses of individual plasmonic nanoparticles can be tuned in a broad spectral range as a function of particle composition, size, and shape (29-31). In addition, the nanoparticles can be optically coupled to each other and show sensitive spectral changes in an interparticle distance-dependent manner as observed in Förster resonance energy transfer of organic fluorophores, but driven by different mechanisms (32-34).

Dark-field microscopy is a simple and powerful technique that excludes the unscattered from the image and visualizes plasmonic nanoparticles with a high-contrast background. The position of metal nanoparticles can be determined with nanometer spatial precision and microsecond temporal resolution (18, 35). Individual nanoparticle images also possess unique and useful information such as scattering spectra and optical polarization as only the resonantly scattered light is collected through an objective lens. This indicates that dark-field microscopy affords a suit of optical readouts to determine various physical and chemical states of individual and interacting nanoparticles in situ. Dark-field microscopy has the advantage over other microscopic methods in the collection of spectral information of scattering signals, which permits precise monitoring of plasmonic coupling (17, 42). Plasmonic coupling enables the spectral shift and intensity change to be correlated to the distance between nanoparticles with nanometer precision (17, 42). Dark-field microscopy can monitor successive assembly and disassembly of nanoparticles, and furthermore visualize color-coding of multiple plasmonic nanoparticles (17, 45-47).

One of the major issues for single nanoparticle analysis is a lack of methods to simultaneously track many diffusing particles that are floating around in solution and continuously enter and exit the focal plane of the optical microscope. The uncontrolled movements of particles in the z-axis make it challenging to implement reliable long-term observations of moving particles (Figure 1a). Self-assembled lipid bilayers on hydrophilic solid supports, which are called supported lipid bilayers (SLBs), offer new platforms to address this issue. SLBs enable one to synthesize fluidic surfaces on solid substrates and incorporate a variety of species in a laterally mobile fashion. Once the nanoparticles are tethered to the SLBs, they are confined in the two-dimensional (2D) focal plane of the optical microscope while freely diffusing on substrate surfaces due to the fluidic nature of lipid bilayers (Figure 1b). The lateral fluidity of SLB was confirmed by fluorescence recovery after photobleaching (FRAP) (Figure 1e). The movements and interactions of the nanoparticles can be effectively imaged and tracked with single nanoparticle resolution for a long period due to much better photostability (Figure 1d).

Different molecular interactions give rise to a variety of physical consequences of the SLB-tethered nanoparticles (Figure 1b, c). The mobility and diffusion mode of the nanoparticles are affected either when anchor molecules directly interact with other molecules or when molecular interactions modulate physical and chemical properties of the surrounding membrane. Further, plasmonic coupling due to interactions between molecules on different nanoparticles can be detected by dark-field microscope imaging. These effects can be understood by quantitatively analyzing the changes in dynamic behaviors and optical properties of the nanoparticles.

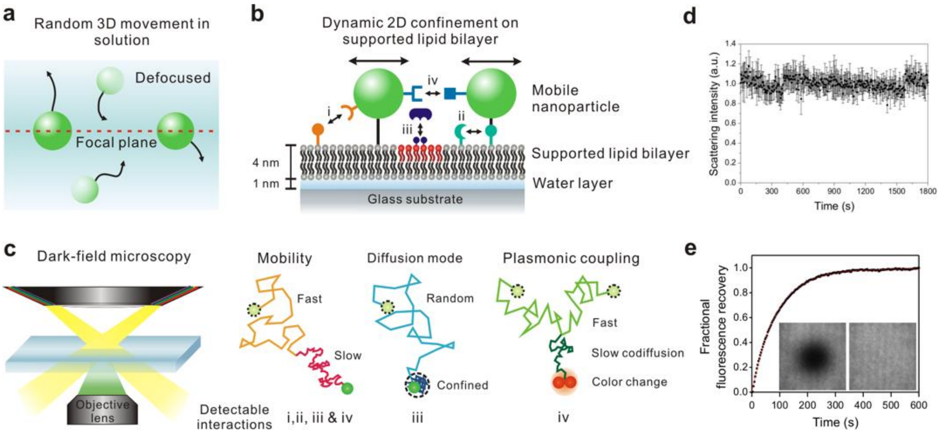

Figure 1. a) Movements of nanoparticles dispersed in solution. Nanoparticles show random three-dimensional motion and stay in the focal plane of an optical microscope only for a short time. b) A plasmonic nanoparticle-tethered supported lipid bilayer platform. Real-time imaging of laterally mobile plasmonic nanoparticles enables observation of i) receptor-ligand interactions, ii) interactions between membrane components, iii) soluble ligand binding and membrane clustering, and iv) universal pair interactions. c) A dark-field microscopy setup (left) and impacts of molecular interactions on dynamic behaviors and optical properties of plasmonic nanoparticles under dark-field microscopy imaging (right). d) The scattering intensity of the SLB-tethered PNP probes under the continuous dark-field illumination. The optical signal was recorded and calculated every 6 s from 7 individual immobile plasmonic nanoprobes. e) Fluorescence recover after photobleaching from a supported bilayer containing 1 mol % NBD-PC lipids. The plot was fitted to the equation $F(t) = A(1 - e^{-t\tau})$. (Inset images) Lipid bilayer images after initial photobleaching (left) and 6 min of recovery (right). d) and e) are reprinted with permission from Ref. (47). Copyright 2014 American Chemical Society.

1.2.3 Nanoparticle-Tethering Techniques

In the most basic sense, nanoparticle tethering to a bilayer involves a connection between a nanoparticle and the surface of the bilayer. Given the well-known methods for surface functionalization and reliable scattering properties, gold is a common core material for nanoparticle tethering. Part of its popularity also stems from the use of staining transmission electron microscopy (TEM) images with antibody-adsorbed gold colloids, a technique first conceived in 1971 (48, 49). Following this idea, the first nanoparticle bilayer tethering paper by G. M. Lee et al. involved adsorbing an antibody against fluorescein onto the surface of a 30 nm gold nanoparticle, and allowing it to attach to a bilayer containing 1.7 mol% fluorescein-labeled lipids while maintaining the mobility (50).

Proteins besides antibodies also adsorb well onto the negatively charged surface of citrate-capped gold nanoparticles, and have been used in creating linkages to the bilayer surface. For example, the tetrameric protein streptavidin can be adsorbed onto gold nanoparticles and linked to a bilayer containing a low percentage (≤1 mol%) of biotinylated lipids (51). The binding interaction between biotin and streptavidin (or its variants avidin and NeutrAvidin) creates the strongest non- covalent bond known and has been used successfully to create fluid displays of a stably-linked protein on bilayers (52-54). Hsieh et al. and Spillane et al. also used streptavidin-adsorbed gold nanoparticles, but instead of linking to a biotinylated bilayer, reacted the particles with a limited concentration of biotinylated cholera toxin subunit B (CTB) in solution (55, 56). The particles were next added to a bilayer containing ganglioside lipid (GM1), which is the natural ligand of CTB, and thus the tether was formed by the receptor–ligand interaction (Figure 1a). The native binding to GM1 in a bilayer was used by Kukura et al. to tether a virus-like particle (VLP) (57). The biotinylated Simian virus 40 was functionalized with a single streptavidin- modified QD and was attached to a fluid GM1 bilayer. The simultaneous visualization of both the fluorescence signal from the QD and the scattering signal from the VLP revealed its dynamic position and orientation (Figure 1b). Instead of using a separate linking molecule between a bilayer and a particle, Sagle et al. took a minimalist approach in adsorbing gold nanoparticles directly onto the bilayer (58). Given the strong negative charge of the citrate-capped gold nanoparticle, it could be connected electrostatically to a bilayer containing a positively charged lipid and retain the fluidity. In control experiments the researchers used the peak shift of the gold nanoparticles' localized surface plasmon resonance to confirm the specificity of the electrostatic tether.

The gold surface is especially known for its reactivity with thiol functional groups, and this chemistry has been used by Yang et al. and Ota et al. to link gold nanoparticles to bilayers containing thiolated lipids (59, 60). This occurs by simply incubating the gold nanoparticles on the SLB. To mediate the reactivity, both research groups first adsorbed bovine serum albumin onto the nanoparticles to block multivalent thiol–gold linkages. Instead of blocking the surface, Y. K. Lee et al. densely covered gold nanoparticles with thiolated DNA oligomers, some of which were capped with biotin to enable and control binding to a biotin–

streptavidin bilayer (Figure 1c) (61). Besides gold, the thiol group is reactive to other species available for tethering methods. For example, Murcia et al. functionalized CdSe/ZnS core–shell quantum dots with hydrophilic groups and male- imide, the latter of which reacts with thiolated lipids to form a covalent bond (62).

Creating tethered nanoparticle bilayers is also possible with commercially available nanoparticles, such as latex, polystyrene, quantum dots, or silica particles with functionalized surfaces. Hormel et al. used commercial NeutrAvidin-coated, fluorescent latex particles to link them to a biotin-displaying bilayer (63). They also added similar particles, but with a biotin coating, to form doublets with the tethered NeutrAvidin-coated particles (Figure 1d). Mascalchi et al. also used streptavidin or NeutrAvidin-coated particles, in this case with latex, quantum dots, or gold cores, but instead of linking them readily to biotin lipids, they used a biotinylated antibody against fluorescein (Figure 1e) (64). This enabled a tether to a fluorescein-containing bilayer, similar to the original tethering technique pioneered by G. M. Lee et al (50).

Lipid vesicles on the nanoscale can also be surface-functionalized, tethered to the bilayer, and tracked by fluorophores on the vesicle surface or enclosed within. The first published attempt of this used biotinylated lipids and avidin–streptavidin conjugation for long term, stable observation of single bio-molecule fluorescence, but did not allow lateral mobility (65). Mobile tethering of lipids came in 2003 when Yoshina-Ishii and Boxer reported using DNA hybridization for the linking mechanism (66). They achieved this with a disulfide exchange reaction of thiolated 24-mer oligonucleotides to dithiol lipids on the surface of the SLB and on 50 nm lipid vesicles. Upon hybridization of complementary strands, the tethered vesicles were laterally mobile and collided with each other. A sub- sequent paper by Yoshina-Ishii et al. substituted the disulfide exchange reaction, which could potentially react and denature proteins, with a gentler technique: oligonucleotides were conjugated to lipid headgroups, and these modified lipids were able to spontaneously insert into preformed SLBs and lipid vesicles.10 DNA hybridization following the modified lipid insertion also created a mobile display of tethered lipid vesicles (Figure 1f). Benkoski and Höök took a similar approach but instead used cholesterol-tagged DNA (67). Following the spontaneous insertion of the cholesterol into preformed vesicles and SLBs, DNA hybridization also produced diffusing, tethered vesicles. For vesicles with a more robust DNA tether, van Lengerich et al. (2010) devised a DNA-templated click reaction to attach the vesicles' DNA covalently to the SLB (68). Compared to the previous tethering techniques which relied on DNA hybrid- ization alone, this orthogonal covalent linkage has the advantage of stability under different buffer conditions, as low salt concentrations destabilize DNA base pairing.

The above studies represent a range of bilayer tethering techniques for nanoparticles that can be easily adapted or combined into new strategies. But more important than the tether's composition or physical behavior is the number of tethers per particle. This number exists on a continuum where a nanoparticle with several attachment points to a bilayer will exhibit limited or no mobility, even on a fluid bilayer. At the other extreme, a nanoparticle with very few, or just one attachment, will diffuse freely on a fluid bilayer. Thus, a successful bilayer platform of tethered nanoparticles involves controlling this degree of attachment. Part of this requires an optimal concentration of attaching lipids, which are mixed into the bilayer constituent lipids at concentrations ranging from 0.1 to 4 mol% depending on the chemistry involved (58, 59). For some experiments, it is more important to regulate the surface chemistry to reduce the number of surface anchoring sites. This was key for the original tethering by G. M. Lee et al. where mobile attachment was not achieved until blocking most of the fluorescein antibodies on the nanoparticle with a secondary antibody (50). Also limiting multiple tether formation, Y. K. Lee et al. used 1 : 799 molar ratio of biotinylated (tethering) DNA to non-biotinylated (target capture) DNA on their nanoparticles to produce a highly mobile attachment with an assumed single anchor on a bilayer with 0.1 mol% biotin– streptavidin (61).

In some cases, a nanoparticle's lack of curvature will generate multiple binding sites: larger nanoparticles with less curvature have more exposed surface area for multiple anchors. Mascalchi et al. cited this tendency to explain the slow diffusion of their 40 nm gold nanoparticles.32 Considering this disadvantage, Lin et al. and Hsieh et al. instead used 20 nm gold nanoparticles to limit the number of tethers formed per particle (55, 51). However, there are bounds to reducing the size as smaller nanoparticles produce weaker scattering, with a signal contrast pattern that can be confused with lipid vesicles on the surface (55, 56). Despite the disadvantage of lower mobility from multiple surface anchors, Hormel et al. attached larger particles (200 nm diameter NeutrAvidin-coated latex) to a bilayer displaying a relatively high concentration (1 mol%) of biotin lipids (63). Their goal was to create lipid footprint areas underneath the particles to better respond to the rotational and translational effects of the bilayer viscosity, and this approach would otherwise be limited with singly-anchored nanoparticles. Recently, Johnson-Buck et al. tethered rectangular DNA origami tiles to a fluid bilayer using the technique of cholesterol-DNA hybridization similar to Benkoski and Höök (67, 69). Each 60 × 90 × 2 nm tile was designed with 187 ssDNA of the identical nucleotide sequence exposed on one side. Of the hybridizing oligomers added, only 25% contained the bilayer- anchoring cholesterol. Though the exact number of bilayer connections per tile was not calculated and probably less than maximal due to charge repulsion, each particle was likely anchored by multiple strands. However, the modest 0.71 μm^2 s^{-1} diffusion of the tiles on the bilayer suggests that the spacing of the tethers, or perhaps the complete lack of particle curvature, may nullify the conditions leading to immobile tethering.

1.2.4. Real-Time Imaging and Tracking of Single Nanoparticles on SLB

Single molecule/particle imaging and tracking are powerful methods for investigating cell membranes. Direct visualization of single molecule trajectories reveals submicron-scale local heterogeneity of fluid plasma membranes and dynamic molecular interactions, which are unobservable with other ensemble measurements such as FRAP (38-41, 70, 71). The individual molecules undergo specific or transitional diffusion modes that are susceptible to interactions with local environments or other interacting molecules (72). The extraction of underlying physical parameters enables interpretation of dynamic behaviors of cell membrane components. Single-particle tracking becomes a more reliable technique to probe molecular interactions when implemented on a model membrane such as SLBs, which provide a more homogeneous and sensitive diffusion media compared to native cell membranes (73, 74).

The first observation of gold nanoparticle movement on a SLB was reported by Jacobson group (Figure 2) (75). The diffusion of lipid molecules was directly monitored with 30-nm gold nanoparticles that were tethered to fluorescein-conjugated lipids through antigen-antibody interaction. Under the video-enhanced contrast-combined bright-field microscopy, the attached gold nanoparticles exhibited Brownian motion, providing direct evidence for random diffusion of lipids in a SLB. They also observed lower diffusion coefficient values for multivalent nanoparticles with respect to the paucivalent nanoparticles, which bind only one or a few lipids. This reduced diffusion suggests that multivalent binding of the nanoparticle created a partially permeable membrane patch up to 30-40 nm in diameter. DIC microscopy has an advantage over dark-field microscopy in the low background signals from cellular components. Extensive works of single particle tracking on live cell membranes using this method were done by Kusumi and Jacobson (38-41, 70). They showed the dynamic and heterogeneous diffusion behaviors of receptor molecules in cell membranes compartmentalized at scales of a few hundred nanometers. Our lab developed a single particle tracking-based detection method for membrane receptor-ligand interactions on a model membrane using dark-field microscopy (Figure 3) (27). Unlike the bright background scattering from live cells under dark-field illumination, the geometrically flat SLB gives rise to minimum background noise, and thus clear dark-field imaging of tethered nanoparticles can be achieved. GM1 ganglioside was incorporated in SLBs and used as a membrane-receptor for capturing cholera toxin B subunit (CTB). Multivalent binding of CTBs to the GM1 receptors induced clustering of GM1 and created gel-phase lipid domains. These lipid domains could serve as obstacles that hinder the free movement of neighboring lipids and thus affect overall lipid fluidity in the SLB. The gold nanoparticles, tethered to thiolated lipids, were tracked in real time using dark-field microscopy to monitor the fluidity change of the SLB, and it was also proven that paucivalent nanoprobes are useful in improving probe mobility and detection sensitivity. This method quantitatively detected as low as 10 pM concentration in solution with four orders of magnitude dynamic range without direct labeling of the target protein.

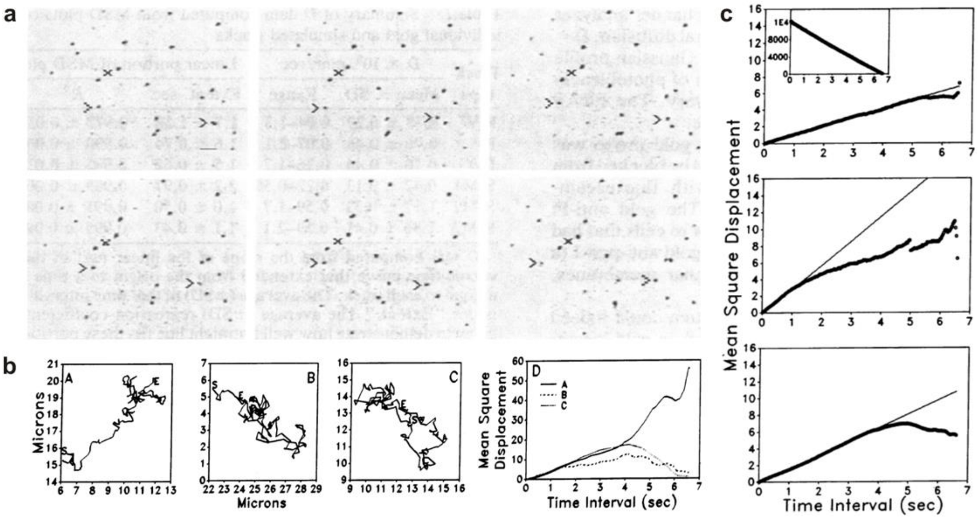

Figure 2. a) Video images of multivalent colloidal gold anti-fluorescein moving on a supported planar membrane containing fluorescein-conjugated phosphatidylethanolamine. Single gold particles are small black spots. Larger spots are aggregates. The images are 165 ms apart. The displacement of the gold particles can best be seen by comparing the position of moving particles (arrowheads) with immobile particles (x). (scale bar =1 μm.) b) (A-C) Trajectories of random motion of gold anti-Fl attached to a planar membrane. (D) The MSD (μm^2) plots for each of the tracks shown. Diffusion coefficients for each of the gold particles was 1.1 x 10^{-8} cm^2/sec, 1.0 x 10.8 cm^2/sec, and 1.3 x 10^{-8} cm^2/sec. c) Averaged MSD (μm^2) plots for 74 multivalent gold particles (top), 19 paucivalent gold particles (middle), and 10 simulated tracks (bottom). The MSD for each time interval was averaged for all tracks with D > 4 x 10^{-10} cm^2/sec. (Top inset) Number of displacements that were squared and averaged to give the MSD for each respective time interval in A. The solid lines are regression lines computed over the linear region of the curve: 0-3 sec (top), 0-1 sec (middle), and 0-4 sec (bottom) (47).

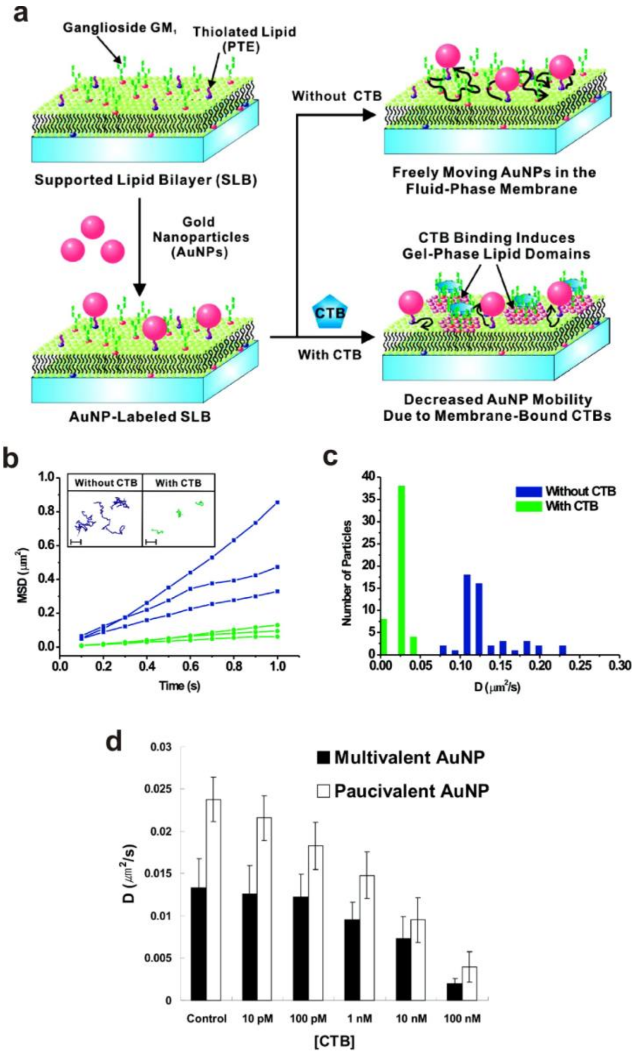

Figure 3. a) Single nanoparticle tracking-based detection on supported lipid bilayer platform. The movements of AuNPs are changed by molecular binding events on the supported lipid bilayer. b) The trajectories of lipid-tethered AuNPs (inset, the scale bars are 5 μm) and mean square displacement plots as a function of time. c) Histogram plot of diffusion coefficients for 50 tethered AuNPs. The average diffusion coefficients are 0.13 μm²/s without CTB and 0.02 μm²/s with CTB respectively. d) Single nanoparticle tracking-based CTB detection results for various concentrations of CTB using multivalent and paucivalent AuNP labels. The average diffusion coefficients of tethered AuNPs on SLB are plotted as a function of CTB concentration from 10 pM to 100 nM. Reprinted with permission from Ref. (27). Copyright 2009 American Chemical Society.

Sagle et al. implemented single-particle tracking on a SLB containing GM1 and measured the percolation threshold of a phase-separated model membrane system (Figure 4) (28). Negatively charged citrate-capped gold nanoparticles were electrostatically bound to positively charged lipids and exhibited random diffusion on the GM1-free SLB. They observed a linearly increasing tendency in the number of confined particles with GM1 concentration. This observation indicates the concentration- dependent formation of the heterogeneous GM1 clusters acting as solid barriers to free movement of lipids. The percolation threshold, in which all nanoparticles are confined within the discontinuous minor fluid phase surrounded by major GM1 clusters, was determined to be 22%. The confining diameter was also found to be ~50 nm.

1.2.5. Observation of Interactions between Single Nanoparticles

The interaction between molecules on different nanoparticle surfaces can be observed when those nanoparticles are on a SLB. In a single-particle tracking system, the interactive nanoparticles exhibit a series of changes in their movements due to their mutual recognition and subsequent co-localization and co-diffusion. The optical overlap does not always indicate that the particles are interacting with each other because particles that reside within the optical resolution can still be separated by a distance of up to several hundred nanometers. Therefore, the particle interactions should be confirmed with other supplementary observations such as particle dwelling time within a specific location. Direct monitoring of co-diffusion and changes in diffusion coefficient have been employed in single-molecule tracking techniques to probe interactions between membrane-tethered species (76). This could be extended to the detection of the particle interactions, but the effects of dimer and higher-order oligomer formation on the nanoparticle diffusion on SLBs, especially for a large number of particles, are still challenging and need to be studied further. Plasmonic coupling is a reliable indicator for differentiating the interactions between metal nanoparticles as it typically occurs only when the distance between the particles are below a few tens of nanometers (30, 32, 77). The plasmonic responses are highly sensitive within the length scale of biological interactions and reactions, and can be triggered by single molecule binding events that induce the formation or fluctuation of coupled metal nanostructures (78).

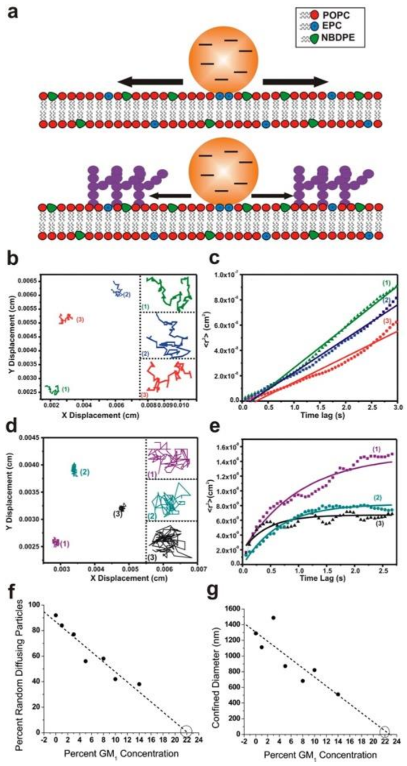

Figure 4. a) Schematic illustration of nanoparticle movement on a bilayer with no GM1 lipids (top) or with a bilayer containing >5 % GM1 lipids (bottom). The nanoparticles, electrostatically bound to bilayers with >5 % GM1, display confined motions that are restricted between GM1 clusters. b) The trajectories of three particles on a bilayer without GM1. c) Plot of root-mean-squared displacement as a function of time lag for the three particles shown in (b). The linear trend of root-mean-squared displacement plots of all three particles indicates Brownian motion. d) The trajectories of three particles on a bilayer with 10 % GM1. e) Plot of root-mean-squared displacement as a function of time lag for the three particles shown in (d). The plotted lines were fitted to the equations describing confined particle motions. f) Plot of percent confined particles as a function of GM1 concentration, showing a linear trend. It is expected that, at the percolation threshold, 100 % of the particles would show the confined behavior, and thus the percolation threshold is defined as the GM1 concentration at 0 % randomly diffusing particles. Linear extrapolation (dashed line) reveals a percolation threshold value of 22% GM1. g) Plot of confined diameter for the particles exhibiting a confined behavior as a function of GM1 concentration, showing a linear trend. Linear extrapolation (dashed line) reveals a confined diameter of 50 nm at the percolation threshold. Reprinted with permission from Ref. (28). Copyright 2012 American Chemical Society.

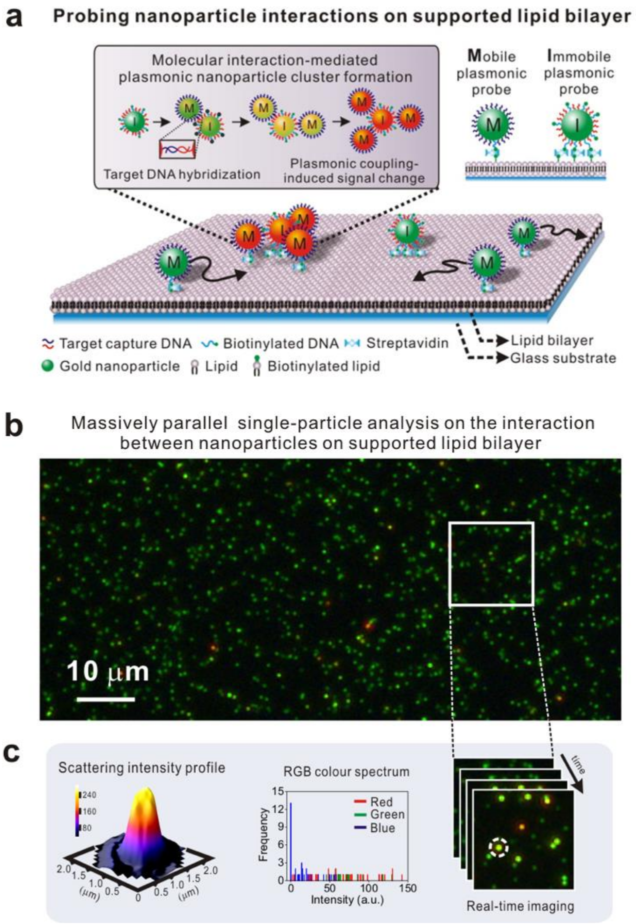

Figure 5. In situ parallel dark-field imaging and single-particle-level optical analysis of a large number of dynamically tethered nanoparticles on a supported lipid bilayer. a) Schematic illustration of the dynamic two-dimensional confinement of plasmonic nanoparticles on lipid bilayer surface. Two different types of probes (mobile and immobile plasmonic probes) are tethered to a supported lipid bilayer. Target DNA hybridization induces two-dimensional cluster formation and plasmonic coupling. b) Multiparallel in situ observation and quantitative analysis of supported lipid bilayer-tethered plasmonic nanoprobes via dark-field microscopy with single-nanoparticle resolution. c) The scattering intensity and RGB color spectrum are obtained from the single plasmonic cluster, marked with a white dashed line. Reprinted with permission from Ref. (47). Copyright 2014 American Chemical Society.

In 2014, our lab exploited plasmonic coupling to selectively measure DNA-induced interactions between metal nanoparticles on SLBs in situ (Figure 5a) (47). Plasmonic coupling of freely diffusing metal nanoparticles was specifically observed for short-range interactions, and nonspecific distant optical overlaps were clearly discriminated from the specific interaction-based change in plasmonic coupling (Figure 6a). It should be pointed out that a large number of nanoparticles can be reliably and stably tethered to a SLB using biotin-streptavidin interactions. This gives highly reliable single-particle-level quantitative data as nearly all of the particles on a SLB pattern can be tracked in real time (Figure 5b). This tethering strategy also allows for controlling particle mobility, and this ability renders two different probes for modification on the SLB (the mobile probes with low biotin valency that freely diffuse and interact, and the immobile probes with high biotin valency that serve as stable observation centers for particle cluster growth). In the presence of the target DNA sequences, the nanoparticles functionalized with complementary DNA sequences form two-dimensional multiparticle clusters on the fluidic lipid bilayer surface (Figure 6b). Hundreds of particles on the SLB can be simultaneously tracked, and their dynamic processes such as in situ nanoparticle cluster growth were imaged and analyzed. The assembly process was reversible in response to DNA hybridization/dehybridization reactions, and successfully resolved for observation of single-nanoparticle addition/elimination events in the dark-field microscope (Figure 6d). As the cluster evolved, the nanoparticles showed stepwise changes of both the scattering intensity and plasmon resonance wavelength in every monomeric particle addition step. It was also tested that this two-dimensional probe system allows for driving faster binding kinetics than with three-dimensionally-moving particles (Figure 6e). The plasmonic scattering signals of individual growing clusters were quantified with brightness and RGB color spectrum analysis in the dark-field microscope images. The intensity and color calibration curves were derived as a function of the degree of clustering, and used for highly sensitive detection of target DNA hybridization reactions. Using this platform, we also showed that single-base-mismatched DNA can be easily differentiated from a perfect-match DNA sequence at high fM levels. We believe that this nanoparticle-tethered dark-field SLB platform is able to provide ways of studying a large number of particles simultaneously, understanding their in situ interactions from the diversity of available molecular reaction geometries, rates, and fluctuations.

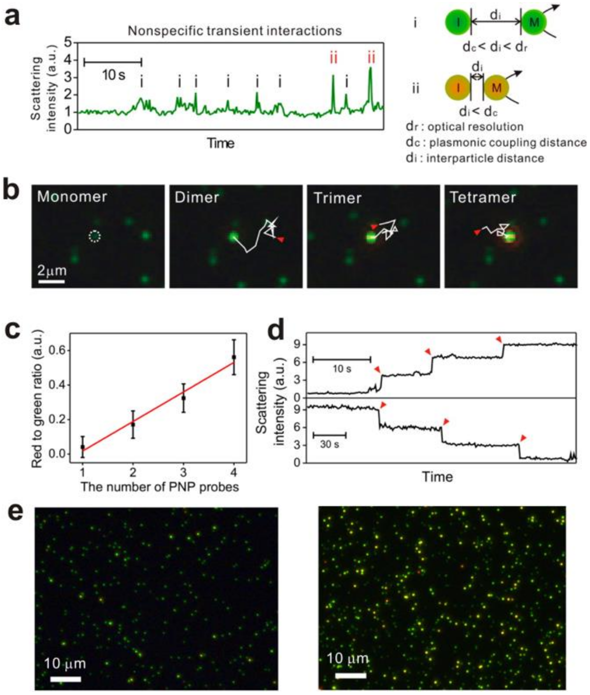

Figure 6. a) The time trace and schematic depiction of transient change in the scattering intensity for an immobile plasmonic probe site without target DNA sequence. b) The dark-field microscopic images of target DNA hybridization-induced plasmonic nanoparticle clusters. The 15-step trajectories of mobile probes from the starting position (red arrows) before binding are highlighted with white solid lines. The time interval for each trajectory step is 0.188 s. c) The red-to-green ratio plot for dark-field microscopic images of probe clusters as a function of the number of probes per cluster. (R^2 = 0.970, N = 30 clusters) d) Representative time traces of the scattering intensity for assembly (top) and disassembly (bottom) processes of nanoparticle clusters. e) The dark-field microscope images of the plasmonic nanoparticle probe-modified SLB after reaction with 300 pM target DNA sequence for 1 h. The immobile probes were tethered to the SLB surface and mobile probes were dispersed in solution (left). Both immobile and mobile probes were tethered to a SLB (right). The cluster formation kinetics were much faster when both immobile and mobile probes were tethered to the SLB. Reprinted with permission from Ref. (47). Copyright 2014 American Chemical Society.

1.2.6. References

1. Y. Harada, O. Ohara, A. Takatsuki, H. Itoh, N. Shimamoto, K. Kinosita, *Nature* **2001**, *409*, 113-115.
2. A. Yildiz, J. N. Forkey, S. A. McKinney, T. Ha, Y. E. Goldman, P. R. Selvin, *Science* **2003**, *300*, 2061-2065.
3. X. Zhuang, L. E. Bartley, H. P. Babcock, R. Russell, T. Ha, D. Herschlag, S. Chu, *Science* **2000**, *288*, 2048-2051.
4. H. P. Lu, L. Xun, X. S. Xie, *Science* **1998**, *282*, 1877-1882.
5. Z. Xie, N. Srividya, T. R. Sosnick, T. Pan, N. F. Scherer, *Proc. Natl. Acad. Sci. U.S.A.* **2004**, *101*, 534-539.
6. A. D. Douglass, R. D. Vale, *Cell* **2005**, *121*, 937-950.
7. L. A. Campos, J. Liu, X. Wang, R. Ramanathan, D. S. English, V. Munoz, *Nat. Methods* **2011**, *8*, 143-146.
8. A. Jain, R. Liu, B. Ramani, E. Arauz, Y. Ishitsuka, K. Ragunathan, J. Park, J. Chen, Y. K. Xiang, T. Ha *Nature* **2011**, *473*, 484-488.
9. B. P. English, W. Min, A. M. van Oijen, K. T. Lee, G. Luo, H. Sun, B. J. Cherayil, S. C. Kou, X. S. Xie, *Nat. Chem. Biol.* **2006**, *2*, 87-94.
10. C. Joo, H. Balci, Y. Ishitsuka, C. Buranachai, T. Ha, *Annu. Rev. Biochem.* **2008**, *77*, 51-76.
11. I. Rasnik, S. A. McKinney, T. Ha, *Nat. Meth*ods **2006**, *3*, 891-893.
12. J. Yguerabide, E. E. Yguerabide, *Anal. Biochem.* **1998**, *262*, 137-156.
13. L. Xiao, E. S. Yeung, *Annu. Rev. Anal. Chem.* **2014**, *7*, 7:8.1-8.23.
14. E. Boisselier, D. Astruc, *Chem. Soc. Rev.*. **2009**, *38*, 1759-1782.
15. R. Mout, D. F. Moyano, S. Rana, V. M. Rotello, *Chem. Soc. Rev*. **2012**, *41*, 2539-2544.
16. K. E. Sapsford, W. R. Algar, L. Berti, K. B. Gemmill, B. J. Casey, E. Oh, M. H. Stewart, I. L. Medintz, *Chem. Rev.* **2013**, *113*, 1904-2074.
17. B. M. Reinhard, S. Sheikholeslami, A. Mastroianni, A. P. Alivisatos, J. Liphardt, *Proc. Natl. Acad. Sci. U.S.A.* **2007**, *104*, 2667-2672.
18. X. Nan, P. A. Sims, X. S. Xie, *ChemPhysChem* **2008**, *9*, 707-712.
19. J. Zhao, A. Das, X. Zhang, G. C. Schatz, S. G. Sligar, R. P. Van Duyne, *J. Am. Chem. Soc.* **2006**, *128*, 11004-11005.
20. I. Ament, J. Prasad, A. Henkel, S. Schmachtel, C. Sönnichsen, *Nano Lett*. **2012**, *12*, 1092-1095.
21. G. Raschke, S. Kowarik, T. Franzl, C. Sönnichsen, T. A. Klar, J. Feldmann, A. Nichtl, K. Kürzinger, *Nano Lett.* **2003**, *3*, 935-938.
22. W. J. Galush, S. A. Shelby, M. J. Mulvihill, A. Tao, P. Yang, J. T. Groves, *Nano Lett*. **2009**, *9*, 2077-2082.
23. S. A. Claridge, H. W. Liang, S. R. Basu, J. M. J. Fréchet, A. P. Alivisatos, *Nano Lett.* **2008**, *8*, 1202-1206.
24. M. M. Maye, M. T. Kumara, D. Nykypanchuk, W. B. Sherman, O. Gang, *Nat. Nanotechnol*. **2010**, *5*, 116-120.
25. J. M. Yuk, J. Park, P. Ercius, K. Kim, D. J. Hellebusch, M. F. Crommie, J. Y. Lee, A. P. Alivisatos, *Science* **2012**, *336*, 61-64.
26. Y. Liu, X.-M. Lin, Y. Sun, T. Rajh, *J. Am. Chem. Soc.* **2013**, *135*, 3764-3767.
27. Y.-H. Yang, J.-M. Nam, *Anal. Chem.* **2009**, *81*, 2564-2568.
28. L. B. Sagle, L. K. Ruvuna, J. M. Bingham, C. Liu, P. S. Cremer, R. P. Van Duyne, *J. Am. Chem. Soc.* **2012**, *134*, 15832-15839.
29. P. K. Jain, K. S. Lee, I. H. El-Sayed, M. A. El-Sayed, *J. Phys. Chem. B* **2006**, *110*, 7238-7248.

30. K. L. Kelly, E. Coronado, L. L. Zhao, G. C. Schatz, *J. Phys. Chem. B*. **2002**, *107*, 668-677.
31. N. E. Motl, A. F. Smith, C. J. DeSantis, S. E. Skrabalak, *Chem. Soc. Rev*. **2014**, *43*, 3823-3834.
32. P. K. Jain, M. A. El-Sayed, *Chem. Phys. Lett.* **2010**, *487*, 153-164.
33. P. K. Jain, W. Huang, M. A. El-Sayed, *Nano Lett.* **2007**, *7*, 2080-2088.
34. N. J. Halas, S. Lal, W.-S. Chang, S. Link, P. Nordlander, *Chem. Rev.* **2011**, *111*, 3913-3961.
35. H. Ueno, S. Nishikawa, R. Iino, K. V. Tabata, S. Sakakihara, T. Yanagida, H. Noji, *Biophys. J.* **2010**, *98*, 2014-2023.
36. G. Wang, A. S. Stender, W. Sun, N. Fang, *Analyst* **2010**, *135*, 215-221.
37. Y. Gu, X. Di, W. Sun, G. Wang, N. Fang, *Anal. Chem.* **2012**, *84*, 4111-4117.
38. A. Kusumi, Y. Sako, M. Yamamoto, *Biophys. J.* **1993**, *65*, 2021-2040.
39. C. Dietrich, B. Yang, T. Fujiwara, A. Kusumi, K. Jacobson, *Biophys. J.* **2002**, *82*, 274-284.
40. K. Murase, T. Fujiwara, Y. Umemura, K. Suzuki, R. Iino, H. Yamashita, M. Saito, H. Murakoshi, K. Ritchie, A. Kusumi, *Biophys. J.* **2004**, *86*, 4075-4093.
41. K. Ritchie, X.-Y. Shan, J. Kondo, K. Iwasawa, T. Fujiwara, A. Kusumi, *Biophys. J.* **2005**, *88*, 2266-2277.
42. B. M. Reinhard, M. Siu, H. Agarwal, A. P. Alivisatos, J. Liphardt, *Nano Lett.* **2005**, *5*, 2246-2252.
43. W. Sun, G. Wang, N. Fang, E. S. Yeung, *Anal. Chem.* **2009**, *81*, 9203-9208.
44. A. E. Augspurger, A. S. Stender, R. Han, N. Fang, *Anal. Chem.* **2014**, *86*, 1196-1201.
45. S. Schultz, D. R. Smith, J. J. Mock, D. A. Schultz, *Proc. Natl. Acad. Sci. U.S.A.* **2000**, *97*, 996-1001.
46. A. Agrawal, R. Deo, G. D. Wang, M. D. Wang, S. Nie, *Proc. Natl. Acad. Sci. U.S.A.* 2008, 105, 3298-3303.
47. Y. K. Lee, S. Kim, J.-W. Oh, J.-M. Nam, *J. Am. Chem. Soc*. **2014**, *136*, 4081-4088.
48. W. P. Faulk and G. M. Taylor, Immunochemistry, 1971, 8, 1081–1083.
49. J. F. Hainfeld and R. D. Powell, J. Histochem. Cytochem., 2000, 48, 471–480.
50. G. M. Lee, A. Ishihara and K. A. Jacobson, Proc. Natl. Acad. Sci. U. S. A., 1991, 88, 6274–6278.
51. Y.-H. Lin, W.-L. Chang and C.-L. Hsieh, Opt. Express, 2014, 22, 9159–9170.
52. K. Salaita, P. M. Nair, R. S. Petit, R. M. Neve, D. Das, J. W. Gray and J. T. Groves, Science, 2010, 327, 1380–1385.
53. O. H. Laitinen, V. P. Hytönen, H. R. Nordlund and M. S. Kulomaa, Cell. Mol. Life Sci., 2006, 63, 2992–3017.
54. J.-M. Nam, P. M. Nair, R. M. Neve, J. W. Gray and J. T. Groves, ChemBioChem, 2006, 7, 436–440.
55. C.-L. Hsieh, S. Spindler, J. Ehrig and V. Sandoghdar, J. Phys. Chem. B, 2014, 118, 1545–1554.
56. K. M. Spillane, J. Ortega-Arroyo, G. de Wit, C. Eggeling, H. Ewers, M. I. Wallace and P. Kukura, Nano Lett., 2014, 14, 5390–5397.
57. P. Kukura, H. Ewers, C. Müller, A. Renn, A. Helenius and V. Sandoghdar, Nat. Methods, 2009, 6, 923–927.
58. L. B. Sagle, L. K. Ruvuna, J. M. Bingham, C. Liu, P. S. Cremer and R. P. Van Duyne, J. Am. Chem. Soc., 2012, 134, 15832–15839.
59. Y.-H. Yang and J.-M. Nam, Anal. Chem., 2009, 81, 2564–2568.
60. S. Ota, S. Wang, Y. Wang, X. Yin and X. Zhang, Nano Lett., 2013, 13, 2766–2770.
61. Y. K. Lee, S. Kim, J.-W. Oh and J.-M. Nam, J. Am. Chem. Soc., 2014, 136, 4081–4088.
62. M. J. Murcia, D. E. Minner, G.-M. Mustata, K. Ritchie and C. A. Naumann, J. Am. Chem. Soc., 2008, 130, 15054–15062.

63. T. T. Hormel, S. Q. Kurihara, M. K. Brennan, M. C. Wozniak and R. Parthasarathy, Phys. Rev. Lett., 2014, 112, 188101.
64. P. Mascalchi, E. Haanappel, K. Carayon, S. Mazères and L. Salomé, Soft Matter, 2012, 8, 4462–4470.
65. E. Boukobza, A. Sonnenfeld and G. Haran, J. Phys. Chem. B, 2001, 105, 12165–12170.
66. C. Yoshina-Ishii and S. G. Boxer, J. Am. Chem. Soc., 2003, 125, 3696–3697.
67. J. J. Benkoski and F. Höök, J. Phys. Chem. B, 2005, 109, 9773–9779.
68. B. van Lengerich, R. J. Rawle and S. G. Boxer, Langmuir, 2010, 26, 8666–8672.
69. A. Johnson-Buck, S. Jiang, H. Yan and N. G. Walter, ACS Nano, 2014, 8, 5641–5649.
70. A. Kusumi, C. Nakada, K. Ritchie, K. Murase, K. Suzuki, H. Murakoshi, R. S. Kasai, J. Kondo, T. Fujiwara, *Annu. Rev. Biophys. Biomol. Struct.* **2005**, *34*, 351-378.
71. M. J. Saxton, K. Jacobson, *Annu. Rev. Biophys. Biomol. Struct.* **1997**, *26*, 373-399.
72. F. Persson, M. Linden, C. Unoson, J. Elf, *Nat. Meth*ods **2013**, *10*, 265-269.
73. M. Ott, Y. Shai, G. Haran, *J. Phys. Chem. B*. **2013**, *117*, 13308-13321.
74. Y.-H. M. Chan, P. Lenz, S. G. Boxer, *Proc. Natl. Acad. Sci. U.S.A.* **2007**, *104*, 18913-18918.
75. G. M. Lee, A. Ishihara, K. A. Jacobson, *Proc. Natl. Acad. Sci. U.S.A.* **1991**, *88*, 6274-6278.
76. R. S. Kasai, A. Kusumi, *Curr. Opin. Cell Biol.* **2014**, *27*, 78-86.
77. S. A. Maier, M. L. Brongersma, P. G. Kik, H. A. Atwater, *Phys. Rev. B*. **2002**, *65*, 193408.
78. C. Sonnichsen, B. M. Reinhard, J. Liphardt, A. P. Alivisatos, *Nat. Biotechnol*. **2005**, *23*, 741-745.

Chapter 2

Multiplexed Biomolecular Detection Strategy

It is of great challenge to identify what is happening inside an intricate system such as a cellular environment or a reaction vessel. One way to understand the system is visualizing the reaction in real time with microscopic technique; for example, a biological process can be monitored using high-speed atomic force microscopy or nanoparticle growth can be observed using liquid transmission electron microscopy. These microscopic movies provide multidimensional spatial and temporal information that implies kinetic and thermodynamic information with high spatiotemporal resolution. The microscopic analysis can be employed in biosensors which transduce information about the target concentration to various types of signal (electrical, optical, etc.) that users can indirectly acquire and understand. Multiplexed detection, which detects multiple targets simultaneously, requires different signal outputs for each target in a single sample, unlike high-throughput detection that operates parallel detections in multiple separate samples. In this chapter, I developed a complex nanoparticle reaction mixture system on lipid bilayer and analyzed each reaction in a single-nanoparticle level using microscopy to detect nine biomolecules simultaneously. This multiplexed detection design principle using plasmonic nanoparticles is versatile and expanded to further develop nanoparticle network system.

This work was published in full as:

Sungi Kim, Jeong-Eun Park, Woosung Hwang, Jinyoung Seo, Young-Kwang Lee, Jae-Ho Hwang, and Jwa-Min Nam, “Optokinetically Encoded Nanoprobe-Based Multiplexing Strategy for MicroRNA Profiling” *J. Am. Chem. Soc.* 139, 3558-3566 (2017).

2.1. Introduction

Multiparallel reactions among a variety of reactants are common phenomena in chemical and biological systems (1−3). Simultaneous interpretation of multiple interactions from complex reaction mixtures offers important chemical or biological information including binding affinity and nature, reaction mechanisms, reaction and binding specificity, biodiagnostics, and rapid screening in biological sensing (4). It is, however, challenging to distinguish multiple interactions in a single reaction mixture due to the lack of tools for obtaining reliable information on complex binding events and their kinetic information with multiple (or multiplexed) readouts (5).

MicroRNAs (miRNAs) are small (∼22-nt), single stranded, noncoding RNAs. miRNAs act as post-transcriptional gene regulators and have emerged as potential diagnostic and prognostic biomarkers for human diseases including cancers and neurodegenerative diseases (6−8). The capability to identify and quantify multiple miRNA species is critical in translating miRNA sequences into useful information and is highly beneficial for improving the accuracy, precision, and specificity of diagnosis (9). Accurate quantification of miRNA is, however, difficult due to its intrinsically short length and instability (10). Although the quantitative reverse transcription polymerase chain reaction (qRT-PCR) offers high sensitivity and specificity, it requires poly-A tail or specially designed primer in cDNA formation and error-prone enzymatic amplification and is relatively lowthroughput (11). Microarrays are highthroughput, but they use fluorescence-based quantification that provides only relative expression values.11). Recently, researchers have developed nanostructure-based miRNA detection methods that use biobarcode amplification (12), nanopores (13), gold nanoparticles (14), scanometric arrays (15), silicon nanowires (16), graphene oxide (17), and quantum dots (18). However, previously reported nanostructure-based assays have limited multiplexing and quantification capabilities, and the assay time is typically well over 1 h with complicated multiple reaction steps and setups. Further, fluorescence-based methods including PCR and microarrays have limitations in photostability and multiplexing capability of fluorophore probes. Therefore, it remains challenging to develop a miRNA identification and quantification method that meets both speed and multiplexed detection requirements.

Here, we developed an optokinetically encoded plasmonic nanoprobe-based multiplexing strategy, and this strategy was used for miRNA profiling to identify and quantify 9 different miRNA species simultaneously on two-dimensional (2D) supported lipid bilayer (SLB) (Figure 1). The nanoprobes (NPs) here are coded optically (combinatorial plasmonic couplings) and kinetically (particle mobility) to generate highly multiplexed detection of targets (Figure 1). In DNA design, first, three different oligonucleotide sequences for detecting three different miRNA sequences and biotinylated DNA for tethering NPs to biotinylated SLB via streptavidins were modified to each NP. The number of modified biotinylated DNA strands per particle determines the mobility of probes for the kinetic coding (low biotin valency, mobile (M) probes; high biotin valency, immobile (I) probes) (19). For the optical coding, three different plasmonic nanostructures with distinctively different light scattering spectra [red (R), green (G), and blue (B) color-scattering nanostructures] were used (Figure 1a, b). Six types of optokinetically encoded NPs (MR-, MG-, MB-, IR-, IG-, and IB-NPs) were identified at single-particle level by real-time monitoring of their distinct scattering signals using dark-field microscopy (DFM). DNA sequences were modified to NP in a way that mobile NPs interact only with immobile NPs while M-NPs (or I-NPs) do not interact with other M-NPs (or I-NPs). It should be noted that target capturing induces assemblies of NPs and plasmonic coupling between NPs. The plasmonic coupling between different nanostructures generates unique scattering signal change, which is detectable and identifiable by DFM in a highly parallel manner (Figure 1b, d). Colorimetric signal change due to plasmonic coupling at the single nanoparticle-level was quantitatively analyzed with RGB color profiling method.

With this optokinetic (OK) coding strategy and highly photostable DFM-based single-particle analysis method on distinct plasmonic coupling, 9 different interactions between NPs induced by 9 different targets can be clearly distinguishable and detected on 2D SLB. Based on these designs and principles, we developed the OK-NP-tethered SLB (OK-NLB) assay. These nine NP assembly reactions were quantitatively analyzed as analogues of multicomponent association reactions (Figure 1c). Target miRNA sequences were selected based on the previous reports showing their abnormal expression patterns in multiple cancers (20−22). In principle, one can potentially differentiate and diagnose prostate, breast, and lung cancers by identifying these 9 miRNA targets in one sample. The OK-NLB assay was further validated with HeLa cell-extracted total RNA samples for 9 different RNA sequences, and the results were compared to the qRT-PCR.

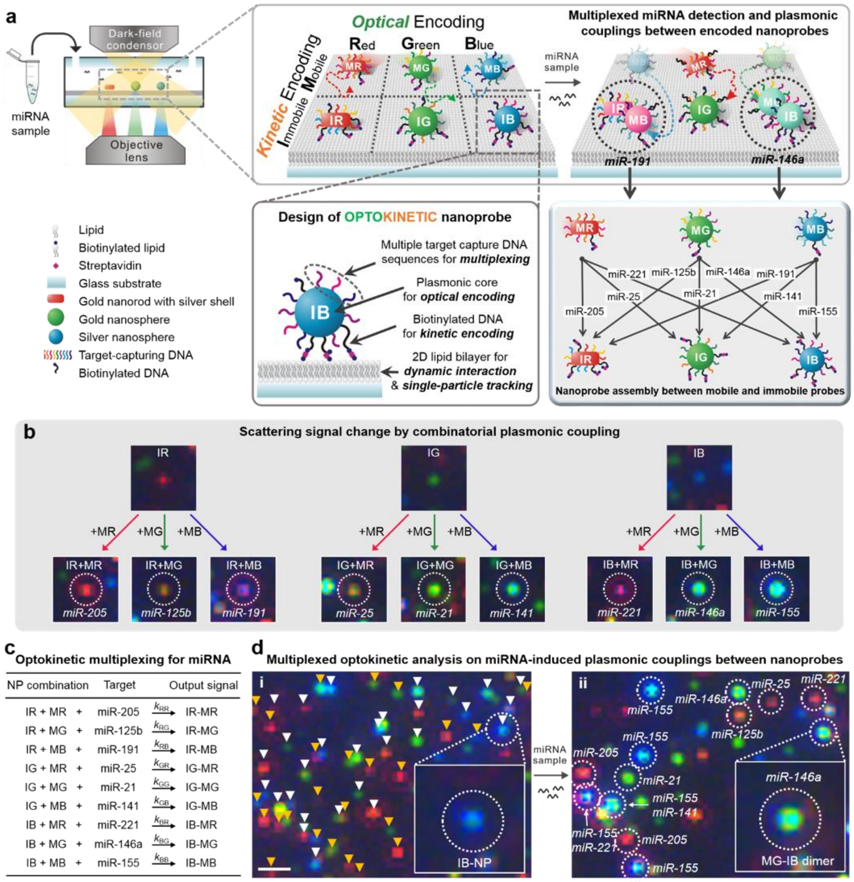

Figure 1. Optokinetically encoded nanoprobe (OK-NP)-tethered supported lipid bilayer (SLB) assay (OK-NLB assay). (a) The miRNA sample is directly injected into a reaction chamber, and NP interactions are monitored with dark-field microscopy (DFM). Six types of OK-NPs are prepared by kinetic [mobile (M) and immobile (I)] and optical [red (R), green (G), and blue (B)] coding methods. OK-NPs are composed of plasmonic nanoparticle core, multiple target capture DNAs, and biotinylated DNA. The NP assembly events between the M-NPs and the I-NPs are mediated by target miRNAs and identified with scattering color changes via plasmonic coupling. The nineplexing strategy using combinatorial assemblies between OK-NPs relies on each assembly mode, which was mediated by 9 different target miRNAs (bottom right). (b) Nine different scattering signal changes due to combinatorial plasmonic couplings induced by M-NPs binding to I-NPs. (c) Nine NP assembly reaction equations are described as multicomponent association reactions. (d) DFM images of DF scattering signals from individual OK-NPs on SLB. (d) (i) OK-NP identification by particle color and mobility. White and orange solid triangles indicate I-NPs and M-NPs, respectively. (ii) Multiplexed combinations of OK-NP assemblies reveal the target miRNA-induced particle assemblies in highly parallel manner (white dashed circles). The scale bar is 2 μm.

2.2. Experimental Section

Preparation of Small Unilamellar Vesicles (SUVs)

The SLBs were formed on the lower cover glass by SUV vesicle fusion. The lipid in chloroform solution was mixed to have 97.2 mol% dioleoylphosphatidylcholine (DOPC), 0.3 mol% biotinylated dioleoylphosphatidylethanolamine (DOPE), and 2.5 mol% 1k poly(ethylene glycol)−DOPE. The lipid mixture was evaporated with a rotary evaporator, and the lipid film was thoroughly dried under a stream of nitrogen. The dried mixture was resuspended in deionized (DI) water and followed by three repetitive freeze−thaw cycles. The total lipid concentration was 2 mg/mL. The solution was extruded 31 times through a polycarbonate membrane with 100 nm pores at 25 ℃. The SUV solution was kept at 4 ℃ until use.

Synthesis of Plasmonic Nanoparticles

Gold nanorods with an aspect ratio value of 4 were synthesized for red NPs by a seedmediated growth mechanism. The seed was prepared by mixing 5 mL of 0.5 mM $HAuCl_4 \cdot 3H_2O$ solution with 5 mL of 0.2 M cetyltrimethylammonium bromide (CTAB), followed by rapid injection of 600 μL of ice-cooled 0.01 M $NaBH_4$ solution. The seed solution was kept for 2 h after the reducing step. A 5 mL aliquot of 0.5 mM $HAuCl_4 \cdot 3H_2O$ solution was mixed with 5 mL of 0.2 M CTAB solution, and 250 μL of 4 mM $AgNO_3$ solution was added, followed by 70 μL of 78 mM ascorbic acid solution. Seed solution (12 μL) was added and gently mixed. The solution was incubated for 4 h. To enhance scattering intensity, we coated the gold nanorods with thin silver shells. Gold nanorods (1 mL, 100 nM) were mixed with cetyltrimethylammonium chloride (1 mL, 10 mM), $AgNO_3$ (1 mL, 0.2 mM), and ascorbic acid (1 mL, 50 mM). After 4 h incubation, the solution was washed three times by centrifugation, supernatant removal, and redispersion in DI water. Spherical gold nanoparticles (50 nm) were purchased from BBI Solutions (Cardiff, UK) for nanoparticles scattering green light. To synthesize nanoparticles scattering blue light, we formed 20 nm silver shells on 20 nm gold seed. Two hundred microliters of mixture was prepared to obtain 150 pM of 20 nm gold nanoparticle (BBI Solutions, Cardiff, UK), 0.2% polyvinylpyrrolidone (PVP), and 0.25 mM $AgNO_3$. Sodium ascorbate solution (100 μL, 50 mM) was rapidly injected into the mixture to form a silver shell, and the color turned yellow immediately. This solution was directly used for DNA modification for particle stability. The TEM images are obtained using JEM-2100 (JEOL) systems at the National Center for Inter-University Research Facilities (NCIRF), Korea.

Preparation of OK-NPs

Synthetic thiolated oligonucleotides (Bioneer, Daejeon, Korea) were reduced by incubation with 100 mM dithiothreitol (DTT) in 100 mM phosphate buffer (PB) solution for 1 h and separated with an NAP-5 column (GE Healthcare, Buckinghamshire, U.K.). For detailed sequences of thiolated oligonucleotides attached on each OK-NP, see Table S3. The mixture of thiolated strands at a concentration of 4 μM were incubated with 50 pM plasmonic nanoparticles for 2 h at room temperature. The ratio of biotinylated strands to target capturing strands are 1%, 0.1%, 0.5%, and 30% for MR-NP, MG-NP, MB-NP, and I-NP, respectively. The solution was adjusted to 10 mM PB and 0.1% (w/v) sodium dodecyl sulfate. Three aliquots of 1 M NaCl and 0.01% sodium dodecyl sulfate (SDS) solution were added with 1 h interval between each addition to achieve a final concentration of 0.3 M. The mixture was heated at 55 ℃ for 10 min after each salt addition. The mixture was incubated overnight at room temperature. The suspension was washed by centrifugation, the supernatant removal, and particle redispersion in 10 mM PB solution three times.

Reaction Chamber Preparation

SLBs were formed inside a glass flow chamber, consisting of a top and bottom glass and a thermoplastic spacer. The top slide glass was drilled to form inlet and outlet holes and passivated with 10 mg/mL bovine serum albumin solution to block SLB formation. The bottom cover glass was sonicated for 10 min in chloroform, acetone, and DI water. After sonication, the bottom glass was cleaned with 1 M NaOH for 1 h and thoroughly washed with DI water. The top and the bottom glasses were assembled with a sandwiched thermoplastic spacer by heating at 120 ℃ on a digital hot plate. The SUV solution was prepared to have 1 mg/mL of SUV, 75 mM of NaCl, and 10 mM of phosphate buffer. The solution was introduced into the flow chamber for 40 min to form SLBs. The volume of the flow chamber was 9 μL. Streptavidin (10 nM) in 150 mM NaCl phosphate buffered saline (PBS, 10 mM phosphate buffer, pH 7.5) was injected to the flow cell to bind to the biotinylated lipid for 1 h. The flow cell was washed with 150 mM NaCl PBS twice at each step. NPs (1−10 pM) were reacted for 10 min to have optimized density of ∼700 NPs/14400 μm^2 for each M-NP and ∼1200 NPs/ 14400 μm^2 for each I-NP. The buffer was exchanged to 225 mM NaCl PBS for assay conditions. Cell Culture. HeLa (human epithelial carcinoma line; ATCC, Num. CCL-2) cells were purchased from the Korean Cell Line Bank (Seoul, Korea). The cells were cultured in RPMI medium (Gibco, USA) containing 10% fetal bovine serum, 100 U/mL penicillin, and 100 μg/mL streptomycin (Gibco, USA). The cell line was incubated at 37 ℃ with 5% CO_2 in a humidified incubator.

Total RNA Extraction from HeLa Cells

We used the Qiagen miRNeasy miRNA extraction kit (Hilden, Germany), which isolates total RNA (>18 nucleotides) through phenol/guanidine-based lysis of samples and silica membrane-based purification. Eighty percent of confluent cells grown in a monolayer in 75 cm^2 flask were trypsinized and transferred to a clean 2 mL microcentrifuge tube. After centrifugation at 300 × g for 5 min, the cells were collected as a cell pellet, and the supernatant was completely aspirated. The cell pellet was mixed with 700 μL of QIAzol lysis reagent, homogenized by vortexing, incubated for 5 min at room temperature, and subsequently mixed with

140 μL of chloroform. The organic and aqueous phases were separated by centrifugation for 15 min at 12 000 × g at 4 ℃. The aqueous phase containing the RNA was carefully transferred to a new collection tube and mixed with 1.5 volumes of 100% ethanol. The mixture was loaded into an RNeasy Mini spin column and washed several times at 8100 × g. The RNeasy Mini column was transferred to a clean 1.5 mL collection tube, and RNA was eluted by addition of 50 μL of RNase-free water. The total RNA concentration was 120 ng/μL with $A_{260}/A_{280} = \sim 2$. The cell extract was kept frozen until use.

Real-Time Monitoring of Combinatorial Assembly between OK-NPs and OK-NLB Assays

The movement and combinatorial assembly between OK-NPs on SLBs were observed with DF microscope (Axiovert 200M, Carl Zeiss, Germany) with 40× objective lens (NA = 0.6) and AxiCam HR color camera. To characterize association of OK-NPs and to obtain a calibration curve, synthetic miRNAs were purchased from Bioneer (Daejeon, Korea) (Table S3). Known concentrations of miRNA targets in 225 mM NaCl PBS were injected into the reaction chamber. The negative control sample contains 300 pM of miR-100. The NP binding events were monitored with DFM. Snapshot images were taken at 10 min intervals for 1 h, and the assembly events in a $120 \times 120\ \mu m^2$ area were counted. It should be noted that the calibration curves for detection targets of interest need to be calculated only one time, and the preobtained calibration curves can be used for actual assays. For the

HeLa cell assay, cell extracts were diluted to a final concentration of 600 ng/μL in 225 mM NaCl PBS and injected into the reaction cell. Three replicate samples were analyzed. The images were analyzed using ImageJ software (https://imagej.nih.gov/ij/).

qRT-PCR Analysis

The qRT-PCR analysis of cell extracts was performed using Geno-Total RNA kit (Genolution, Seoul, Korea). cDNA was synthesized from total RNA sample with the Mir-X kit (Clontech). A SYBR Green-based qRT-PCR reaction was conducted with the real-time PCR system (Bio-Rad CFX) using Geno-qPCR kit no. RD1101 (Genolution, Seoul, Korea). PCR was carried out with initial denaturation at 95 ℃ for 2 min, followed by 40 cycles of 95 ℃ for 5 s and 60 ℃ for 20 s. Relative expressions of each miRNA to U6 snRNA as an internal control were calculated by the $2^{-\Delta CT}$ method. The reactions were run in duplicate to obtain standard deviations.

2.3. Results and Discussion

In a typical experiment, we prepared DNA-modified nanoparticles and tethered these particles to SLBs. Three target capture DNA sequences that are half-complementary to target miRNA, were modified onto each OK-NPs (Figure 1 and Table S3). For distinct optical encoding, we prepared three types of plasmonic nanoparticles that scatter red, green, and blue light by varying size, shape, and composition to yield desirable optical properties. Gold nanorods with a silver shell (～46 nm in longer axis and ～13 nm in shorter axis with ～5 nm shell), gold nanospheres (～47 nm in diameter), and silver nanospheres on gold seeds (～19 nm core and ～37 in diameter) were synthesized and used as R-NPs, G-NPs, and B-NPs, respectively. The DFM images showed red, green, and blue scattering signals from the nanoparticles, and R-NPs, G-NPs, and B-NPs showed distinct localized surface plasmon resonance at different wavelengths in the extinction spectra (Figures 2a, b). Because of their distinct optical properties, we can individually identify R-, G-, and B-NPs from a mixture of densely tethered NPs on SLBs (Figure 2c). The NPs were kinetically encoded on the SLB by controlling the ratio of biotinylated (tethering group to streptavidin) DNA to target-capturing DNA on the nanoparticle surface. Biotinylated DNA can be bound to the biotinylated SLB via multivalent streptavidin linkers. The particles with a low valency were tethered with high mobility, whereas the particles with a high valency were immobilized by forming multiple linkages between the particles and the SLB (19).

M-NPs showed random 2D Brownian motion confirmed by linear mean square displacement plot (Figures 2d, e). Nearly 90% of M-NPs were mobile on the SLB (Figure S1a). The lipid-tethered NPs occasionally exhibited a confined behavior and hop diffusion when observed for a prolonged period (>10 min), mainly because of incomplete homogeneity in lipid substrates (23). Particle diffusion in fluids is explained by the Stokes−Einstein equation, which describes that hydrodynamic radius is inversely proportional to diffusion coefficients in 3D Brownian motion. Interestingly, the average diffusion coefficients of MR-, MG-, and MB-NPs were 0.362 ± 0.227, 0.383 ± 0.203, and 0.379 ± 0.202 $\mu m^2/s$, respectively. These results indicate that the diffusion of these mobile probes did not depend on the different hydrodynamic size of the NPs, which implies that the diffusion of the tethered NPs is mainly driven by the lateral mobility of lipids, and the kinetic encoding of NPs is decoupled with optical encoding. We also checked the photostability of OK-NPs on SLBs under continuous illumination of dark-field light source for 1 h (Figure 2f). Significantly, the RGB profiles of scattering intensities of red, green, and blue probes were well maintained without photoblinking or photobleaching for the whole observation period (60 min), indicative of high photostability of the light scattering OK-NPs on SLB.

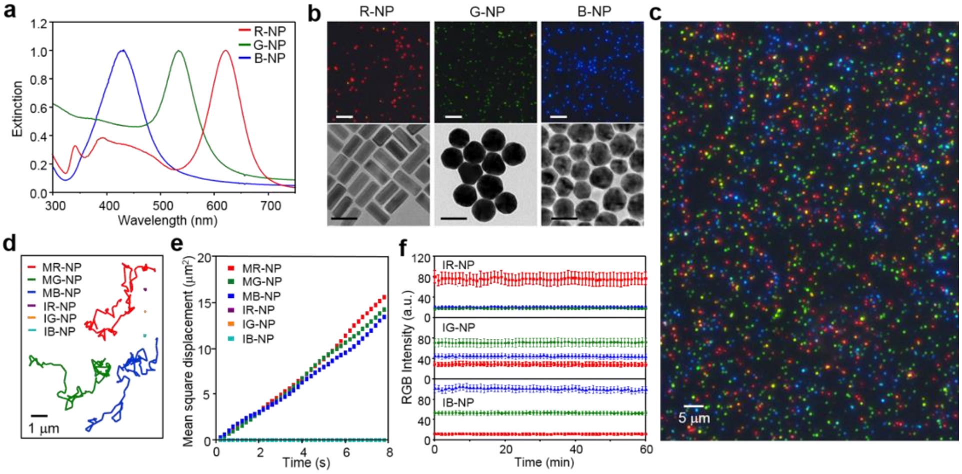

Figure 2. Photostable plasmonic NPs and DFM-based identification of the types of OK-NPs. (a) The extinction spectra of three optically encoded NPs. (b) DFM images (top) and transmission electron microscopy images (bottom) of R-NPs, G-NPs, and B-NPs (from left to right). The scale bars are 10 μm (DFM) and 50 nm (TEM). (c) A large area DFM image of the OK-NPs on SLB. (d) Representative diffusion trajectories and (e) mean square displacement plot of OK-NPs. The NPs with two kinetic states (M-NPs and I-NPs) show clear distinction in diffusion. (f) Averaged red (red square), green (green circle), and blue (blue triangle) scattering intensity of each I-NP under continuous dark-field illumination for 60 min. The images were taken every 1 min, and error bars are standard deviation from 20 NPs.

Next, we verified that the real-time monitoring of the six OK-NPs can differentiate 9 different types of plasmonic coupling signals based on different target miRNA induced binding events (Figure 3a). Without target addition, only transient scattering color changing events were observed due to temporary nonspecific overlaps between M-NPs and I-NPs. In the presence of the targets, the miRNAs were hybridized with half complementary DNA strands on both M- and I-NPs, confining M-NPs to I-NPs to induce plasmonic coupling between particles. We interpreted and classified the types of association events using light-scattering signal changes in DFM images and RGB intensity profiles of each particle. R-, G-, and B-NP monomers were represented as distinct red, green, and blue spots in the DF image with the strongest red, green, and blue channel intensities, respectively, in RGB profiles (Figure S1b).

Binding of MR-, MG-, and MB-NPs to an I-NP increased red, green, and blue color intensities, respectively. Accordingly, the red, green, and blue colors of R−R, G−G, and B−B homodimers are significantly brighter than R-, G-, and B-NP monomers. The R−G, G−B, and B−R heterodimers displayed orange, cyan, and magenta colors. The binding of a MR-NP to an I-NP only increased red color intensity with negligible changes in green and blue color intensities. Assembly with MG-NPs enhanced both red and green color intensities, whereas assembly with MB-NPs resulted in distinct change in blue color intensity. A red-shift of color profile in association among G- and B-NPs was observed as a result of a plasmonic coupling effect (24). The formations of MG− IG dimer and MB−IB dimer induced higher R to G and G to B ratios, respectively, compared to their monomer states. Theabove in situ monitoring and color profiling strategy also can identify trimer formation (the addition of a third NP to dimer). However, in the case of tetramer formation (addition of the fourth NP to trimer, which is rare), it was challenging to differentiate which M-NP was engaged with the trimer, due to the complex plasmonic coupling arising from different geometric configurations. Therefore, we controlled the density of I-NPs to be higher than that of M-NPs to reduce multimer formation and thereby simplify data analysis. Due to heterogeneity in the size and optical signals of NPs, particle tracking should be initiated prior to the target addition to fully differentiate each NP assembly event with high reliability. All 9 types of different interactions were successfully discriminated and counted in a parallel manner over a large area (Figure 3b).

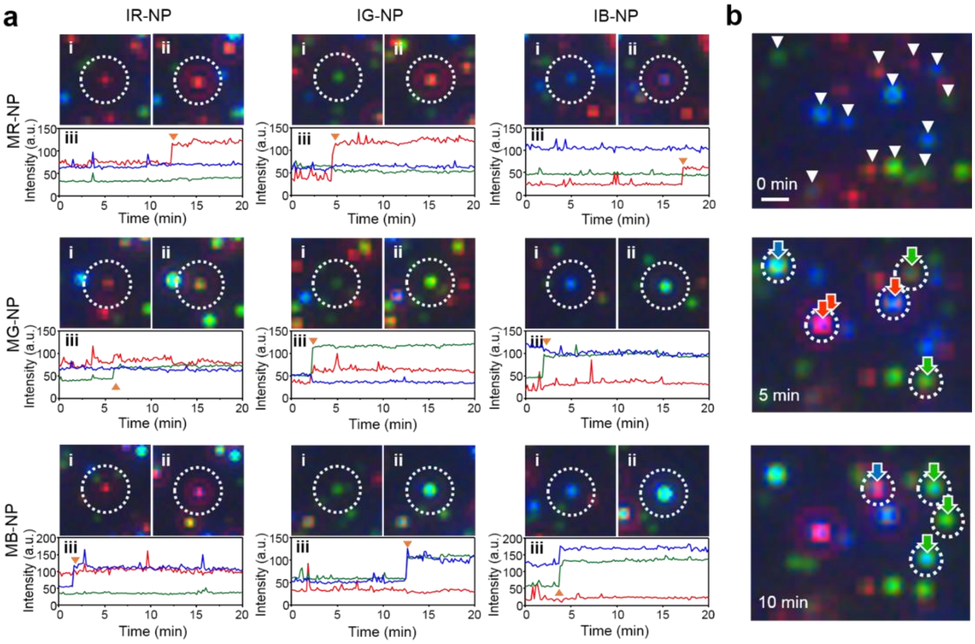

Figure 3. Multiplexable and parallel identification of the interaction between OK-NPs by combinatorial plasmonic coupling. (a) Real-time monitoring of combinatorial assemblies between OK-NPs. OK-NPs were monitored with 10 s interval after addition of 10 nM of 9 target miRNAs. DFM images of 9 combinations at (i) 0 min and (ii) 20 min (Videos S1−9). The bindings of M-NPs to I-NPs result in distinct color and signal intensity change. (iii) The RGB intensity profiles show characteristic patterns for the binding of MR-, MG-, and MB-NPs. The binding events are indicated with orange triangles. (b) Parallel observation of the individual binding events (white dashed circle) between I-NPs (white triangle) and MR- (red arrow), MG- (green arrow), and MB-NPs (blue arrow) (Video S10). The scale bar is 1 μm.

Before obtaining a calibration curve, we analyzed the NP reaction kinetics. The binding events can be regarded as multicomponent association reactions (Figure 1c and eq 1).

$$\text{I-NP} + \text{M-NP} + \text{miRNA} \rightarrow \text{I-M complex} \quad (1)$$

We first tested the effect of NP density on NP association reaction. Although we aimed to load a similar number of NPs on SLBs in different reaction chambers by controlling loading time and particle concentration, there were deviations in the NP density for each batch. The higher density of M-NPs and INPs resulted in an increased number of binding events for the same target concentration (Figure 4a and Table S1). When the number of binding events after 60 min incubation was proportional to $[\text{I-NP}]^{0.5}[\text{M-NP}]^{0.5}$, the lowest standard deviation and largest R^2 value were obtained (Figure 4b).

The logarithm of target concentration showed a linear behavior with the normalized binding events (Figure S2). By considering the NP density and target concentration factors, we can build the reaction kinetics equation for the OK-NP reaction.

$$(\text{Binding events}) = k_{\text{XY}} \cdot \frac{[IX-NP]^{0.5}[MY-NP]^{0.5}}{1000\ \ NPs/unit\ \ area} \cdot \log([\text{miRNA}]/\text{pM})$$

$$(\text{X, Y} = \text{R, G, B}) \quad (2)$$

where k_{XY} is reaction rate constant (1 h), which represents the binding efficiency, [IX-NP] and [MY-NP] is the 2D NP density. To remove the effect of different NP density per reaction chamber, we used the normalized the binding events by setting the internal reference as 1000 NPs/unit area with the density factor after measurement (eq 3 and Figure 4c).

$$\text{(Normalized binding events)} = \text{(Binding events)} \cdot \frac{1{,}000\ \text{NPs/unit area}}{[I-NP]^{0.5}[M-NP]^{0.5}} \quad (3)$$

We calculated the k values for nine different OK-NP reactions with the slope of a linear relation region of the calibration curve (Figure S2 and Table S2). Considering melting temperature of a target sequence, the association reaction between R-NP and B-NP shows the highest value. The rate constant is affected by the hybridization energy, which is determined by the target miRNA sequence, DNA modification density for OK-NPs, NP morphology, etc. The diversity in k value implies that the target sequence and the types of NPs affect the binding efficiency.

Under these conditions, we obtained the calibration curves of the normalized binding events with target concentrations ranging from 3 to 300 pM (Figure 4d). The binding events were counted on 120 × 120 μm^2 SLBs with consecutive images every 10 min. The logarithm of target concentration showed linear behavior with the normalized binding events (Figure S2). The limit of detection (LoD) ranged between 3 and 10 pM (30−100 amol) for 9 miRNA targets without optimizations. The kinetic responses of binding events were dependent on the combination of NPs. Furthermore, miRNA sequence has an influence on the kinetics of assembly and disassembly with complementary DNA sequences (25).

An assay time of 1 h was sufficient to discriminate different target concentrations. Longer assay time did not noticeably increase the sensitivity because the binding event curve reached a plateau after 1 h when a small amount of target was present. OK-NLB assay allows for differentiating small differences in miRNA expression, which is key to distinguishing dysregulated miRNA expression for cancer diagnosis (13).

To examine the multiplexing capability and the crossreactivity of the OK-NLB assay, we tested samples containing 100 pM targets with several different combinations of miRNA targets (Figures 5a, b). miRNA profiling results were analyzed through in situ monitoring of nine association reactions. Although each M-NP is designed to bind to three types of INPs simultaneously, the assay showed negligible cross-reactivity in all the cases and specifically detected the targets with high reliability and quantification capability. Even when all 9 targets existed in one sample, the assay was able to detect all the targets with similar quantification results (the far-right histogram of Figure 5b). We also confirmed the specificity of the assay. Single-base-mismatched targets at 300 and 10 pM were tested for three orthogonal targets (miR-21 for MG-IG, miR-155 for MB-IB, and miR-205 for MR-IR; Figure 5c and Table S3). The single-base-mismatched target showed signals from 10 pM single-base-mismatched targets were not differentiable from control signals. The single nucleotide polymorphism (SNP) in G−C pair for miR-205 showed greater discrimination than SNP in A−U pair for miR-21. The detected amount of 300 pM single-base mismatched input ranged between 10 and less than the LoD. The results prove the SNP selectivity and specificity of the OK-NLB assay.

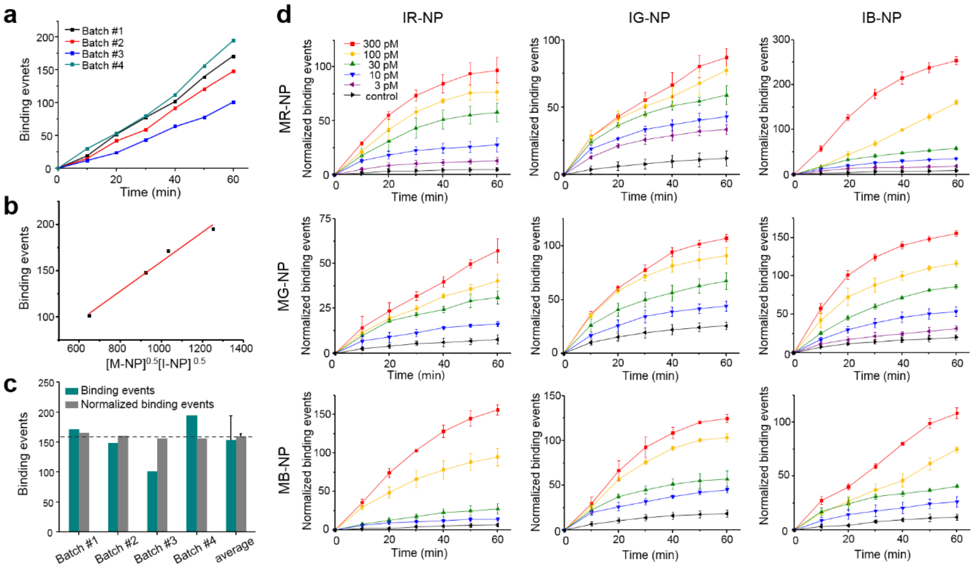

Figure 4. Kinetics and quantification of miRNA binding events. (a) Cumulative binding events for 60 min between MR-NPs and IB-NPs at 100-pM miRNA with different NP densities on SLB (Table S1). (b) The number of binding events at 60 min is proportional to $[M\text{-}NP]^{0.5}$ and $[I\text{-}NP]^{0.5}$. The orders were fitted to have the largest R^2 value (0.9868) and the smallest standard deviation of normalized binding events. (c) Binding events at 60 min from different batches were normalized by (Normalized binding events) = $\frac{(Binding\ \ events)}{[M-NP]^{0.5}[I-NP]^{0.5}}\cdot$1,000 NPs/unit area was set as an internal reference. The normalized binding events with varying NP densities show similar values with a small standard deviation compared to the standard deviation without normalization. (d) Normalized binding events of 9 miRNAs at different concentrations. The error bars represent the standard deviations from three independent experiments. Control experiments contained 300 pM of negative control miRNA (miR-100).

Finally, we performed miRNA profiling of total RNA samples extracted from HeLa cells (human cervical adenocarcinoma) with the OK-NLB assay (Figure 5d). We used 0.6 μg of total RNA for cancer cell assay. miR-21, an oncogene widely overexpressed in diverse cancers including cervical cancers (26), showed the highest expression level. The measured values of miR-141, miR-146a, miR-155, and miR-205 were below LoD, and this result is consistent with the previous report that showed those miRNAs have low or no expression in HeLa cells (27). We spiked miR-146a (30 pM final concentration) in a total RNA sample and quantified it using the OK-NLB assay. The detected amount of target was 25.7 ± 1.62 pM. The spiked sample showed 94% of the normalized binding events, compared to that of the same concentration of target sample in buffer condition. Six percent signal loss was largely due to cell debris in the lysate observed on the SLB (Figure S3). We further validated the result of the OK-NLB assay using qRT- PCR. The relative expression value of each miRNA to the internal reference U6 was plotted against the absolute concentration of miRNA obtained from OK-NLB assay (Figure 5e). The two assay results showed strong agreement with R^2 values of >0.999. Moreover, the expression pattern of 9 miRNA targets was well matched with the reported value obtained by microarray-based assay (28).

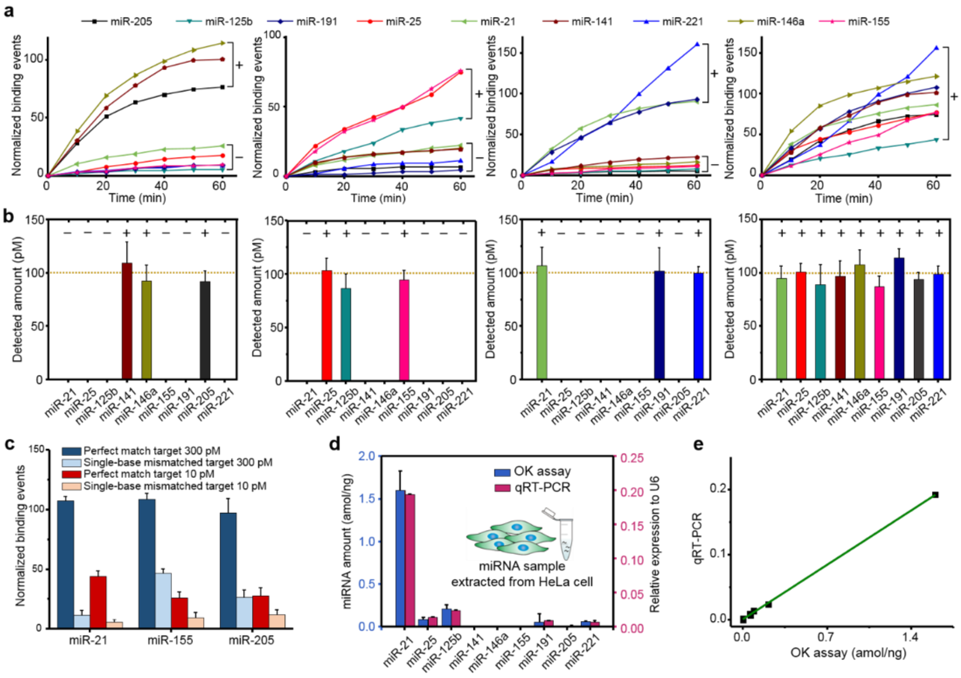

Figure 5. Multiplexed detection of miRNA sequences. (a) Representative data for in situ monitoring of binding events and (b) multiplexed profiling results from different combinations of 100-pM target miRNA sequences. Plus (minus) sign indicates presence (absence) of the target miRNA in samples. The detected amount was obtained from calibration curves (Figure S2). The dashed lines indicate the added amount of target miRNA. The results prove the multiplexing capability and negligible cross-reactivity within experimental errors of the assay. (c) Discrimination between target miRNA and single-base mismatched target at 300 pM and 10 pM. Single-base mismatched target show < 43% normalized binding events at 300 pM, and indistinguishable signals with control signals at 10 pM. (d) Multiplexed miRNA profiling of total RNA extract from HeLa cells and validation with qRT-PCR. qRT-PCR result shows relative expression value to U6 snRNA. (e) Correlation of OK-NLB assay with qRT-PCR based on the results of total RNA from HeLa cells. The 9 target miRNA results obtained with two methods show a strong agreement (R^2=0.9993). The standard deviations are obtained from three independent experiments.

2.4. Conclusion

In summary, we developed an optokinetically encoded light scattering NP-based assay on SLBs (OK-NLB assay), which allows real-time monitoring of individual NP assembly modes. The assay enables rapid, sensitive, quantitative, and multiplexed profiling of 9 different miRNAs in one sample without complicated setup, target modification, and enzymatic amplification. The probes on SLBs used herein were modified with three different target miRNA complements and mobility controlling biotinylated DNA for multiplexed optokinetic encoding and showed remarkable photostability with DFM that allows for in situ monitoring of the probes and reliable quantification of their binding events with miRNA. As a proof of concept, we showed the highly specific detection of various combinations of 9 different miRNA targets with 9 interacting pairs of probes between mobile R, G, or B probes and immobile R, G, or B probes on SLBs. In situ single-particle monitoring and normalized RGB analysis of 2D diffusion and target miRNA-facilitated binding of a large number of the photostable NPs with DFM in a highly parallel manner allows for reliably differentiating and quantifying 9 different miRNA targets in one sample. Moreover, single-base mismatched target miRNA sequences were clearly discernible from target miRNA sequences on the OK-NLB assay platform. Highly selective detection of different miRNA sequences used here implies the diagnosis of breast, prostate, lung, pancreas and stomach cancers from clinical samples could be potentially possible with further optimizations. (9) For rigorous validation, we profiled the expression levels of 9 miRNAs from cervical cancer cell extracts within 1 h and confirmed that the expression pattern is consistent with qRT-PCR result. The assay should be readily applicable to study other complex biological and chemical reactions because the surface of OK-NPs can be modified with diverse biochemical ligands (28−30). The multiplexed profiling strategy with OK-NPs on SLBs expands the number of multiplexable targets and opens new ways of developing highly multiplexed signals with photostable probes on a highly analyzable, quantifiable platform. The OK-NLB platform could be useful for rapid and multiplexed pathogen detection (31, 32), as well as cancer diagnosis.

2.5. Supporting Information

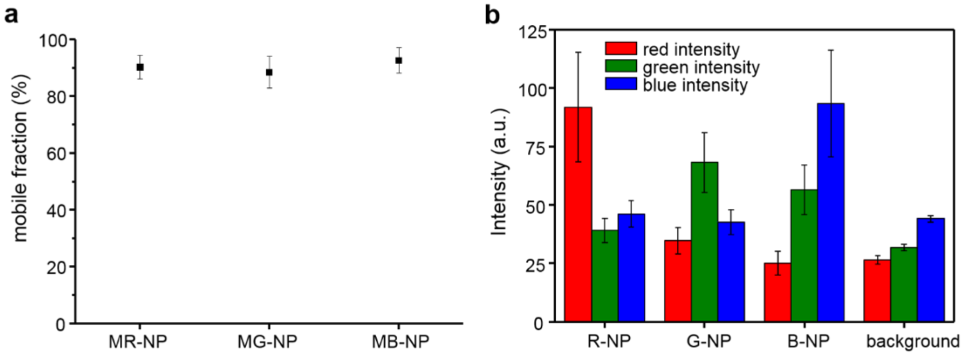

Figure S1. (a) Mobile fraction of MR-, MG-, and MB-NPs. Each standard deviation was obtained from three independent measurements (*N*=500). (b) Average RGB intensities of R-, G-, and B-NPs and background (*N*=100).

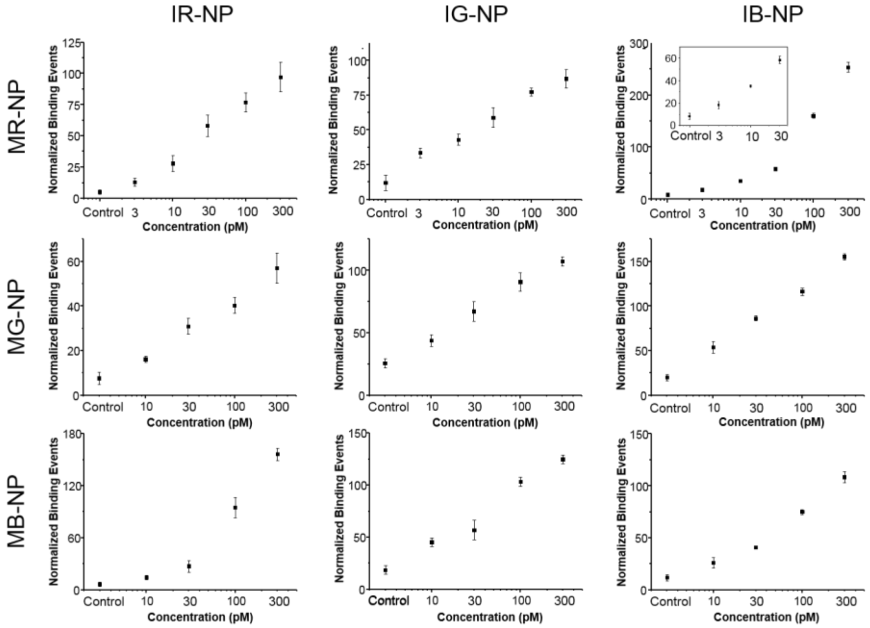

Figure S2. Calibration curves with varying target concentrations. The error bars represent the standard deviations from three independent experiments. Control experiments contained 300 pM of negative control miRNA (miR-100).

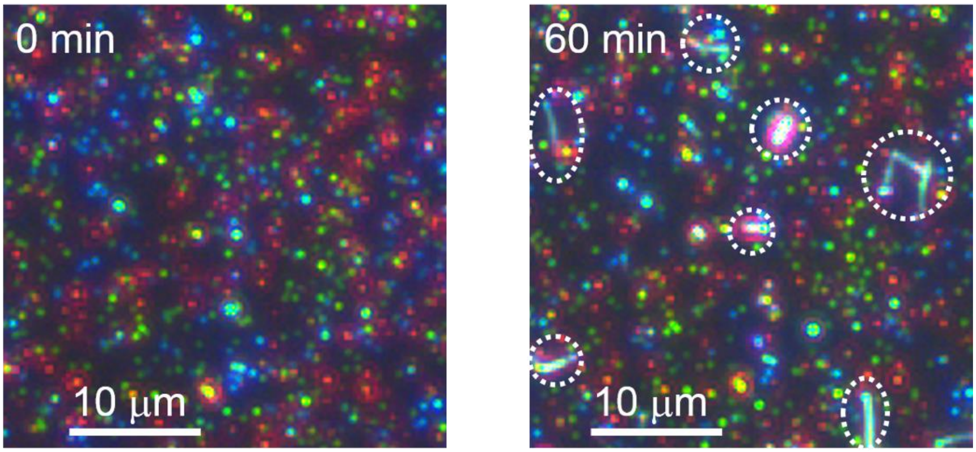

Figure S3. Cell debris from total RNA extract sample on NP-modified SLB (white dashed circles). Nonspecific binding of NPs to cell debris induces signal loss.

Table S1. Binding event of 100 pM of target miRNA after 60 min from four batches with different particle densities on SLB. The ratio of I-NPs to M-NPs ranged between 1.8 and 2.5 to minimize multimer (trimer or higher) formation. Unit area is 120 × 120 μm^2.

	Batch #1	Batch #2	Batch #3	Batch #4
# of I-NPs/unit area ([M-NP])	1629	1440	882	1872
# of M-NPs/unit area ([I-NP])	657	594	477	837
Binding events	171	148	101	195

Table S2. Reaction constants for each combinatorial assembly reaction.

	IR-NP	IG-NP	IB-NP
MR-NP	45.6	30.4	195.4
MG-NP	26.5	43.0	67.5
MB-NP	129.1	54.1	67.6

Table S3. Oligonucleotide and miRNA sequences.

Synthetic oligonucleotides and miRNAs	Sequences (5’ → 3’)
miR-21	UAGCUUAUCAGACUGAUGUUGA
miR-25	CAUUGCACUUGUCUCGGUCUGA
miR-125b	UCCCUGAGACCCUAACUUGUGA
miR-141	UAACACUGUCUGGUAAAGAUGG
miR-146a	UGAGAACUGAAUUCCAUGGGUU
miR-155	UUAAUGCUAAUCGUGAUAGGGGU
miR-191	CAACGGAAUCCCAAAAGCAGCUG
miR-205	UCCUUCAUUCCACCGGAGUCUG
miR-221	AGCUACAUUGUCUGCUGGGUUUC
miR-100	AACCCGUAGAUCCGAACUUGUG
Single base mismatched miR-21	UAGCAUAUCAGACUGAUGUUGA
Single base mismatched miR-155	UUAAUGCUGAUCGUGAUAGGGGU
Single base mismatched miR-205	UCCUUCAUUCCACCGGAAUCUG
biotinylated DNA for M-NP	HS-(CH$_2$)$_6$-PEG$_6$-CTTTGAGCACTGTTAGCGTGTGTGGAATTTTAAT-biotin
biotinylated DNA for I-NP	biotin-TAATTTTAAGGTGTGTGCGATTGTCACGAGTTTC-PEG$_6$-(CH$_2$)$_3$-SH
miR-205 capturing DNA for MR-NP	HS-(CH$_2$)$_6$-A$_{15}$-PEG$_6$-CAGACTCCGGT
miR-25 capturing DNA for MR-NP	HS-(CH$_2$)$_6$-A$_{15}$-PEG$_6$-TCAGACCGAGA
miR-221 capturing DNA for MR-NP	HS-(CH$_2$)$_6$-A$_{15}$-PEG$_6$-GAAACCCAGCA
miR-125b capturing DNA for MG-NP	HS-(CH$_2$)$_6$-A$_{15}$-PEG$_6$-TCACAAGTTAG
miR-21 capturing DNA for MG-NP	HS-(CH$_2$)$_6$-A$_{15}$-PEG$_6$-TCAACATCAGT
miR-146a capturing DNA for MG-NP	HS-(CH$_2$)$_6$-A$_{15}$-PEG$_6$-AACCCATGGAA
miR-191 capturing DNA for MB-NP	HS-(CH$_2$)$_6$-A$_{15}$-PEG$_6$-CAGCTGCTTTTG
miR-141 capturing DNA for MB-NP	HS-(CH$_2$)$_6$-A$_{15}$-PEG$_6$-CCATCTTTACC
miR-155 capturing DNA for MB-NP	HS-(CH$_2$)$_6$-A$_{15}$-PEG$_6$-ACCCCTATCACG
miR-205 capturing DNA for IR-NP	GGAATGAAGGA-PEG$_6$-A$_{15}$-(CH$_2$)$_3$-SH

miR-125b capturing DNA for IR-NP	GGTCTCAGGGA-PEG$_6$-A$_{15}$-(CH$_2$)$_3$-SH
miR-191 capturing DNA for IR-NP	GGATTCCGTTG-PEG$_6$-A$_{15}$-(CH$_2$)$_3$-SH
miR-25 capturing DNA for IG-NP	CAAGTGCAATG-PEG$_6$-A$_{15}$-(CH$_2$)$_3$-SH
miR-21 capturing DNA for IG-NP	CTGATAAGCTA-PEG$_6$-A$_{15}$-(CH$_2$)$_3$-SH
miR-141 capturing DNA for IG-NP	AGACAGTGTTA-PEG$_6$-A$_{15}$-(CH$_2$)$_3$-SH
miR-221 capturing DNA for IB-NP	GACAATGTAGCT-PEG$_6$-A$_{15}$-(CH$_2$)$_3$-SH
miR-146a capturing DNA for IB-NP	TTCAGTTCTCA-PEG$_6$-A$_{15}$-(CH$_2$)$_3$-SH
miR-155 capturing DNA for IB-NP	ATTAGCATTAA-PEG$_6$-A$_{15}$-(CH$_2$)$_3$-SH

2.6. References

1. Zhao, Y.; Cheng, Y.; Shang, L.; Wang, J.; Xie, Z.; Gu, Z. *small*, **2015**, *11*, 151-174
2. He, L.; Hannon, G. J. *Nat. Rev. Genet.* **2004**, *5*, 522–531.
3. Mitchell, P. S.; Parkin, R. K.; Kroh, E. M.; Fritz, B. R.; Wyman, S. K.; Pogosova-Agadjanyan, E. L.; Peterson, A.; Noteboom, J.; O'Briant, K. C.; Allen, A.; Lin, D. W.; Urban, N.; Drescher, C. W.; Knudsen, B. S.; Stirewalt, D. L.; Gentleman, R.; Vessella, R. L.; Nelson, P. S.; Martin, D. B.; Tewari, M. *Proc. Natl. Acad. Sci. U. S. A.* **2008**, *105*, 10513–10518.
4. Li, Y.; Kowdley, K. V. *Genomics. Proteomics Bioinformatics* **2012**, *10*, 246–253.
5. Wang, J.; Zhang, K. Y.; Liu, S. M.; Sen, S. *Molecules* **2014**, *19*, 1912–1938.
6. Carthew, R. W.; Sontheimer, E. J. *Cell* **2009**, *136*, 642–655.
7. Pritchard, C. C.; Cheng, H. H.; Tewari, M. *Nat. Rev. Genet.* **2012**, *13*, 358–369.
8. Lee, H.; Park, J.-E.; Nam, J.-M. *Nat. Commun.* **2014**, 5, 3367
9. Wang, Y.; Zheng, D.; Tan, Q.; Wang, M. X.; Gu, L.-Q. *Nat. Nanotechnol.* **2011**, 6, 668–674.
10. Degliangeli, F.; Kshirsagar, P.; Brunetti, V.; Pompa, P. P.; Fiammengo, R. *J. Am. Chem. Soc.* **2014**, 136, 2264-2267.
11. Alhasan, A. H.; Kim, D. Y.; Daniel, W. L.; Watson, E.; Meeks, J. J.; Thaxton, C. S.; Mirkin, C. A. *Anal. Chem.* **2012**, *84*, 4153-4160.
12. Lu, N.; Gao, A.; Dai, P.; Song, S.; Fan, C.; Wang, Y.; Li, T. *Small* **2014**, *10*, 2022–2028.
13. Dong, H.; Zhang, J.; Ju, H.; Lu, H.; Wang, S.; Jin, S.; Hao, K.; Du, H.; Zhang, X. *Anal. Chem.* **2012**, *84*, 4587–4593.
14. Zeng, Y.; Zhu, G.; Yang, X.; Cao, J.; Jing, Z.; Zhang, C. *Chem. Commun.* **2014**, *50*, 7160–7162.
15. Lee, Y. K.; Kim, S.; Oh, J. W.; Nam, J. M. *J. Am. Chem. Soc.* **2014**, *136*, 4081–4088.
16. Volinia, S.; Calin, G. a; Liu, C.-G.; Ambs, S.; Cimmino, A.; Petrocca, F.; Visone, R.; Iorio, M.; Roldo, C.; Ferracin, M.; Prueitt, R. L.; Yanaihara, N.; Lanza, G.; Scarpa, A.; Vecchione, A.; Negrini, M.; Harris, C. C.; Croce, C. M. *Proc. Natl. Acad. Sci. U. S. A.* **2006**, *103*, 2257–2261
17. Wang, W.-T.; Chen, Y.-Q. J. *Hematol. Oncol.* **2014**, *7*, 86
18. Kosaka, N.; Iguchi, H.; Ochiya, T. *Cancer Sci.* **2010**, *101*, 2087–2092
19. Hsieh, C. L.; Spindler, S.; Ehrig, J.; Sandoghdar, V. *J. Phys. Chem. B* **2014**, *118*, 1545–1554
20. Rong, G.; Wang, H.; Skewis, L. R.; Reinhard, B. M. *Nano Lett.* **2008**, *8*, 3386–3393/
21. Johnson-Buck, A.; Su, X.; Giraldez, M. D.; Zhao, M.; Tewari, M.; Walter, N. G. *Nat. Biotechnol.* **2015**, *33*, 1–4/
22. Lu, Z.; Liu, M.; Stribinskis, V.; Klinge, C. M.; Ramos, K. S.; Colburn, N. H.; Li, Y. *Oncogene* **2008**, *27*, 4373–4379.
23. Nelson, P. T.; Baldwin, D. A.; Scearce, L. M.; Oberholtzer, J. C.; Tobias, J. W.; Mourelatos, Z. *Nat. Methods* **2004**, *1*, 155–161.
24. Xianyu, Y.; Xie, Y.; Wang, N.; Wang, Z.; Jiang, X. *Small* **2015**, *11*, 5510–5514.
25. Chen, W.; Cao, F.; Zheng, W.; Tian, Y.; Xianyu, Y.; Xu, P.; Zhang, W.; Wang, Z.; Deng, K.; Jiang, X. *Nanoscale* **2015**, *7*, 2042–2049.
26. Zhou, W.; Gao, X.; Liu, D.; Chen, X. *Chem. Rev.* **2015**, *115*, 10575–10636.
27. Hauck, T. S.; Giri, S.; Gao, Y.; Chan, W. C. W. Adv. *Drug Deliv. Rev.* **2010**, *62*, 438–448.
28. Hu, R.; Liu, T.; Zhang, X. B.; Huan, S. Y.; Wu, C.; Fu, T.; Tan, W. *Anal. Chem.* **2014**, *86*, 5009–5016.

Chapter 3

Nano-Bio Computing on Lipid Bilayer

In this chapter, the complex nanoparticle network system on lipid bilayer discussed in chapter 2 were employed to operate biomolecular logic circuits. We tried to exploit the lipid for biocomputing in terms of construction, scalability, and modularity, with lipid bilayers becoming special breadboard (a construction base for electronics) for logic function-encoded plasmonic nanoparticles. On 2D fluidic platform, plasmonic nanoparticles receive the inputs in solution, process the information, change their conformation, and generate assembly and disassembly events as an output one. We systematically designed and performed diverse logic circuits with two types of logic encoding principle: (1) interfacial design, and (2) network design. A biomolecular logic computing chip using nanoparticle-lipid platform offers unique two-dimensional controllable fluidity to tethered nanoparticles. In particular, compared to the computing devices in solution state (such as DNA computing), it enables spatial confinement which widens the scope of logic gates.

This work was published in full as: Jinyoung Seo^{+}, Sungi Kim^{+}, Ha H. Park^{+}, Da Yeon Choi, and Jwa-Min Nam, "Nano-Bio Computing Lipid Nanotablet" *Science Advances*, accepted.

+ represents equal contribution.

3.1. Introduction

Across many length scales, matters have been merged with computation, from micro-sized droplets (1) and particles (2–4) to biomolecules (5–14) and molecular machines (15). However, implementing computation in nanoparticles remains unexplored, despite a wide range of applications that would benefit from algorithmically controlling their potentially useful photonic, electrical, magnetic, catalytic, and material properties that are not accessible from molecular systems (16–23). Systems of nanoparticles equipped with computing capability—nanoparticle “circuits”—can autonomously perform complex tasks in response to external stimuli, directing the flow of matter and information at the nanoscale. To date, a common approach to using nanoparticles as substrates for computation is functionalizing the particles with stimuli-responsive ligands (24–30). A group of surface-modified nanoparticles then can carry out elementary logic operations, responding to various chemical and physical inputs. Ideally, one should be able to use individual nanoparticles as modular nano-parts and implement a desired computation in a plug-and-play manner. However, the current approach has been limited to installing few logic operations that control only simple outputs, such as aggregation of particles in solution. This limitation is not because of the lack of sophistication in nanoparticles or surface ligands, but because of the difficulties in modular wiring of multiple logic gates in the solution phase, where inputs, logic gates, and outputs all diffuse uncontrollably in the three-dimensional (3D) space. Specifically, the following constraints have imposed limitations on nanoparticle computing. First, particles with information-processing functions are irreversibly altered after one operation and mixed with unreacted particles or inputs in a bulk solution. The lack of compartmentalization prevents the implementation of more than one computational task per test tube. Second, it is difficult to control or analyze structural changes, dynamic interactions, and output signals of freely diffusing particles in solution. In most cases, only an ensemble-averaged signal such as a color change of solution is obtained as a final readout, which averages out particle-by-particle responses of the computation. To construct complex yet reliable nanoparticle circuits at the level of single particles, it is necessary to go beyond solution-phase approaches and make a transition into scalable, modular platforms with in situ readout and controllability, in which a circuit of interest can be systematically constructed on the basis of digital design principles.

In nature, the cell membrane is a biological equivalent of a circuit board. Hosting a variety of receptor proteins as computational units, the membrane compartmentalizes the proteins from information-rich extracellular fluids; on the fluidic membrane surface, the receptors laterally interact with each other to carry out complex functions as a network. Each receptor, as an active constituent of the biological circuit, takes chemical and physical cues as inputs such as binding events with its ligands or changes in membrane voltage, and generates outputs such as conformational changes or dimerization/dissociation reactions; in addition, the membrane allows many different computing processes to occur in parallel (31–33).

Taking inspiration from cellular membranes, we demonstrate a lipid bilayer-based nanoparticle computing platform termed lipid nanotablet (LNT) that enables nanoparticles tethered to a supported lipid bilayer (SLB) to perform logic computation in a modular manner. To implement the computation, we use SLBs—which have been widely employed as synthetic mimics for cell surfaces (34) —as "chemical circuit boards" and program the ways tethered nanoparticles interact with one another using surface ligands. As a proof of concept, we use light-scattering plasmonic nanoparticles as circuit components, DNA as surface ligands and molecular inputs, and biotin−streptavidin interaction for tethering. Tethering of nanoparticles to a lipid bilayer provides the following features: First, nanoparticles are compartmentalized from a solution containing molecular inputs. Second, particle-to-particle interactions are confined to occur only through lateral diffusion at the fluidic two-dimensional reaction space. Third, the laterally confined nanoparticles are tracked and analyzed in situ with single-particle resolution because a large number of light-scattering nanoparticles are confined in the focal plane of dark-field microscopy (DFM). We exploit these unique features to realize an unconventional way to carry out computation with single nanoparticles. This "nano-bio" computation, which occurs at the interface of nanostructures and biomolecules, translates molecular information in solution (input) into dynamic assembly/disassembly of nanoparticles on a lipid bilayer (output).

3.2. Experimental Section

To construct lipid nanotablets (LNTs), three key components—small unilamellar vesicles (SUVs), glass flow chambers, and DNA-functionalized plasmonic nanoparticles—were first prepared. Afterward, the solution of SUVs was introduced into a flow chamber to form a SLB on its bottom glass substrate. The DNA-modified nanoparticles were then tethered to the SLB and used as logic gates and circuits for molecular information processing. Depending on their mobility on a LNT, the functionalized nanoparticles were classified into immobile receptors (reporters of computation) or mobile floaters (information carriers of computation). Receptors and floaters for Disassembly logic gates were pre-dimerized before each logic operation. Dark-field microscopy imaging was carried out to measure the performances of the nanoparticle logic gates responding to molecular inputs in solution. Dark-field image sequences obtained from the logic operations were processed and quantified by a custom-built image analysis pipeline.

Preparation of small unilamellar vesicles

The lipid solution in chloroform was mixed in a round-bottom flask to have 97.2 mol% dioleoylphosphatidylcholine (DOPC), 0.3 mol% biotinylated dioleoylphosphatidylethanolamine (DOPE), and 2.5 mol% poly(ethylene glycol) (1K)–DOPE. Chloroform was removed by a rotary evaporator, and the lipid film formed inside the flask was thoroughly dried for 15 min under a stream of N_2. The dried mixture was resuspended in deionized (DI) water to have the total concentration of 2 mg/mL. The lipid solution went through three freeze-thaw cycles between -78 ℃ and 40 ℃. To generate uniform SUVs, the solution was extruded more than 11 times through a polycarbonate membrane with a pore diameter of 100 nm at 30 ℃. The resulting SUV solution was kept at 4 ℃ until use.

Preparation of supported lipid bilayers

SLBs were prepared on glass substrates within flow chambers via the vesicle fusion method. A flow chamber was made from a top and bottom glass and a Parafilm spacer (4 mm × 50 mm × 200 µm). The working volume of the glass chamber is ~40 uL. The top slide glass (Paul Marienfeld GmbH) with inlet and outlet holes was cleaned by 5-min bath sonication in DI water and 2-min piranha etching in H_2SO_4/H_2O_2 3:1. After each cleaning procedure, glass substrates were rinsed with sufficient amounts of DI water. The cleaned top glass slide was then passivated with 10 mg/mL of bovine serum albumin (BSA) in 150 mM NaCl phosphate buffered saline (1× PBS) to prevent SLB formation on the upper side of the chamber. The bottom cover glass (Co. KG, Germany) was cleaned by 5-min sonication in DI water followed by 2-min piranha etching. A two-ply Parafilm spacer was then placed between the two glass slides and heat-sealed at 100 ℃. The freshly extruded SUV solution was diluted to 1 mg/mL in 1× PBS solution and sonicated for 15 min. The SLBs were formed by introducing the sonicated vesicle solution into the flow chamber at 30 ℃. After 60 min, the flow chamber was gently washed with DI water and 1× PBS. Defects in SLBs were then passivated with 100 µg/mL BSA in 1× PBS for 45 min. 17 nM streptavidin in 1× PBS was then injected into the flow chamber to modify the biotinylated DOPE molecules. After 40 min, the flow chamber was washed with 1× PBS twice. The flow chamber with the streptavidin-modified SLB can be stored up to 3 days in a humidified refrigerator at 4 ℃. Formation of air bubbles inside the chamber should be avoided in all procedures.

Synthesis and functionalization of plasmonic nanoparticles

Gold nanorods with silver shells, gold nanospheres, and silver nanospheres on gold seeds that exhibit red, green, and blue scattering signals were synthesized and referred to as red, green, and blue nanoparticles, respectively. For the preparation of red nanoparticles, gold nanorods with an aspect ratio of 4 were first synthesized according to previous methods based on a seed-mediated growth mechanism (*36*). 5 nm-thick silver shells were formed around the gold nanorods by incubating the gold nanorod solution (1 mL, 100 nM) with cetyltrimethylammonium chloride (CTAC) solution (1 mL, 10 mM), $AgNO_3$ (1 mL, 0.2 mM), and L-ascorbic acid (1 mL, 50 mM) for 4 hours. The resulting red nanoparticles (diameter = ~22 nm; length = ~56 nm) were washed three times by centrifugation, supernatant removal, and redispersion in DI water. Spherical gold nanoparticles (diameter = ~50 nm) were purchased from BBI Solutions (Cardiff, UK) and used as green nanoparticles. Blue nanoparticles (diameter = ~54 nm) were prepared by growing 17 nm-thick silver shells on 20-nm spherical gold nanoparticle seeds. To form silver shells on the seeds, sodium ascorbate solution (100 µL, 50 mM) was rapidly injected into the mixture containing 150 pM of 20-nm gold seeds, 0.2% polyvinylpyrrolidone (PVP), and 0.24 mM $AgNO_3$. The nanoparticles were characterized by transmission electron microscopy (TEM, JEM-2100, JEOL Ltd, Japan), UV-Vis spectrophotometer (Agilent 8453, Agilent Technologies, USA), dark-field microscopy (DFM, Axiovert 200M, Carl Zeiss, Göttingen, Germany), and field-emission scanning electron microscopy (FE-SEM, JSM-7600F, JEOL Ltd, Japan). Correlative DFM–SEM imaging was performed to analyze single-particle scattering signals from the three nanoparticles: Nanoparticles loaded on a Cr-patterned glass substrate were first imaged by DFM, treated with Pt coating (Cressington 108auto, Cressington Scientific Instruments Ltd, UK), and imaged in the same position by FE-SEM. The characterization data are summarized in fig. S2. TEM and FE-SEM imaging were carried out at the National Center for Inter-University Research Facilities and at the Research Institute of Advanced Materials (both at Seoul National University, Seoul, South Korea), respectively.

Thiolated DNA oligonucleotides (Bioneer, Daejeon, Korea) were treated with 100 mM dithiothreitol (DTT) in 100 mM pH 8.0 phosphate buffer (PB) for 1 hour. Afterward, the oligonucleotides were purified via size-exclusion chromatograph with a NAP-5 column (GE Healthcare, Buckinghamshire, U.K.). Nanoparticles (final concentration of 15 pM) were incubated with 216 nM (for blue nanoparticles) or 288 nM (for red and green nanoparticles) of the thiolated oligonucleotides for 1 hour at 25 ℃. The ratios of biotinylated DNA linkers to total surface DNA ligands were 0.5%, 0.5%, 0.5%, 35%, 35%, and 50 % for R-NF, G-NF, B-NF, R-NR, G-NR, and B-NR, respectively. The solution was then adjusted to 0.1% (w/v) PVP in 10 mM PB for red nanoparticles, to 0.1% (w/v) sodium dodecyl sulfate (SDS) in 10 mM PB for green nanoparticles, and to 10 mM PB for blue nanoparticles. Three aliquots of 1 M NaCl, 0.1% SDS, and 10 mM PB salt solution were added with a 1-hour interval to achieve a final concentration of 0.3 M NaCl. After each salt addition, the mixture was heated at 50 ℃ for 10 min and incubated at 25 ℃ for 50 min. 2 hours after reaching the final concentration, the red nanoparticle solution was centrifuge-washed and redispersed in 1× PBS. Other nanoparticle solutions were incubated for 12 hours, centrifuge-washed, and redispersed in DI water (green nanoparticles) or in 1× PBS (blue nanoparticles).

Oligonucleotide Design

Nanoparticles were functionalized with single-stranded DNA strands that contain thiol modifications at their 3’ or 5’ ends. DomainDesign (*44*, *45*) was used to generate a set of orthogonal 10 nt toeholds, 10 nt supporting domains, 14 nt binding domains, and 34 nt linker domains. These sequences were then verified by NUPACK (*46*) and further optimized if any undesirable interaction was detected during experiments. The thiolated DNA strands include: (a) biotinylated linker DNA strands used for the tethering of nanoparticles to streptavidin-modified SLB surfaces and (b) ligand DNA strands directly involved in the nanoparticle computing process. A linker strand with 5'-thiol modification contains (*i*) an A_{15} domain after a 5'-thiol group, (*ii*) six ethylene glycol (EG) units (a PEG moiety), and (*iii*) a linker domain followed by biotin modification. A linker strand with 3'-thiol modification (with biotin modification at 5' end) contains (*i*) a linker domain, (*ii*) a PEG moiety, and (*iii*) an A_{15} domain followed by 3'-thiol modification. Ligand DNA strands are categorized into two types: 'normal' single-stranded DNA strands that do not form hairpin loops and hairpin-type DNA ligands used in Assembly AND gate. The normal ligand type is further classified into two groups, one with 3'-thiol modification and another with 5'-thiol modification. A ligand with 5'-thiol modification contains (*i*) an A_{15} domain after 5'-thiol, (*ii*) a PEG moiety, (*iii*) a supporting domain, and (*iv*) a binding domain. A ligand with 3'-thiol modification contains (*i*) a binding domain, (*ii*) a supporting domain, and (*iii*) a PEG moiety, and (*iv*) an A_{15} domain followed by 3'-thiol modification. Unless otherwise noted, receptor and floaters were functionalized with 3' thiol ligands and 5' thiol ligands. Hairpin-type DNA ligands were thiolated at 5' end. Supporting domains are introduced to better expose binding domains to solution, thereby promoting the hybridization of the binding domains with input strands. The A_{15} domain and PEG moiety in each strand are essential parts of the design, as these two components enhance DNA hybridization on nanoparticle surfaces and decouple functional units (binding domains) from a core structure (nanoparticle) by providing optimal DNA density, reducing non-specific interactions, and stretching out the binding domain. Sequences of thiolated strands are listed in table S2.

Operation and characterization of nanoparticle circuits on lipid nanotablets

A solution containing ~3 pM of DNA-modified nanoparticles with biotinylated linkers was introduced to a flow chamber, whose bottom glass substrate was coated with a streptavidin-modified lipid bilayer. The solution was incubated from 1 to 5 min to result in a desired particle density. The particle density was linearly proportional to incubation time **(fig. S5)**. After the particle loading, the LNT was washed with 1× PBS twice. The tethered nanoparticles then functioned as logic gates, taking single-stranded DNA inputs in 1× PBS buffer. Performance of each nanoparticle circuit was tested by injecting 500 μL of an input solution into the flow chamber during dark-field imaging. The input solution was injected slowly while a user was monitoring the field of view, such that a flow introduced from the injection did not alter the initial position of receptors. Dark-field imaging was carried out at room temperature by a commercial dark-field microscope with a 40× objective lens (NA 0.6) and AxiCam HRC color camera on an optical table (Dail Systems, South Korea). The field of view was 180 × 180 μm^2. Prior to input injection, 31 images were acquired with a time step of 200 ms to identify the positions and signals of receptor nanoparticles. Circuit performance was recorded during and after input injection with imaging interval of 2.5 s. The recording continued until the responses of the circuits reached a plateau. Both image sequences were acquired at a fixed position. Sequences of input strands and experimental conditions for logic gate operation are listed in table S3.

Analysis of dark-field time-lapse images

Images obtained from time-lapse dark-field imaging were analyzed by custom MATLAB code to quantify how nanoparticle circuits respond to molecular inputs. Images were first registered by StackReg plugin in ImageJ. To avoid sampling bias resulting from uneven focus and illumination across the field-of-view (that were typically observed along the image boundaries), An area of interest (128 × 128 μm^2) was then chosen for the analysis. Afterward, the drift-corrected image sequences were processed by an image analysis algorithm that enables single-particle tracking and signal classification. The single-particle tracking algorithm consists of the following three steps: (*i*) In signal detection step, spots (pixels) with signals considerably higher than threshold intensity were identified using a pixel-based intensity threshold. The contours obtained from the detected pixels enabled the segmentation of each nanoparticle signal. (*ii*) In particle localization step, the representative position of each segmented signal was determined. Each localized nanoparticle was assigned with an intensity value obtained from averaging pixel intensities from 3 × 3 pixels around the localized position. (*iii*) In particle tracking step, nanoparticle signals, whose positions remained unchanged for entire imaging duration, were identified as receptor signals. Time traces of all receptor signals identified in the chosen field-of-view were obtained and used as a signal profile of each image sequence. The signal profile was then used to generate a receptor-only image sequence. The algorithm is described in details in fig. S6. In classification step, only the receptors that exhibit step-function-like signal traces were identified as output-generating particles. Transient interactions (short, sharp increase or decrease of a receptor signal) that resulted from temporary co-localizations of two nanoparticles in diffraction-limited spots were filtered out. Any intensity changes that do not last until the end of imaging were excluded. To reliably categorize the nanoparticle reaction types, a signal profile of red, green, and blue nanoparticles shown in fig. S7 was used as a standard. Ambiguous signals that did not fall in the red, green, and blue signal clusters in the standard signal profile were excluded. Afterward, RGB scattering signals of the receptor were further analyzed to identify the floater with which the identified receptor reacted. The entire analysis process is operated in a MATLAB-based graphical user interface program **(fig. S6D)**.

For each logic gate, a time-versus-output relationship was plotted to reveal accuracy and kinetics of the logic gate computation. Output counts of the plot was obtained by cumulatively counting the number of receptors that generated correct outputs over time. To minimize the effect by the variability in particle populations, the final output counts were normalized for each type of logic gate. For example, the output counts measured for the analysis of a two-input AND gate were normalized across the four input conditions (0 AND 0, 0 AND 1, 1 AND 0, and 1 AND 1). For Assembly gates, output counts were normalized by the number of floaters detected in initial 31 images. For Disassembly gates, output counts were normalized by the number of dimers formed in the pre-dimerization step. ON/OFF levels were calculated by dividing the lowest output count obtained in TRUE conditions by the highest output count obtained in FALSE conditions. If the output count in FALSE conditions was 0, the value was set to be 1.

Diffusion behaviors of nanoparticles were analyzed as follows: (*i*) particles were tethered to a SLB with a sufficiently low particle density (~200 particles per 180 × 180 μm^2) that allowed long-term tracking (~10 min) without trajectory overlap. (*ii*) Nanoparticle signals from each frame were detected and localized by the image analysis algorithm. (*iii*) Determined positions were used to generate a trajectory of each particle, which was then used to calculate its diffusion coefficient. Mean square displacement (MSD) values as a function of time interval were obtained for each particle. The MSD plots of these trajectories were fitted to the equation, $<r^2> = 4Dt$, where $<r^2>$ is the MSD, D is the diffusion coefficient, and t is the time interval.

3.3. Results and Discussion

A lipid bilayer as a circuit board for nanoparticle-based logic computation

A key component of an LNT is a flow chamber, of which the bottom substrate is coated with a lipid bilayer. Nanoparticles, whose optical signals, mobility, and surface DNA ligands are readily controllable, are biochemically tethered to the lipid bilayer surface via biotin−streptavidin interaction and monitored by DFM (Fig. 1A and fig. S1). The tethering of nanoparticles enables facile exchanges of input solutions through the flow chamber without washing out the computing elements on the SLB surface. We use three types of core particles with distinct light-scattering spectra: gold nanorods with silver shells, gold nanospheres, and silver nanospheres on gold seeds that exhibited red, green, and blue scattering signals, respectively (fig. S2). These particles are referred to as red, green, and blue nanoparticles. We prepare two classes of nanoparticles—receptor (R) and floater (F)—that differ in diffusion coefficients. Receptors are immobile on SLBs because their lateral diffusion is limited by a large number of biotinylated DNA linkers that strongly interact with streptavidins on a SLB. The biotinylated linkers functionalize 34% to 50% of the receptor surface valency. Floaters, whose linker density was 0.5%, were highly mobile on SLBs with a diffusion coefficient of ~1.0 $\mu m^2/s$ (fig. S3). As a result of the mobility, floaters actively interact with receptors across space and time, functioning as active units of computation. In this study, we use six types of nanoparticle circuit elements with distinct optical and kinetic states: red nano-receptors (R-NRs), red nano-floaters (R-NFs), green nano-

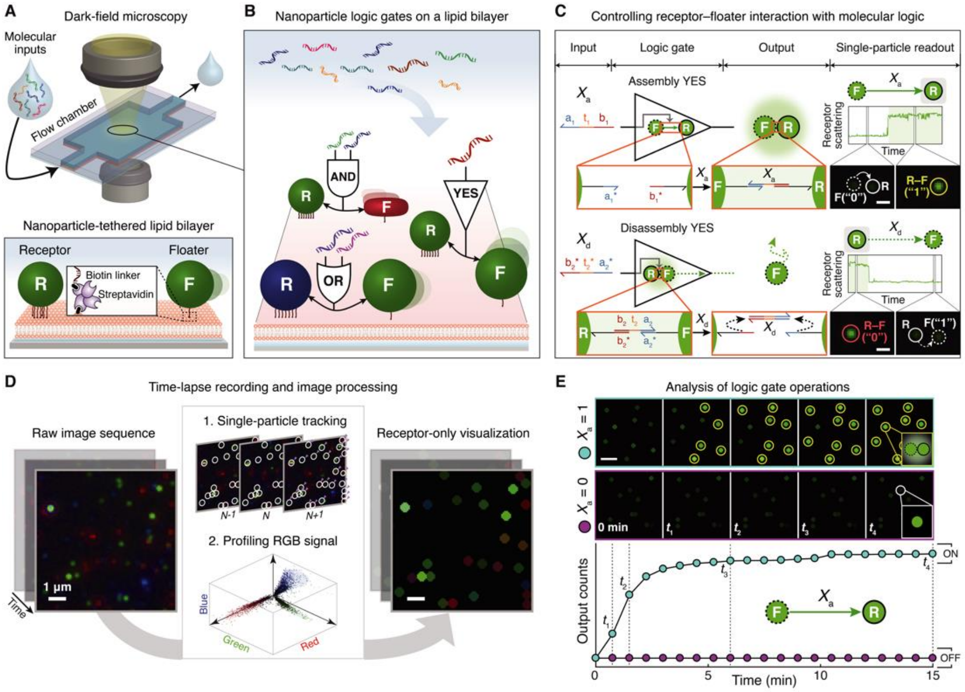

Fig. 1. Single-nanoparticle logic computation on lipid nanotablets. (**A**) Schematics of lipid nanotablet platform. Two types of DNA-modified nanoparticles, immobile receptor (R) and mobile floater (F), are tethered to a supported lipid bilayer and monitored by dark-field microscopy. (**B**) Receptor–floater pairs as nanoparticle Boolean logic gates. Each logic gate takes DNA as inputs and yields either an assembly or a disassembly between the two particles as an output. Bidirectional arrows denote R–F interactions. Surface DNA ligands are not depicted. (**C**) Single-nanoparticle YES gates. An R–F pair acts as an Assembly YES gate when the floater binds to the receptor in response to an input DNA X_a. An R–F dimer is a Disassembly YES gate when an input X_d promotes a disassembly reaction of the dimer via toehold-mediated strand displacement. The assembly/disassembly reactions, represented by directed graph, result in step-function-like changes in receptor signals as optical readout. Functional domains are represented by color and subscripted numbers with arrowheads indicating their 3' ends. Asterisks denote complementarity. Glowing circles behind R–F dimers illustrate plasmonic coupling. Scale bar is 1 μm. (**D**) Image analysis. A single-particle tracking algorithm first identifies receptor signals from a raw image sequence. Afterward, the detected signals are sampled and used to generate a new dark-field movie that visualizes only receptor signals. (**E**) Kinetics analysis. Receptor-only snapshots (top) and a kinetics plot (bottom) of the Assembly YES gate are provided for each input condition. A kinetics plot is obtained by cumulatively counting the number of state-switching receptors over time. Scale bar is 4 μm.

receptors (G-NRs), green nano-floaters (G-NFs), blue nano-receptors (B-NRs), and blue nano-floaters (B-NFs). The surface DNA ligands mediate a receptor–floater interaction, taking DNA molecules as inputs and inducing the binding or unbinding of the receptor–floater complex as an output, only when the molecular inputs meet a Boolean logic condition (Fig. 1B).

Actions of a single floater are intrinsically binary. For a given observation period, a floater either discretely switches its state (through assembly or disassembly), or it does not. Thus, controlling the "digital" actions of each floater with Boolean logic allows a receptor–floater pair to be treated as a logic gate. For the inputs of the single-nanoparticle logic gate, the logic values "0" and "1" represent the absence and presence of an input DNA in solution, respectively. For outputs, logic values are assigned to floaters and indicate whether a floater changes its state: "0" indicates a floater in its initial state, whereas "1" represents a floater whose state is switched as a result of an assembly or a disassembly reaction. Single-nanoparticle YES gates are of the simplest examples (Fig. 1C). In the Assembly YES gate, a G-NF switches its state from a diffusible monomer ("0") to an immobile dimer ("1"), through association with a G-NR in response to a single-stranded DNA input X_a that can hybridize with surface DNA ligands of the two particles. In the Disassembly YES gate, a G-NF is initially bound to a G-NR via hybridization with an oligonucleotide X_d*. The process to form receptor–floater dimers for Disassembly gates is termed pre-dimerization. When a DNA input X_d is introduced, it first binds to the partially hybridized X_d* through a single-stranded toehold domain (t_2) and removes the preformed DNA "bond" (X_d*) from the receptor–floater interface by fully hybridizing it. As a result, the G-NF is released from the G-NR, switching its state from an immobile dimer ("0") to a diffusible monomer ("1"). We use this process, known as toehold-mediated strand displacement (*35*), to design nanoparticle Disassembly logic gates, because this simple mechanism enables robust control of DNA-modified nanoparticles using molecular interactions alone (see fig. S4 for further details). Disassembly reactions require input molecules to penetrate receptor–floater interfaces densely packed with surface DNA ligands for interactions with toehold domains, whereas assembly reactions are simply driven by collisions between receptors and floaters that are modified with input strands. Assembly reactions are thus kinetically favorable than disassembly reactions. We use relatively high input concentration for disassembly reactions to compensate the difference in kinetics. To represent behaviors of logic-gated nanoparticles in a simple diagram, we use "nanoparticle reaction graph" abstraction. This abstraction is based on directed graph where a node is represented by a nanoparticle and an edge is represented by logic, inputs, and reaction type. We depict an assembly reaction by a solid arrow directed from a floater to a receptor and a disassembly reaction by a dashed arrow from a receptor to a floater, as shown in Fig. 1C. The use of directed graph provides an intuitive view on how each nanoparticle logic gate behaves.

To analyze the state-switching behaviors of floaters, we monitor the signal changes of receptors, whose stationary positions allow facile monitoring of assembly and disassembly events. On LNT platform, receptors are used as optical reporters of computation that provide single-particle-level, digital signal readout. For example, the Assembly YES gate produces output “1” when a G-NF assembles onto a G-NR through X_a. As shown in the time trace of a receptor scattering signal and its associated DFM images in Fig. 1C, the assembly process results in a plasmonic coupling-induced, step-function-like increase in green intensity of the G-NR. The real-time operations of two YES gates are described in movie S1 (Assembly YES) and movie S2 (Disassembly YES). Scattering signals of a nanoparticle logic gate depend on plasmonic coupling between two core particles that compose the gate (*36*); for a given assembly or disassembly reaction, there are nine different patterns of scattering signal changes based on combinatorial plasmonic couplings induced by three distinct floaters (R-NF, G-NF, or B-NF) binding to three different receptors (R-NR, G-NR, or B-NR). Thus, multiple nanoparticle logic gates can be implemented and analyzed in parallel as long as each gate provides a distinct optical readout. A sufficiently high density of nanoparticles is maintained to ensure that a large number of logic-gated nanoparticle reactions can occur within a short period of time. Approximately over 4,000 nanoparticles (>3,700 receptors and 300 floaters) are tethered to an area of 180 × 180 μm^2 for computing processes that typically last 15 to 30 min (fig. S5). We set the number of receptors to be higher than that of floaters to minimize trimer and tetramer formation. This condition allows the floaters to switch exclusively between the monomer and dimer states.

To rapidly and reliably process the dark-field imaging data, we introduce an image analysis pipeline that enables detection, tracking, and visualization of nanoparticle signals (Fig. 1D and fig. S6). The key to the analysis pipeline is our single-particle tracking algorithm that is capable of identifying and tracing signals from receptor particles in the high-density setting. Using the single-particle tracking algorithm, we profile the scattering signals of the receptors from a raw dark-field image sequence, and generate a new movie whose each frame visualizes only the receptor signals in a dark background. This process allows the receptor signals to be clearly segmented from the background and distinguished from each other, providing a clear view of how nanoparticle circuits operate at the single-particle level in real-time **(movie S3)**. During experiments, we used this receptor-only visualization to qualitatively estimate the overall computing performance of a nanoparticle logic gate. We also apply the algorithm to profiling the signals of the red, green, and blue core nanoparticles. The signal profile, where single-particle signals of the three core particles are visualized in 3D space of a red-green-blue (RGB) scatter plot, shows three distinct red, green, and blue signal clusters **(fig. S7)**. We use the 3D signal profile to filter out ambiguous signals that do not fall in the three signal clusters from subsequent analysis.

To quantitatively analyze the computing performance of nanoparticle logic gates, we perform kinetics analysis. By cumulatively counting the number of receptors that correctly exhibit monomer-to-dimer (for Assembly gates) or dimer-to-monomer (for Disassembly gates) transitions over time, we obtain the kinetics plots of assembly or disassembly outputs. The time-versus-output plots provide quantitative information on how accurately and fast logic gates respond to different combinations of molecular inputs. For example, the performance of an Assembly YES gate responding to two different input conditions is shown in Fig. 1E. As shown in the dark-field snapshots and the plot, the number of dimerization events between G-NRs and G-NF increases over time only in the presence of the input X_a (input = 1). This result indicates that the population of the nanoparticle logic gate switches into ON state (output = 1) in response to X_a, performing YES logic operation. To accurately perform computations, a population of nanoparticle logic gates should produce high output counts only when the molecular inputs meet TRUE conditions.

Design and construction of single-nanoparticle logic gates

We first demonstrate four types of two-input single-nanoparticle logic gates: Assembly AND, Assembly OR, Disassembly AND, and Disassembly OR gates. To construct these gates, we program receptor–floater interfaces in such a way that DNA bonds at the interfaces are formed (via assembly) or cleaved (via disassembly) only if two different DNA inputs satisfy AND or OR logic. We term this approach “interface programming”. In the two-input Assembly AND gate, conformation-switchable DNA hairpins are used as surface ligands; a G-NR (R_1) and a G-NF (F_1) are each modified with a 5’-thiolated DNA hairpin that hides its binding domain in the stem (Fig. 2A and fig. S8A). Through hybridization with an input strand on its loop domain (t_1 on F_1; t_2 on R_1), the hairpin is opened and exposes the binding domain (b_1*-a_1* on F_1; a_1-b_1 on R_1). R_1 and F_1 assemble only if X_1 and X_2 are both present in the solution (movie S4). In the two-input Assembly OR gate, a G-NR (R_2) and a B-NF (F_2) are each modified with two types of DNA ligands; each particle provides two distinct binding domains (a_2*, a_3* on F_2; b_2*, b_3* on R_2) (Fig. 2B and fig. S8B). Either X_3 or X_4 can hybridize with the binding domains on F_2 and R_2, resulting in dimerization (movie S5). In the two-input Disassembly AND gate, a G-NF (F_3) is initially bound to a B-NR (R_3) by two different DNA bonds, each of which exposes a toehold domain at the R_3–F_3 interface (Fig. 2C and fig. S8C). The toehold domains t_5 and t_6 both act as recognition regions, recruiting input strands X_5 and X_6, respectively. Each input

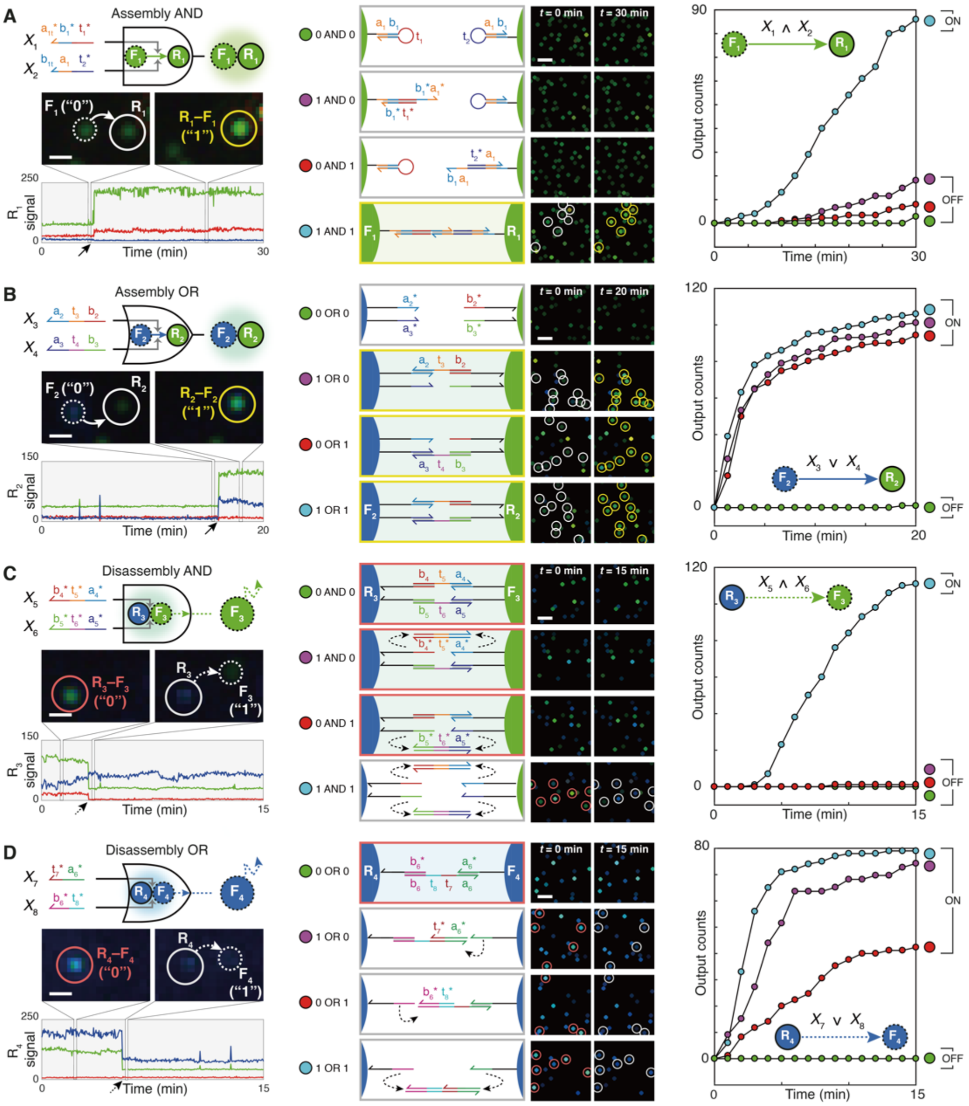

Fig. 2. Nanoparticle logic gates. (**A**) Two-input Assembly AND. (**B**) Two-input Assembly OR. Assembly of G-NFs (F_1) onto G-NRs (R_1) and B-NFs (F_2) onto G-NRs (R_2) were traced as outputs for the AND and OR gates, respectively. (**C**) Two-input Disassembly AND. (**D**) Two-input Disassembly OR. Releases of G-NFs (F_3) and B-NFs (F_4) were traced as outputs for the Disassembly AND and OR gates, respectively. Each nanoparticle species is distinguished based on its signal (color), mobility (R or F), and function (subscripted number). Domains a_{1t}* and b_{1t} (3 nt) are truncated versions of a_1* and b_1 (6 nt), respectively. First column: circuit diagram (upper), actions of a single-nanoparticle logic gate in a logical TRUE condition (middle), and the time trace of a receptor signal (lower). Solid and dashed

arrows in the x-axis indicate monomer-to-dimer and dimer-to-monomer transitions of receptors, respectively. Scale bar is 1 μm. Second column: domain-level illustrations (left) and population-level responses (right) of the logic gates. Scale bar is 4 μm. Receptors are marked with white circles before assembly (red circles before disassembly) and yellow circles after assembly (gray circles after disassembly). Third column: kinetics analysis. Each plot contains a reaction graph that corresponds to a logic gate. ∧ and ∨ denote the logic symbols for AND and OR, respectively. Legends are represented as truth tables. DNA sequences and experimental conditions are listed in tables S2 and S3. Experiments were carried out at 25°C in 1× PBS buffer.

removes a DNA bond via strand displacement. Only when the two DNA bonds are all removed by X_5 and X_6, the disassembly reaction is initiated (movie S6). In the two-input Disassembly OR gate, a B-NF (F_4) is bound to a B-NR (R_4) via a DNA bond that exposes two toehold domains t_7 and t_8 at the interface, and either of the two domains can independently recruit an input strand X_7 or X_8 (Fig. 2D and fig. S8D). This design enables each input strand, whose sequence domains are complementary to a half of the preformed DNA bond, to cleave the bond through strand displacement. Thus, either X_7 or X_8 induces the release of F_4 (movie S7). The design principles for the interface programming are straightforward and generalizable (fig. S9).

We monitor the operations of the four elementary logic gates in real-time using DFM. Single-particle snapshots of each logic gate responding to a logical TRUE condition (1 AND 1 for AND gates and 1 OR 1 for OR gates) are provided in the first column of Fig. 2. The representative time traces of the receptor scattering signals show that each two-input gate exhibits a distinct optical readout. The change in a receptor signal is largely determined by a floater signal: Reactions with G-NFs result in an increase or a decrease in green scattering intensity of receptors (shown in Fig. 2A, C), and reactions with B-NFs lead to changes in both green and blue intensity (shown in Fig. 2B, D). As the four logic gates all produce spectrally distinct signals, we can in principle operate the four gates simultaneously. Furthermore, operations of the logic gates captured in a large field-of-view are shown in the third column of Fig. 2. The images were processed to visualize only receptor signals. For each logic gate, we can readily determine whether or not the logic gate responds to molecular inputs by simply comparing the first and the last frames of a processed movie.

We quantify the kinetics of the two-input logic gates by counting their particle-by-particle responses over time. All four logic gates—Assembly AND, Assembly OR, Disassembly AND, and Disassembly OR—generate low output counts under the logical FALSE conditions and high output counts under the TRUE conditions, providing ON/OFF levels over 5 folds, 88 folds, 93 folds, and 42 folds with fast response kinetics ($t_{1/2} < 19$ min, $t_{1/2} < 5$ min, $t_{1/2} < 9$ min, and $t_{1/2} < 5$ min), respectively. We calculate ON/OFF levels by dividing the lowest output count obtained in TRUE conditions by the highest output count obtained in FALSE conditions. The $t_{1/2}$ of a nanoparticle logic gate is obtained by measuring the amount of time needed for half of its floaters to correctly respond to molecular inputs in TRUE conditions. The response rate (%), defined as the number of floaters that react to inputs divided by the total number of floaters, is ~80% in TRUE conditions (table S1). Given that ~10% of floaters inevitably participate in multimer formations (fig. S5D), the measured response rates suggest that over 90% of floaters eventually exhibit state-switching behaviors. The Assembly AND gate exhibit a small number of incorrect output signals at 1 AND 0 and 0 AND 1 conditions, presumably because the surface hairpins are in dynamic equilibrium between closed and opened states. Despite the minor leakage, the hairpin-based particle assembly is exclusively driven by input-induced hairpin opening (fig.

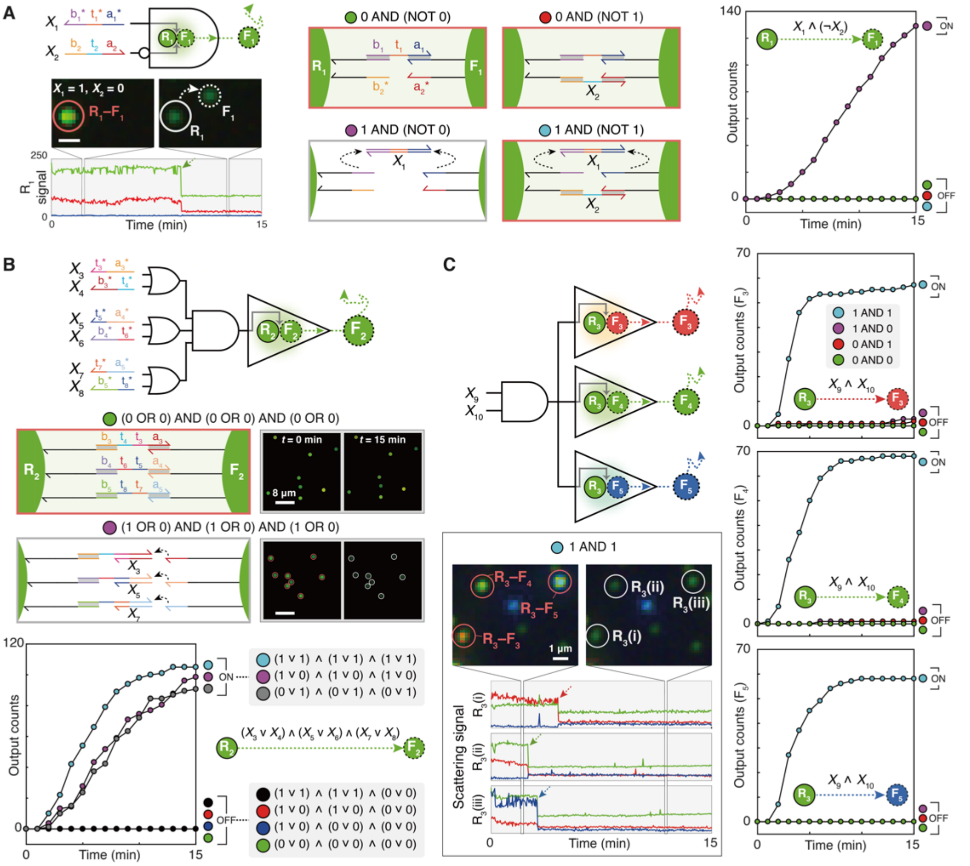

Fig. 3. Circuits with an INHIBIT logic gate, multiple inputs (fan-in), or multiple outputs (fan-out). (**A**) A two-input Disassembly INHIBIT gate implemented in a pair of G-NR (R_1) and G-NF (F_1). X_1 removes a preformed DNA bond via strand displacement, whereas X_2 forms a different DNA bond. Disassembly of the R_1–F_1 dimer is controlled by INHIBIT logic (X_1 AND NOT X_2) based on the two competing reactions. Actions of single-particle INHIBIT gate are shown. Scale bar is 1 μm. (**B**) A six-input Disassembly gate implemented in a pair of G-NF (R_2) and G-NF (F_2). The receptor (R_2) and the floater (F_2) are connected by three distinct DNA bonds, and the cleavage of each bond is controlled by two-input OR logic. (**C**) A two-input Disassembly AND gate with three outputs. This circuit evaluates two-input AND logic and generates three different mobile floaters R-NF (F_3), G-NF (F_4), and B-NF (F_5) as outputs. Three representative receptors that release F_3, F_4, and F_5 are labeled as R_3(i), R_3(ii), and R_3(iii), respectively. Dashed arrows in time traces indicate disassembly reactions. The range of y-axis values in the time traces is 0–250. ∧, ∨, and ¬ denote the logic symbols for AND, OR, and NOT, respectively. Legends are represented as truth tables. DNA sequences and experimental conditions are listed in tables S2 and S3. Experiments were carried out at 25°C in 1× PBS buffer.

S10A) and occurs without interfering with other hybridization events (fig. S10B). Notably, the two-input Disassembly OR gate exhibit uneven responses, where the 0 OR 1 condition results in a response rate of 42% that is notably lower than those of other two TRUE conditions (74% in the 1 OR 0 condition and 79% in the 1 OR 1 condition). We attribute this result to the difference in the density of surface ligands between receptors and floaters (fig. S11). Additionally, we show that the computing architecture of LNTs is compatible with a "dual-rail" convention, where the Boolean values of a logic gate are represented by the presence of either one signal ("0") or another ("1"). This formalism is frequently used for systems where it is difficult to directly introduce NOT function (*8*, *10*, *12*). With this representation, AND and OR gates are sufficient to compute any Boolean functions. We demonstrate a two-input dual-rail NAND gate as a proof of concept (fig. S12).

Next, the interface programming approach is expanded to enable nanoparticle logic gates to process INHIBIT logic [X_1 AND (NOT X_2)], take multiple inputs (fan-in), and generate multiple outputs (fan-out). First, we implement a two-input Disassembly INHIBIT gate (Fig. 3A). To realize the NOT logic required for the INHIBIT gate, we exploit competition between DNA bond elimination (triggered by X_1) and formation (triggered by X_2). The INHIBIT gate releases a G-NF (F_1) as an output, only when the disassembly input X_1 is present and the assembly input X_2 is absent (fig. S13A and movie S8). The INHIBIT gate generates outputs only in the TRUE states with an ON/OFF level over 129 folds ($t_{1/2}$ < 10 min). No output leakage is observed when both inputs are present, indicating that the bond formation by X_2 is faster than the bond removal by X_1. In addition, the two competing reactions proceed without interfering with each other (fig. S13B). Demonstration of the INHIBIT gate is of significance because two-input AND, OR, and INHIBIT operations constitute a functionally complete set of Boolean functions. Second, we construct a multi-input Disassembly gate by increasing the number of distinct DNA bonds in a receptor–floater dimer. When the release of a G-NF (F_2) from a G-NR (R_2) requires the disconnection of three different DNA bonds and each disconnection is controlled by two-input OR logic, the disassembly is regulated by a six-input expression (X_3 OR X_4) AND (X_5 OR X_6) AND (X_7 OR X_8) (Fig. 3B). Representative domain-level illustration and dark-field snapshots of the six-input logic gate responding to a FALSE condition [(0 OR 0) AND (0 OR 0) AND (0 OR 0)] and a TRUE condition [(1 OR 0) AND (1 OR 0) AND (1 OR 0)] are provided. Dark-field time-lapse imaging confirms that the six-input logic gate produces outputs only in the TRUE states with an ON/OFF level over 88 folds ($t_{1/2} < 9$ min) (fig. S13C and movie S9). The two strategies based on competing reactions and increased "bond orders" can be combined to yield Disassembly gates with complex multi-input Boolean logic, such as (X_1 OR X_2) AND [NOT (X_3 OR X_4)] and (X_1 AND X_2) AND (NOT X_3) (fig. S14). Third, we demonstrate the fan-out of a logic gate by implementing identical two-input Disassembly AND logic in three different receptor–floater pairs, each of which has a spectrally distinct floater signal (Fig. 3C). The disassembly reactions of the three floaters is readily analyzed owing to plasmonic coupling between the receptors and the floaters; the dissociations of R-NF (F_3), G-NF (F_4), and B-NF (F_5) from the receptors result in decreases in red, green, and blue intensities of the receptor signals, respectively (movie S10). The Disassembly gate with fan-out releases all three outputs according to the AND logic, with ON/OFF levels over 20 folds ($t_{1/2} <$ 6 min).

Modular wiring of nanoparticle logic gates into a circuit

As the complexity of reactions at a receptor–floater interface increases, incomplete reactions or spurious interactions arise as well. Thus, relying on the programming of particle interfaces is not a scalable strategy for constructing complex circuits. Instead, we introduce a conceptually distinct approach—the nanoparticle "network programming"—that enables any two single-particle logic gates to be combined with AND or OR logic. According to nanoparticle reaction graph abstraction, a nanoparticle logic gate is represented by a graph composed of two nodes and one edge. Through network programming, two edges, each of which represents an assembly or disassembly reaction, are connected by a floater node. This process is equivalent to the coupling of two nanoparticle reactions and thus enables more complex logic operations to be implemented at the level of nanoparticle network. Joining a Disassembly edge (Gate 1) with an Assembly edge (Gate 2) represents the wiring of the two gates with AND logic, and linking two Disassembly edges (Gate 3 and 4) symbolizes the wiring of the two gates with OR logic.

First, we demonstrate the wiring with AND logic by allowing a floater to be used in a Disassembly gate and an Assembly gate in series. We design a two-input Disassembly AND gate composed of a G-NR (R_1) and a G-NF (F_1) in such a way that the F_1 acts as a Assembly YES gate with another receptor B-NR (R_2) after dissociated from the R_1 (Fig. 4A). In this network-level wiring scheme, the formation of an R_2–F_1 dimer then becomes an output of the AND-AND cascade circuit (X_1 AND X_2) AND X_3 (fig. S15A and movie S11). The circuit is described by a reaction graph, where two receptors (R_1 and R_2) are serially connected to a floater (F_1). Dark-field imaging reveals that the circuit provides an ON/OFF level of 36 folds. The intermediate disassembly reactions could also be analyzed owing to their distinct optical signals. The upstream Disassembly AND gate results in an ON/OFF level over 89 folds. Further, we quantify how F_1 population changes over time by subtracting the number of receptors from the total number of detected nanoparticles in each frame. The population dynamics of F_1 shows that the released F_1 subsequently binds to R_2 only if the input X_3 is present. For (1 AND 1) AND 1 condition, over 92% of released F_1 responds to the assembly input X_3. This result indicates that the sequential disassembly–assembly cascade is highly efficient. In addition, the accumulation of F_1 population in (1 AND 1) AND 1 indicates that the assembly reaction is relatively slower than the disassembly reaction in this case. The reversal of the reaction kinetics observed in this condition arises presumably because the access of input X_3 is temporarily hindered by DNA strands hybridized on the floater. Other two-input Disassembly gates, such as two-input OR and

INHIBIT gates, could be modularly rewired, resulting in an OR-AND cascade circuit (fig. S16A) and an INHIBIT-AND cascade circuit (fig. S16B). Second, we implement OR wiring by designing two Disassembly gates to produce floaters with identical optical signals (Fig. 4B). We install a two-input Disassembly AND gate [composed of a B-NR (R_3) and a G-NF (F_2)] and a Disassembly YES gate [composed of a G-NR (R_4) and another G-NF (F_3)] in parallel. In the circuit (X_4 AND X_5) OR X_6, G-NFs can be produced from either the AND gate or the YES gate; the two gates are thus wired with OR logic (fig. S15B and movie S12). The AND-OR cascade circuit results in an ON/OFF output level of 55 folds. We also evaluate the operations of the two upstream Disassembly gates separately, showing that the two gates carried out computation with high ON/OFF levels without interfering with each other. A two-input Disassembly OR gate can be also wired with a Disassembly YES gate to yield an OR-OR cascade circuit (fig. S17). Taken together, our results indicate that the network programming strategy can be readily applied to implementing complex multilayer cascades without extensive optimization.

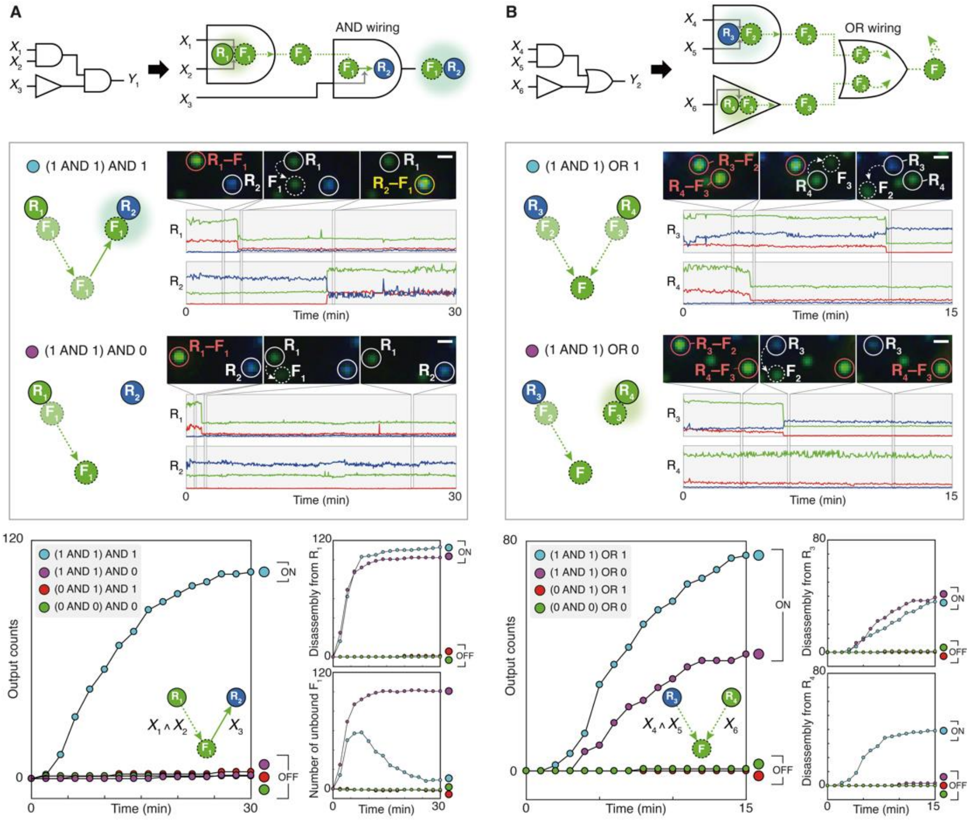

Fig. 4. Wiring of nanoparticle logic gates via network programming. (**A**) Wiring with AND logic. Two logic gates (Disassembly AND gate and Assembly YES gate) are designed to operate in series for AND wiring. A floater F_1, which is bound to the first receptor R_1 in its initial state, acts as a Disassembly AND logic gate and subsequently as an Assembly YES gate with the second receptor R_2. The generation of R_2–F_1 dimers is an output of the (X_1 AND X_2) AND X_3 circuit. (**B**) Wiring with OR logic. Two logic gates (Disassembly AND gate and Disassembly YES gate) are designed to operate in parallel for OR wiring. The two gates both release G-NFs as outputs. The generation of the G-NFs is an output of the (X_3 AND X_4) OR X_5 circuit. Circuit diagrams (upper), single-particle dark-field analysis (middle), and kinetics analysis of circuits (lower left) and intermediate reactions (lower right). Scale bar is 1 µm. Legends are used as truth tables. DNA sequences and experimental conditions are listed in tables S2 and S3. Experiments were carried out at 25℃ in 1× PBS buffer.

A nanoparticle multiplexer circuit on a lipid bilayer

To demonstrate the modularity of nanoparticle computing on LNT platform, we implement a multiplexer circuit (MUX2to1) by rewiring previously introduced logic gates via network programming. The multiplexer takes a selector input (*Sel*) to select one of two inputs X_1 and X_2 and translates the selected input into a single output (Fig. 5A). The multiplexer circuit is designed by connecting a Disassembly INHIBIT gate (X_1 AND NOT *Sel*) and a two-input Disassembly AND gate (*Sel* AND X_2) with OR logic. This circuit diagram is translated into a reaction graph diagram that subsequently guides the design of surface DNA ligands for each nanoparticle. A multiplexer circuit is composed of two receptor–floater pairs, R_1–F_1 and R_2–F_2, whose interfaces can evaluate (X_1 AND NOT *Sel*) and (*Se*l AND X_2) operations, respectively. Both producing G-NFs as outputs, the two Disassembly gates are wired with OR logic. Notably, the multiplexer circuit requires identical selector inputs to be simultaneously processed by two different logic operations—INHIBIT logic (by R_1–F_1 pair) and AND logic (by R_2–F_2 pair) (fig. S18). Under this design constraint, F_1 and R_1 should expose sequence domains a_2 and b_2 that are fully complementary to surface ligands on F_2 and $R_{2,}$ respectively (Fig. 5B). In solution phase, these nanoparticles would spontaneously form aggregates; F_1 can bind to F_2 through complementary binding domains a_2 and a_2*. The multiplexer circuit, however, could be constructed on a lipid bilayer without such issues because the undesirable, spontaneous interactions between the nanoparticles are compartmentalized and controlled during circuit preparation steps: F_1–F_2

interaction is inhibited by temporary protection of the a_2* domain (introduced before the tethering of F_1), and R_1 and R_2 do not collide with one another because of their immobility on SLBs. After the four circuit components are all loaded on the lipid bilayer, two Disassembly logic gates are prepared by forming the R_1–F_1 and R_2–F_2 dimers. As shown in Fig. 5C and movie S13, the nanoparticle multiplexer yields the expected responses to the eight different input combinations with an ON/OFF level over 35 folds. The output counts of the multiplexer come from either a Disassembly INHIBIT gate (R_1–F_1) or a Disassembly AND gate (R_2–F_2). In logical TRUE conditions, the circuit exhibits uneven responses because the INHIBIT gate, which requires the removal of only one DNA bond (X_1*), is kinetically more favorable to disassemble than the Disassembly AND gate that requires the simultaneous removal of two different DNA bonds. The successful implementation of the nanoparticle multiplexer shows that one can design and operate nanoparticle circuits on LNTs in a highly modular and controllable manner.

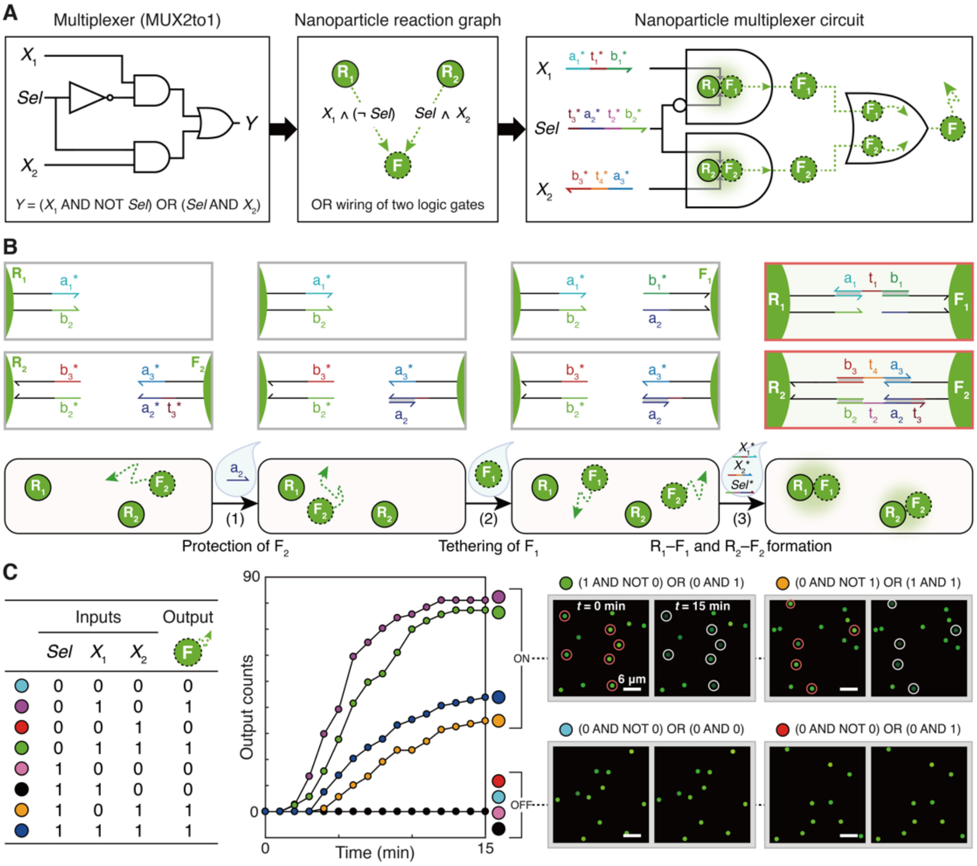

	Inputs			Output
	Sel	X_1	X_2	F
●	0	0	0	0
●	0	1	0	1
●	0	0	1	0
●	0	1	1	1
●	1	0	0	0
●	1	1	0	0
●	1	0	1	1
●	1	1	1	1

Fig. 5. A nanoparticle multiplexer circuit. (**A**) A multiplexer circuit (MUX2to1) implemented by a network of nanoparticles. The multiplexer is constructed by wiring a Disassembly INHIBIT gate (X_1 AND NOT *Sel*) and a Disassembly AND gate (*Sel* AND X_2) with OR logic. Four green nanoparticles (R_1, R_2, F_1, F_2) constitute the multiplexer circuit. (**B**) Modular construction of the nanoparticle multiplexer on a lipid bilayer. The circuit components could be loaded in a controlled and modular manner. To prevent unwanted spontaneous interaction between F_1 and F_2, F_2 was hybridized with the protector strand a_2 prior to loading F_1. (**C**) Measured performance of the multiplexer circuit. Truth table (left), kinetics analysis (middle), and dark-field snapshots (right). Domain-level illustration of the circuit operation is illustrated in fig. S18. Scale bar is 4 μm. DNA sequences and experimental conditions are listed in tables S2 and S3. Experiments were carried out at 25°C in 1× PBS buffer.

3.4. Conclusion

The uniqueness of LNTs lies in the following three merits. First, the computation is solely driven by SLB-tethered nanoparticles whose particle-by-particle interactions are programmable and readable *in situ*. A dynamic network of individual nanoparticles thus acts as a logic circuit. Second, information relay in the dynamic nanoparticle circuits does not require signal restoration or amplification because the cascading is exclusively driven by mobile floaters. In this context, floaters are “wires” carrying the information of upstream gates into downstream gates via their robust lateral diffusion (fig. S19). Third, spatial constraints are exploited to direct the information flow in dynamic-yet-confined nanoparticle networks. Complex digital logic operations can be implemented using a relatively small number of particle and ligand types with few design constraints, as reaction centers can be separated by immobile receptors. The demonstration of the multiplexer circuit exemplifies the beneficial role of spatial constraints in LNT platform. Through the integration with a lipid bilayer, nanoparticles exhibit new collective properties—digital principles—that are absent and cannot be realized in their static, solution-phase assemblies.

The scope of lipid bilayer-based nanoparticle computation can be expanded to advance current molecular computing technologies. First, solution-phase molecular circuits that generate single-stranded DNA as outputs (*7*, *8*, *13*, *14*) can be synergistically interfaced with LNTs because the released DNA molecules can be used as new inputs to operate the nanoparticle circuits. Through the additional layer of molecular circuitry in solution, different nanoparticle circuit modules on a lipid bilayer can communicate with each other. Second, particle modifications based on chemical ligands other than DNA can be introduced to implement nanoparticle circuits that process diverse chemical information (*37*). When nanoparticles are functionalized with new chemical ligands, the design constraints (that may arise from the crosstalk between different surface ligands) can be reduced because particle-by-particle interactions can be spatiotemporally controlled on a lipid bilayer. Third, integrations of lipid bilayers with DNA nanostructures (*38*) may provide a path toward the development of new molecular circuits. If DNA origami scaffolds that contain spatially localized DNA circuits are tethered to SLBs, one may be able to exploit a dynamic network of inter-origami interactions to implement more complex and practical molecular computation.

Despite such potentials, further scaling up the complexity of nanoparticle circuits on LNTs will be challenging because the input (molecules in solution) and output (state-switching floaters) are of different forms. Currently, this intrinsic difference limits the construction of arbitrarily large circuits. We predict that this challenge can be potentially addressed in two ways. First, harnessing new modes of nanoparticle reaction and ligand activation—such as communication (*3*, *4*), dynamic reconfiguration (*39*), and DNA walker (*40*)—may provide a much broader design space for circuit design. Second, increasing the number of different nanoparticle computing units per lipid bilayer "computing chip" will enhance the processing power because these units can operate as a complex circuit through network programming. This approach is similar to the way silicon-based computers have improved over the years: an increase in component density enhances their computing capacity. Exploiting the potential of parallelism, we will ultimately have each nanoparticle independently perform a computation on its own.

As spatial constraints such as localization and encapsulation enable the modular execution of molecular and synthetic biological circuits (*10*, *41*, *42*), tethering of nanoparticles to a lipid bilayer provides a systematic method to build complex nanoparticle circuits. LNT platform will play a pivotal role in constructing dynamic, “autonomous” nanosystems and devices, which will have broad impacts in the following areas. First, LNT platform can be applied to molecular diagnostics and smart sensors; the systems of individual nano-objects in the devices should be able to exploit internal computational algorithms to sense multiple stimuli and trigger the most appropriate responses. Second, if the nanoparticle circuits are introduced to living cell membranes (*43*), it might be possible to create a new type of nano–bio interfaces that are useful for cell-surface engineering and biological-inorganic hybrid systems. Lastly, information-processing nanoparticles on SLBs can be applied to reconstituting artificial cell–cell junctions and used as tools for studying membrane-associated phenomena in living cells. Unlike existing methods that rely on immutable materials such as patterned membranes (*34*), LNTs will allow networks of SLB-tethered nanostructures to algorithmically form clusters in response to signaling molecules released from the cells. Facilitating the nano- and cellular system to communicate with one another, such “active” SLB–cell junctions can also be employed to test how individual theranostic nanorobots navigate complex and dynamic environments.

3.5. Supporting Information

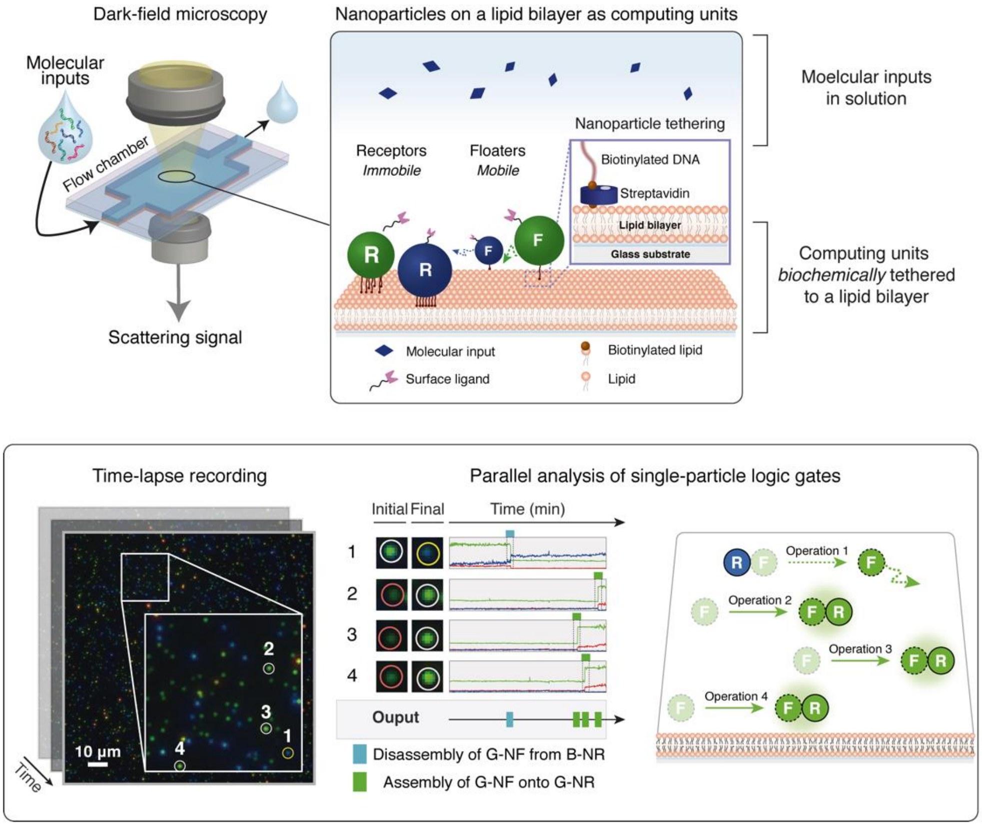

Figure S1. Conceptual illustrations of lipid nanotablet platform.

A lipid nanotablet (LNT) takes molecules as inputs and performs nanoparticle logic computation via nanoparticle networks tethered to its supported lipid bilayer, inducing dynamic assembly/disassembly reactions of nanoparticles as outputs. The plasmonic nanoparticles act as computing units and provide *in situ* optical readout as outputs that are readily readable and analyzable by dark-field microscopy (DFM). (**A**) Supported lipid bilayers as chemical circuit boards for nanoparticle computation. In LNT platform, the nanoparticle logic units are tethered to the lipid bilayer surface via strong interaction between biotinylated DNA linkers on the nanoparticle surfaces and streptavidins bound to biotinylated lipid molecules. On a lipid bilayer, receptor nanoparticles (R) are immobile due to a large number of surface DNA linkers that strongly interact with the lipid surface, and floater nanoparticles (F) are freely diffusible due to low linker density. Depending on the scattering signals of core nanoparticles, receptors are referred to as red nano-receptors (R-NRs), green nano-receptors (G-NRs), or blue nano-receptors (B-NRs). Similarly, floaters are referred to as red nano-floaters (R-NRs), green nano-floaters (G-NFs) or blue nano-floaters (B-NFs). Receptors and floaters serve as logic gates, processing the molecular information in solution using their programmable, stimuli-responsive surface ligands. Once nanoparticle logic gates are integrated on the lipid bilayer “chip”, solutions such as wash buffer and those containing nanoparticle gates or molecular inputs can be exchanged without perturbing the tethered particles. In addition, the dark-field imaging can be performed during the solution exchange *in situ*. (**B**) Parallel, single-particle analysis of nanoparticles by DFM. On LNT platform, multiple nanoparticle logic gates can be analyzed in parallel as long as each logic gate generates a spectrally distinct optical signal as an output. Several logic gates can be readily designed to generate distinct optical signals because plasmonic coupling-induced changes in a nanoparticle scattering signal depend on the combinations of receptor–floater pair involved in the interaction (*36*). A simple example of parallel, single-particle analysis on LNTs is illustrated. In this example, an Assembly logic gate is composed of a G-NR and a G-NF, and a Disassembly logic gate is composed of a B-NR and a G-NF. The two output signals of the two logic gates, an increase in green intensity of a G-NR (by association with a G-NF) and a decrease in the green intensity of a B-NR (by dissociation with a G-NF), are readily discernible. Thus, the two gates can be executed simultaneously.

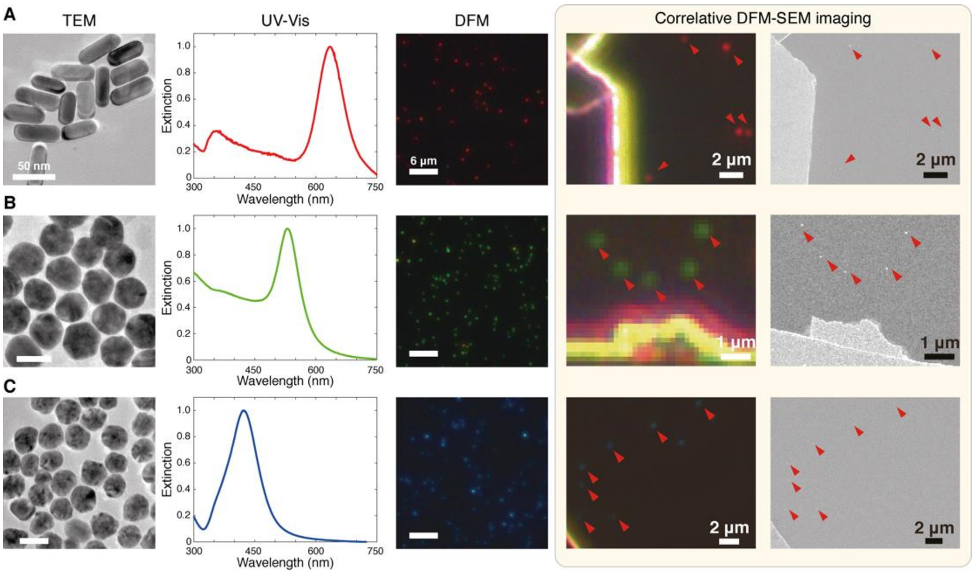

Figure S2. Characterization of nanoparticles

(**A**) Gold nanorods with silver shells (diameter = 22.2 ± 1.2 nm, length = 55.9 ± 2.9, aspect ratio = 2.5) that serve as core red nanoparticles for R-NRs and R-NFs. (**B**) Gold nanospheres (diameters = 50.0 ± 1.8 nm) used as core green particles for G-NRs and G-NFs. (**C**) Silver nanospheres with gold seeds (diameters = 54.8 ± 3.1 nm) that function as core blue particles for B-NRs and B-NFs. First column: transmission electron microscopy images. Second column: extinction spectra obtained by an ultraviolet–visible spectrophotometer. The three spectra were normalized to 1 OD. Third column: DFM images of nanoparticles tethered to a supported lipid bilayer. Fourth and fifth columns: Correlative DFM-SEM imaging for single-nanoparticle scattering signal analysis. Nanoparticles on a Cr-patterned glass substrate were first imaged by DFM, treated with Pt, and imaged in the same position by FE-SEM. As nanoparticles exhibit plasmonic coupling effect when the two nanoparticles are located in a close distance, we could determine whether a bright spot is from a single particle or an aggregation. The SEM images taken in the same positions (right) show that bright spots captured in the DFM images (left) are from single nanoparticles.

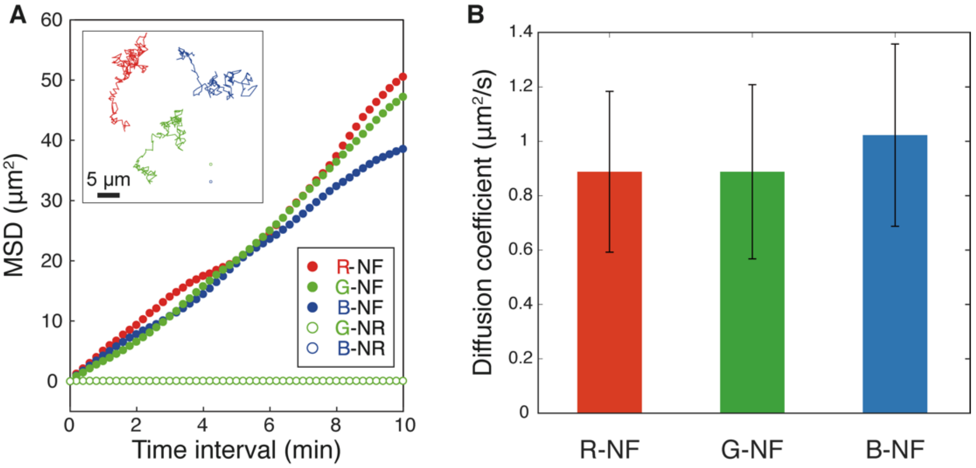

Figure S3. Diffusion of nanoparticles tethered to a supported lipid bilayer.

(**A**) Mean square displacement (MSD) versus time plots of the five representative diffusion trajectories (inset). The MSD plots of the three mobile floaters, R-NFs, G-NFs, and B-NFs, showed a linear relationship that confirmed their two-dimensional Brownian motions. The MSD plots of G-NRs and B-NRs confirmed their immobility. (**B**) Average diffusion coefficients of the diffusive R-NF (N_{tot} = 154), G-NF (N_{tot} = 194), and B-NFs (N_{tot} = 247). Error bars indicate standard deviations.

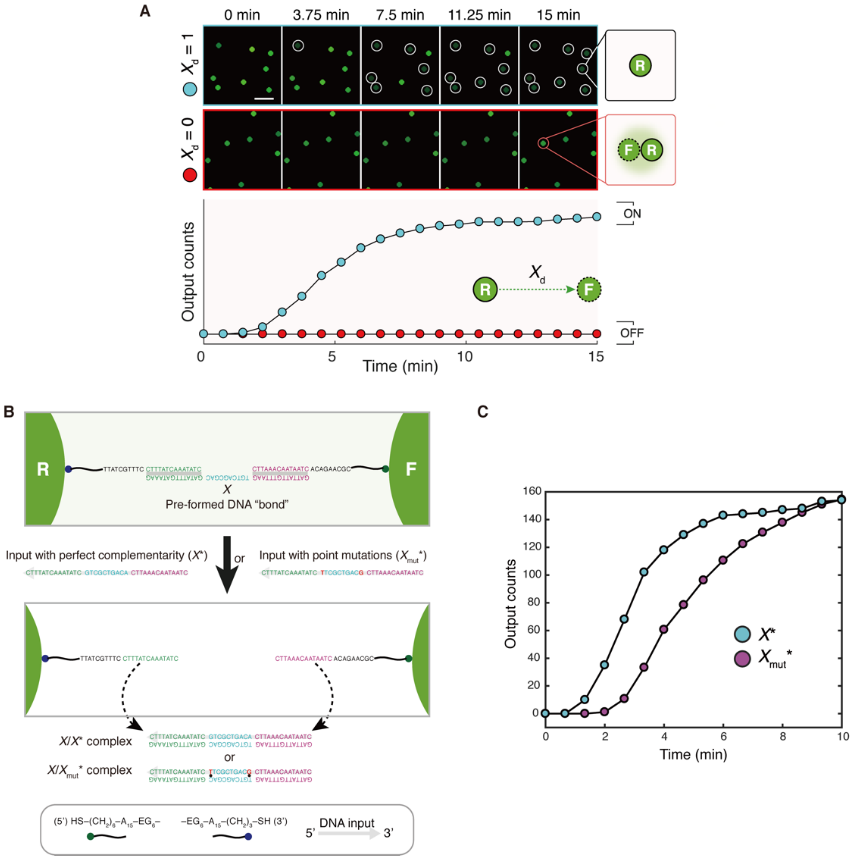

Figure S4. Design and implementation of a Disassembly YES gate.

(**A**) DNA-mediated disassembly reactions captured by DFM imaging. Inputs were added after pre-dimerization. G-NFs are released from G-NRs only when a disassembly input X_d (in Figure 1C) is present in solution. The disassembly events were cumulatively counted as outputs of the Disassembly YES gate. The time-versus-output plot indicates that the population of Disassembly YES gate switches into ON state in response to X_d. (**B**) Nucleotide-level illustrations of a Disassembly YES gate responding to a fully complementary input (X^*) and a mismatched input (X_{mut}^*). Two-point mutations at both ends of the toehold domain (A to G, G to T) and mismatched base pairings are highlighted. (**C**) Kinetics analysis. Fully complementary and mismatched inputs are shown in cyan and magenta, respectively. Due to the high concentration (500 nM) of input and long toehold domain, equilibrium is pushed toward disassembly even in the presence of base mismatches. As a result, responses under both conditions were saturated after sufficient operation time. However, the fully complementary input induced faster response of the disassembly gate than the mismatched input, which indicated that the system could potentially discriminate mismatched inputs under certain conditions. EG denotes an ethylene glycol unit. Asterisks denote complementarity.

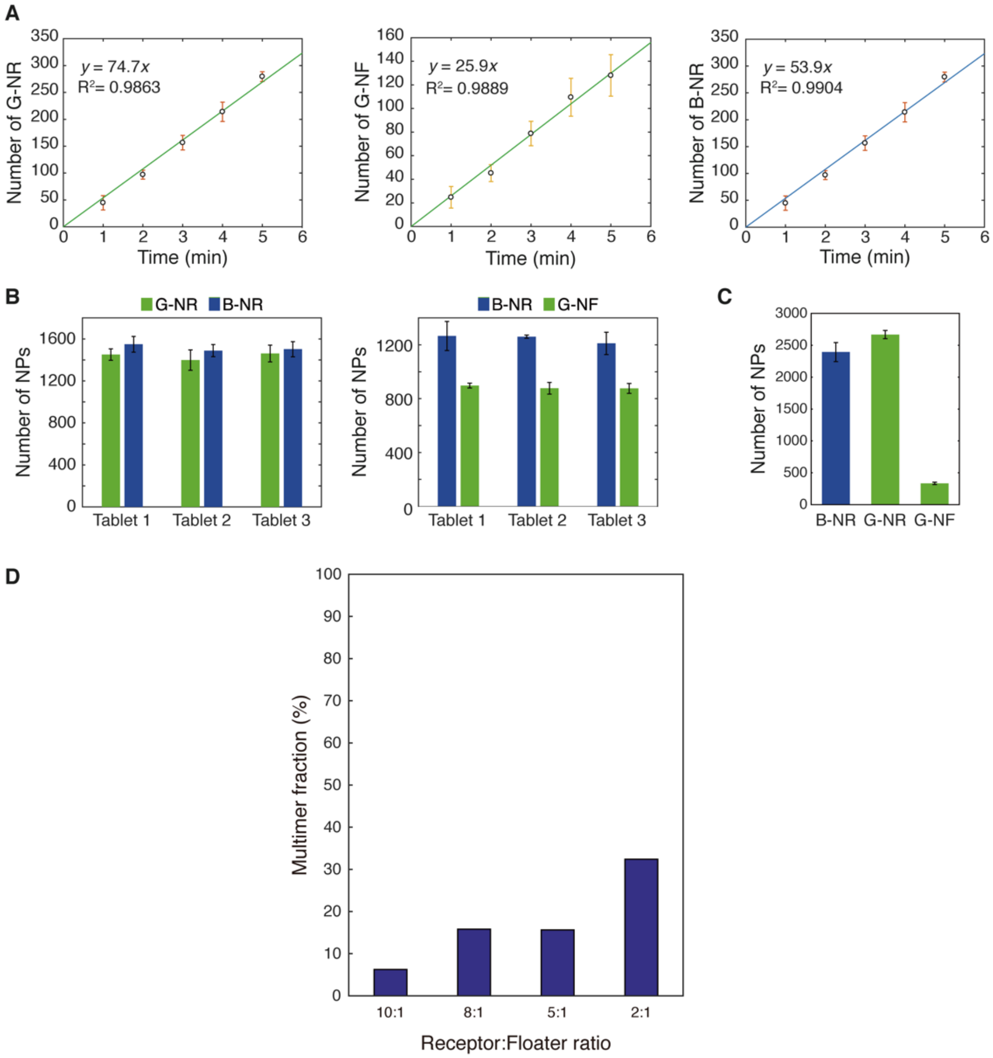

Figure S5. Tethering of nanoparticles to a supported lipid bilayer.

(**A**) The number of nanoparticles (NPs) tethered to a supported lipid bilayer versus incubation time plots. Tethering processes of 2.5 pM G-NR (left), 2.6 pM G-NF (center) and 2.2 pM B-NR (right) are described. The number of NPs at each time point was counted in an area of 90 × 90 μm^2 at four different positions. Error bars indicate standard deviations calculated based on the particle numbers obtained at the four positions. The plots showed that the number of tethered particles is linearly proportional to the time during which a lipid bilayer chambers is incubated with the solution containing biotinylated NPs ($R^2 > 0.98$). The plots also revealed that tethering of receptors is faster than tethering of floaters, as expected from the high linker density of the receptors. This linear relationship allowed accurate control of NP density on lipid bilayers. We also observed that the NPs loaded in the linear range were in better quality; floater particles were more mobile, and less aggregation of NPs was observed. We speculate that NPs could non-specifically bind to a lipid bilayer when incubation time is too long (beyond the linear range). (**B**) The number of tethered NPs in three replicate flow chambers (i.e. tablets). Tethering of G-NRs and B-NRs (left) and B-NRs and G-NFs (right) are described. For each tablet, the number of NPs was counted in an area of 90 × 90 μm^2 at four different positions after the tethering. Error bars indicate standard deviations calculated based on the particle numbers obtained from the four different positions. The tablet-to-tablet variability in particle numbers was negligible. (**C**) The number of three different NPs (B-NRs, G-NRs, and G-NFs) measured at four different positions in a flow chamber. Error bars indicate standard deviation calculated based on the number of NPs obtained from the four different positions. These results demonstrate that the tethering of NPs on a lipid nanotablet is controllable and robust across the large area of lipid bilayers, regardless of nanoparticle types and mobility. The typical population density used in this study was approximately 3,700 receptors and 300 floaters per 180 × 180 μm^2. This optimum density was chosen because (*i*) we wanted at least 100 binding or unbinding events to be observed less than 30 min and (*ii*) at a higher density signal overlaps complicated the image analysis. (**D**) Degree of multimer-forming reactions estimated by MATLAB-based simulation. Assembly reactions of SLB-tethered NPs were modeled and simulated using MATLAB. This computational approach was developed to estimate how a receptor/floater ratio affects the degree of multimer formation. In the model, a given number of receptors and floaters were randomly dispersed in an area of 128 × 128 μm^2 with the periodic boundary conditions. The total number of NPs in the area was set to be 1,800. Diffusion constants of floaters were assigned to have a normal distribution with mean 0.9 μm^2/s and standard deviation of 0.3 μm^2/s. This approximation is based on the experimental data on diffusion profiles of floaters shown in figure S3. We assumed that the diffusion of floaters is governed by a two-dimensional random walk, where the step size for each floater is $\sqrt{4Dt}$ with t = 5 ms. Positions of receptors were fixed. To run the simulation efficiently, floaters were set to diffuse on the grid points. Each grid point was separated by a diameter of particle cross section. The binding events between a receptor and a floater occur with the probability of 0.3 for each collision. In the simulation, “collision” is defined as an event that occurs when a coordinate of a floater on the grid overlaps with that of a receptor. For multimer formation processes, lower binding probabilities (0.18 for trimer formation and 0.09 for tetramer formation) were used because the addition of another floater to a receptor–floater dimer and a trimer is sterically less favored than the addition of a floater to a receptor (*47*). The scaling factor was introduced based on the geometrical constraints. The fraction of floaters that formed multimers (trimers or tetramers) in simulated assembly reactions for a given receptor/floater ratio was estimated using MATLAB-based simulation. Under 10:1, 8:1, 5:1, and 2:1 receptor/floater ratios, 6%, 15%, 15%, and 34% of floaters ended up forming multimers, respectively.

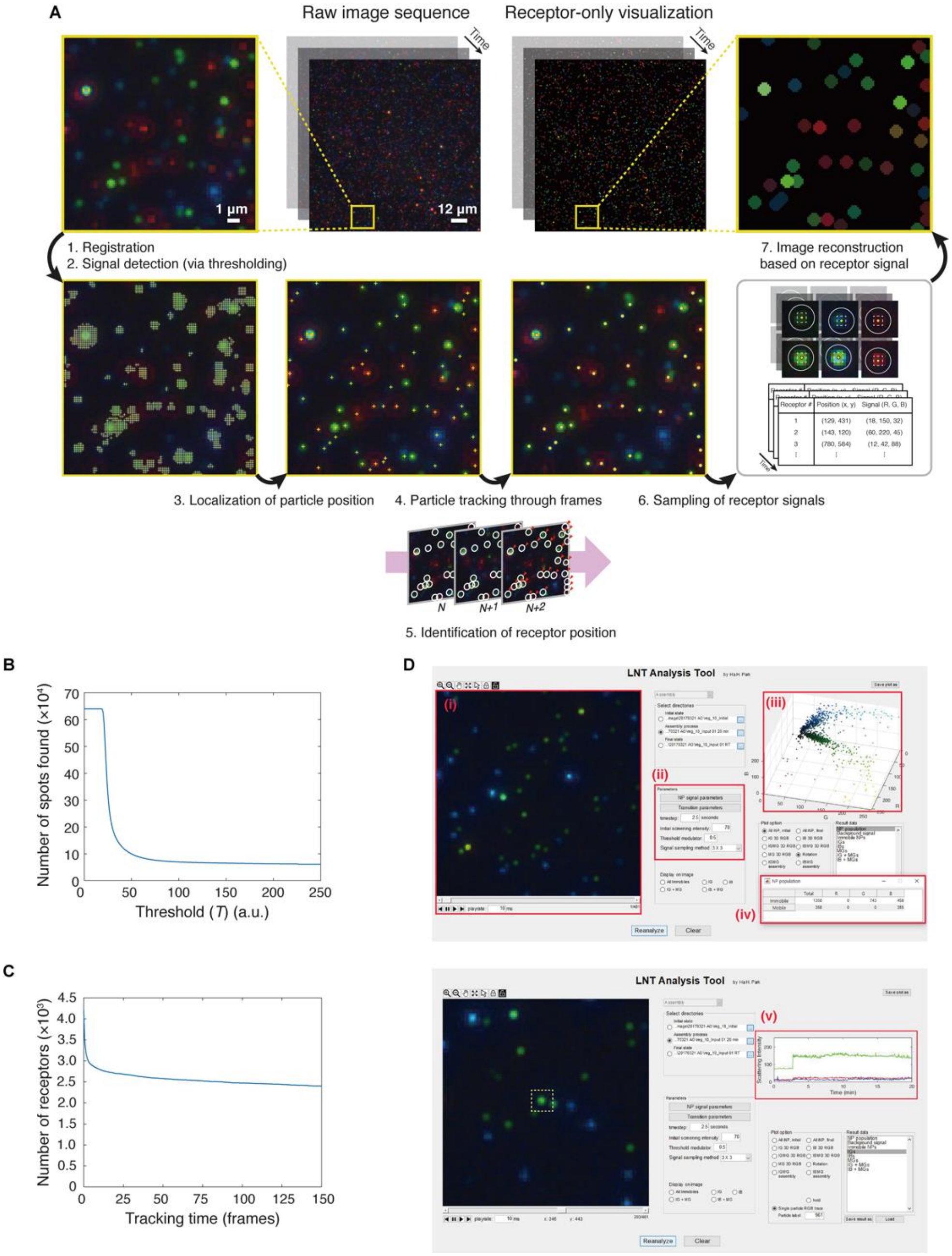

Figure S6. Image analysis pipeline.

(**A**) Single-particle tracking algorithm for the analysis of time-lapse DFM images. After image registration (step 1), pixels with signal intensities higher than a detection parameter are detected and marked with yellow crosses (step 2). The detection parameter (*d*) is specific to each dark-field movie because types and populations of nanoparticles on each tablet affect the background signal of the movie. In our analysis, d is defined as: $d = m_{background} + 0.5 \times \sigma_{background}$, where $m_{background}$ and $\sigma_{background}$ are average and standard deviation of the pixels whose gray scale intensities are below a chosen threshold T. The boundaries of the detected signals (pixels) are readily distinguishable. It was assumed that the segmented signals are from nanoparticles. Centers of the segmented signals are localized to provide the positions of the nanoparticles (step 3). The localized particles are marked with yellow crosses. Receptors are identified by comparing the localized positions through frames (step 4). Particles whose positions remained unchanged for entire imaging duration are identified as receptors and marked with yellow dots (step 5). For each receptor, a signal intensity is sampled and averaged from a 3 × 3 pixel window that is marked with a white dotted box. Visualizing only receptor signals in the dark background yields a "receptor-only" dark-field image sequence. (**B**) The number of detected signals plotted as a function of the threshold T. The presence of a plateau suggests that there is a condition over which the number of identified signals is insensitive to the threshold value T chosen for the analysis. (**C**) The number of receptors plotted as a function of the tracking frame. The presence of a plateau indicates that the number of identified receptors is insensitive to the particular tracking length chosen for the analysis. We chose 70 (a.u.) as a threshold T and 31 (frames) as a tracking length. Positions and signals of receptors in the raw dark-field image sequence movie correspond very well with those identified by the algorithm. The comparison also shows that the algorithms reliably differentiate receptors from floaters in the high-density setting. (**D**) MATLAB-based graphical user interface for analyzing nanoparticle logic gates on LNTs. This program has the following features: (i) a raw dark-field image sequence uploaded for the analysis, (ii) a control panel for analysis parameters (e.g., threshold, signal sampling method, and transition parameter), (iii) a visualization of detected receptor signals in three-dimensional (3D) space of a red-green-blue (RGB) intensity scatter plot (i.e. 3D signal profile), (iv) the number of receptors (R-NR, G-NR, and B-NR) and floaters (R-NF, G-NF, and B-NF) detected from the input image sequence, and (v) a time trace of a selected receptor signal (marked with a yellow dotted box).

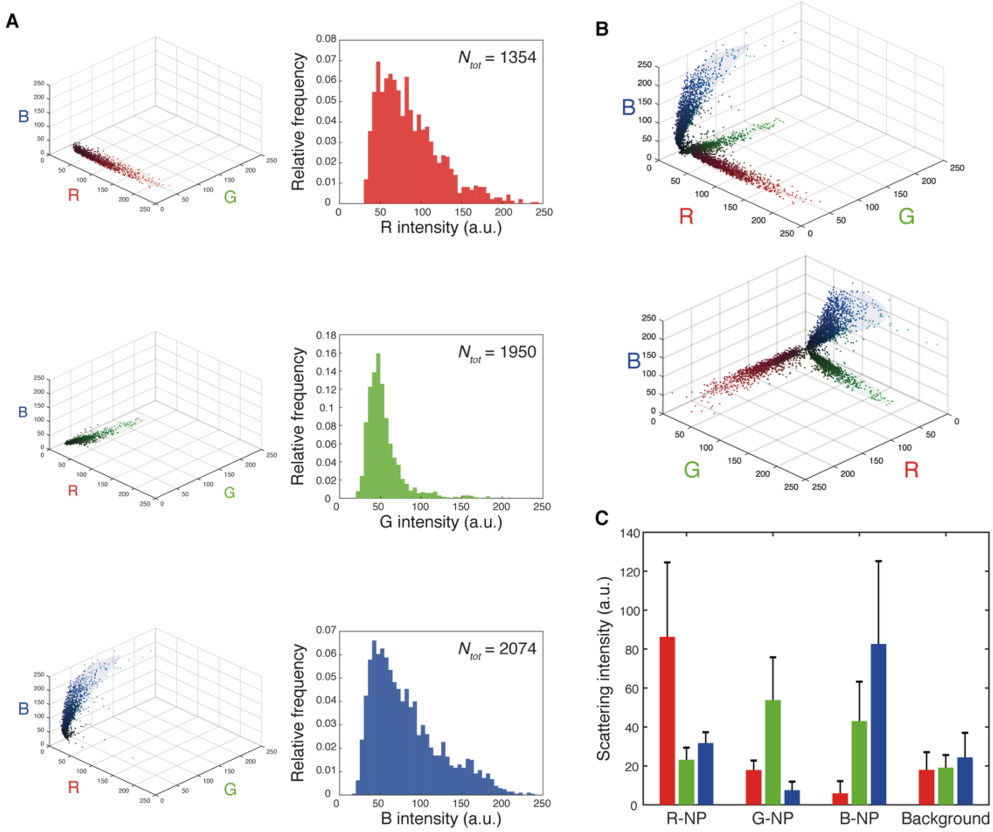

Figure S7. Scattering signal profiles of red, green, and blue nanoparticles.

(**A**) RGB intensity scatter plot of red nanoparticles (R-NP, upper), green nanoparticles (G-NP, middle), and blue nanoparticle (B-NP, lower) in 3D signal space. The background of each cluster is marked with its corresponding color to allow the clusters to be easily distinguishable from each other. (**B**) RGB scattering signals from R-NPs, G-NPs, and B-NPs are visualized together in the 3D signal space. The visualization shows three signal clusters with minimal overlap. This analysis shows that the scattering signals from the red, green, and blue nanoparticles are readily distinguishable from each other. **(C**) Average red, green, and blue scattering intensities of the nanoparticles and background signals are represented with red, green, and blue bars. Error bars indicate standard deviations. The signal profiles of the three core nanoparticles were obtained by the image analysis algorithm (described in figure S6) and used in identifying and classifying logic-gated nanoparticle reactions.

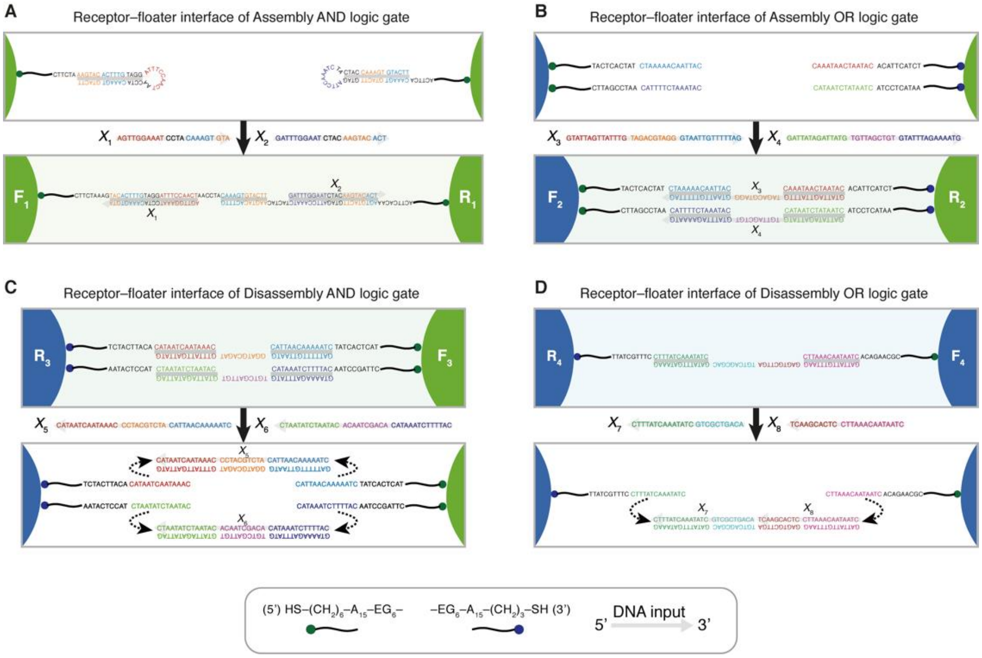

Fig. S8. Nucleotide-level schematics of two-input nanoparticle logic gates.
(**A**) Two-input Assembly AND gate. (**B**) Two-input Assembly OR gate. (**C**) Two-input Disassembly AND gate. (**D**) Two-input Disassembly OR gate. The sequence-level illustrations show how the gates respond to molecular inputs. EG denotes an ethylene glycol unit.

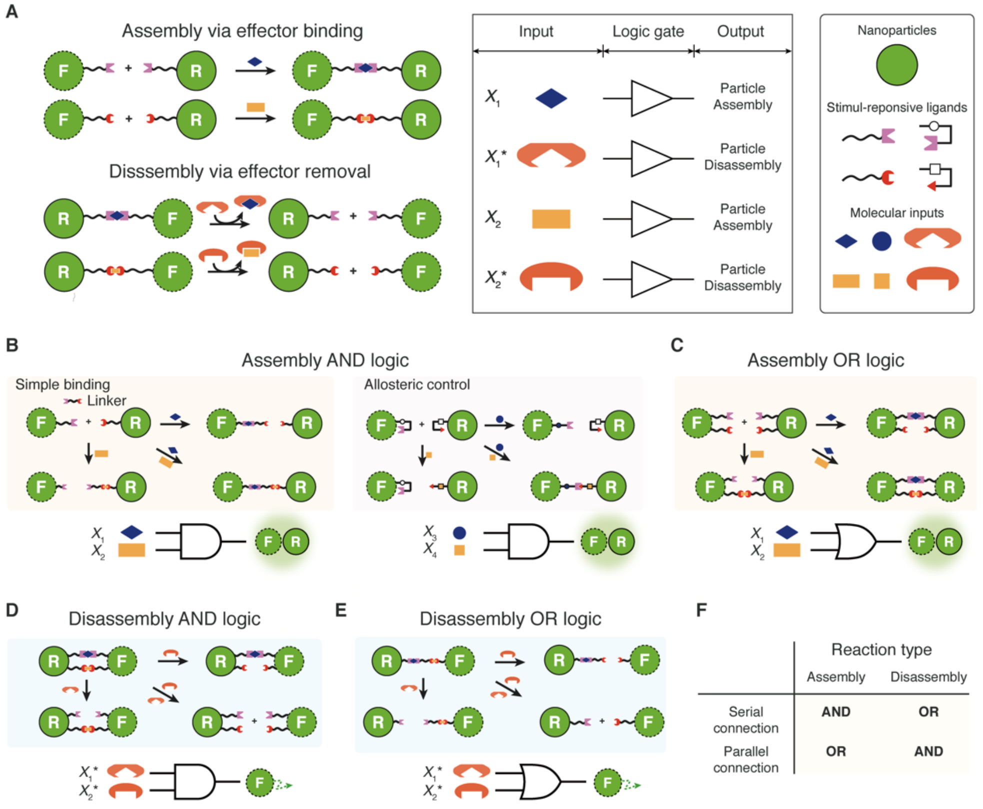

Figure S9. Design principles for nanoparticle logic gates.

(**A**) Graphical summary of the generalizable concept. Illustration of effector-mediated nanoparticle Assembly/Disassembly YES gates (left) and truth table for the concept (right) are provided. Selective effector-ligand pair and effector-chelator pair are required for construction of Assembly/Disassembly logic gates. To build a logic gate using two nanoparticles, "bonding" interactions in the receptor–floater interface need to be programmed in such a way that the bonds are formed (via assembly) or cleaved (via disassembly) only if two molecular inputs satisfy AND or OR logic. (**B**) Two-input Assembly AND gate. (**C**) Two-input Assembly OR gate. Assembly reactions are controlled by AND logic when the bond-forming interaction require the *serial* activation by the two inputs and by OR logic when the bond-forming interaction is controlled in *parallel*. (**D**) Two-input Disassembly AND gate. (**E**) Two-input Disassembly OR gate. Similarly, Disassembly reactions are modulated by AND logic via parallel disconnection paradigm and by OR logic via serial disconnection design. (**F**) Table summary. These illustrations describe the generalized concept of the interface programming. In this study, we used sequence recognition and strand displacement of DNA as the mechanisms to implement the logic. Specifically, we used single-stranded DNA molecules as effectors, thiolated oligonucleotides as ligands, and a strand displacement as chelation mechanism. We foresee that this design rules can be potentially applied to other ligand systems and core nanostructures.

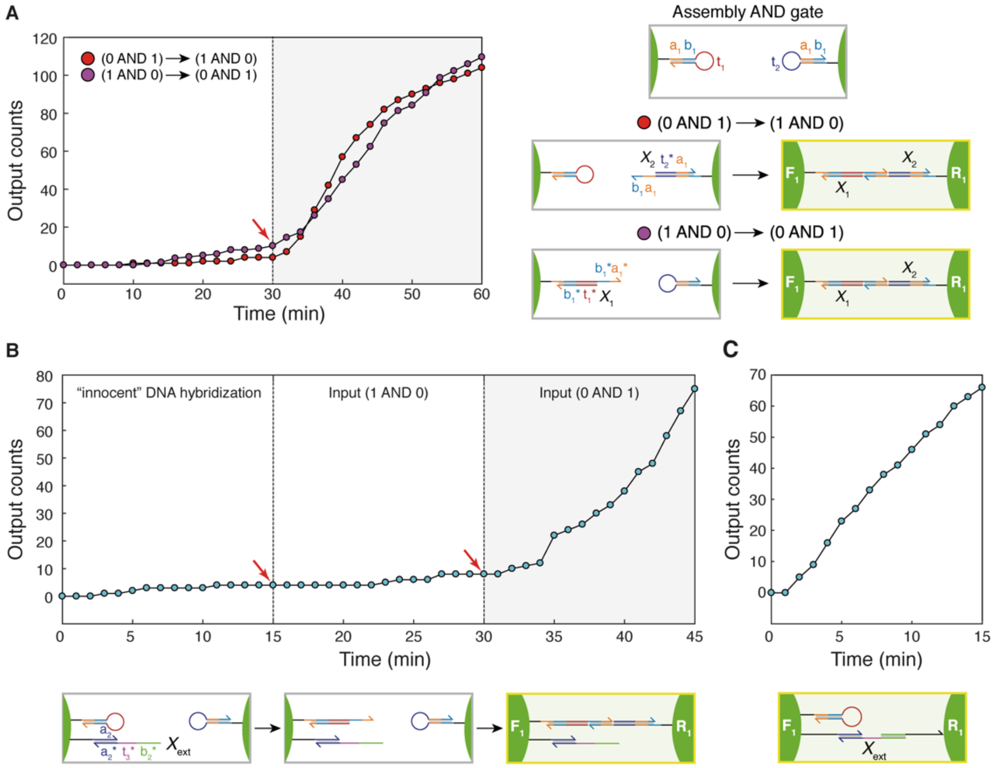

Figure S10. Modularity of a hairpin-based two-input Assembly AND gate.
(**A**) Sequential activation of the two-input Assembly AND gate (described in Figure 2A and figure S8A). The responses of the Assembly AND gate to sequentially introduced inputs (Red dots: X_2 addition followed by X_1 addition. Magenta dots: X_1 addition followed by X_2 addition). The results show that two hybridization events are all required to induce assembly reactions between R_1 and F_1. (**B**) Operation of the Assembly AND gate after hybridization by an "innocent" DNA input X_{ext} that interacts with a non-hairpin ligand on F_1. The results show that the hairpin-based assembly is insensitive to other hybridization events on the same particle. (**C**) Assembly by the DNA input X_{ext}. The assembly by the simple hybridization (as in Assembly YES gate) is insensitive to the presence of hairpin ligands on the same particle. In addition to the time-versus-output plots, domain-

level illustrations are provided. DNA sequences and experimental conditions are listed in tables S2 and S3.

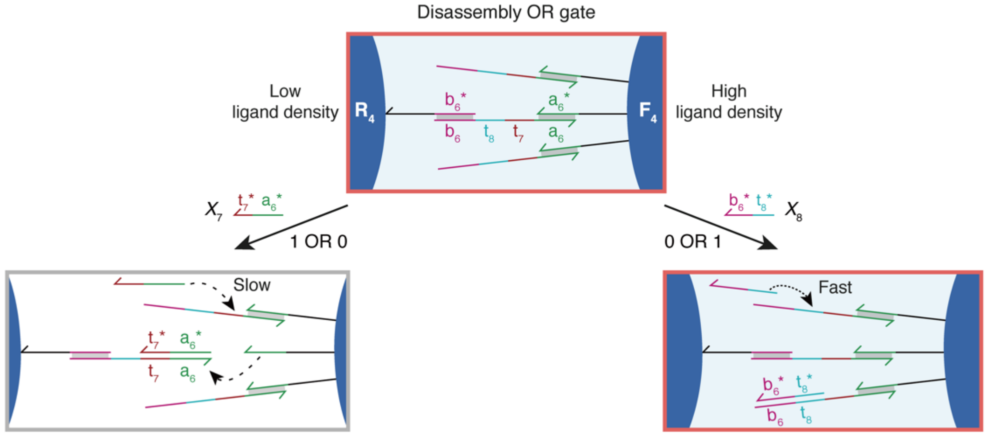

Input molecules (X_7) more easily participate in strand displacements that lead to particle disassembly

Input molecules (X_8) are more easily captured by the unhybridized domains (b_6-t_8-t_7) in R–F interface

Figure S11. Uneven responses of a two-input Disassembly OR gate.
We speculate that the higher response rate under 1 OR 0 condition than the response rate under 0 OR 1 condition can be attributable to the higher density of surface ligands in F_4 than in R_4. Due to its higher ligand density, F_4 exposes more single-stranded domains (b_6-t_8-t_7) than R_4 after pre-dimerization. The exposed strands can interact with incoming input strands. In 0 OR 1 condition, interactions between the input X_8 (b_6*-t_8*) and the exposed bonds are more effective compared with those between the input X_7 (a_6*-t_7*) and the bonds in 1 OR 0 condition, mainly because the recognizable sequence is longer and more accessible for the former interaction. As a result, the input X_8 is more easily trapped by the exposed strands without leading to effective strand displacements that induce particle disassembly. This interaction is an example of undesirable interactions that occur within particle–particle interfaces. R_4, F_4, X_7, and X_8 are from Figure 3D.

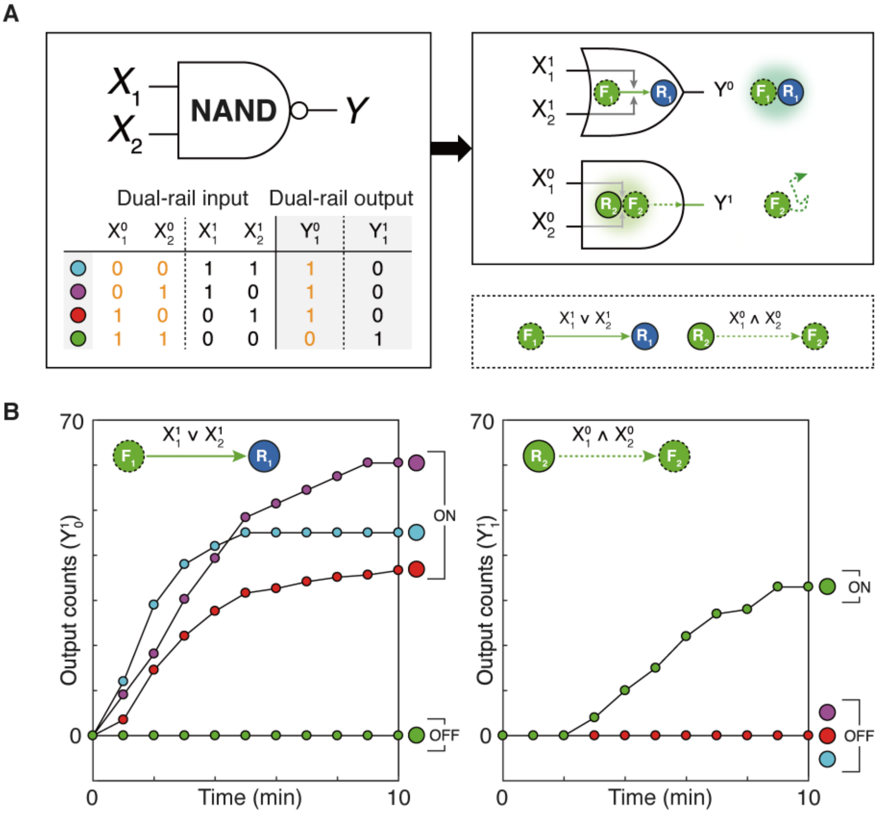

Figure S12. A dual-rail NAND gate.

(**A**) A two-input dual-rail NAND gate. Dual-rail inputs of X_i are represented as X_i^0 and X_i^1 (which denote logic FALSE and TRUE, respectively). Outputs were denoted by the same rule. A two-input Assembly OR gate (X_1^1 OR X_2^1) and a two-input Disassembly AND gate (X_1^0 AND X_2^0) are implemented in parallel to process dual-rail NAND logic. (**B**) Kinetics analysis. The two gates generate correct logic outputs without interfering with each other, providing ON/OFF levels over 37-fold (Y^0, two-input Assembly OR) and 33-fold (Y^1, two-input Disassembly AND). This result demonstrates the modularity of nanoparticle logic gates. DNA sequences and experimental conditions are listed in tables S2 and S3.

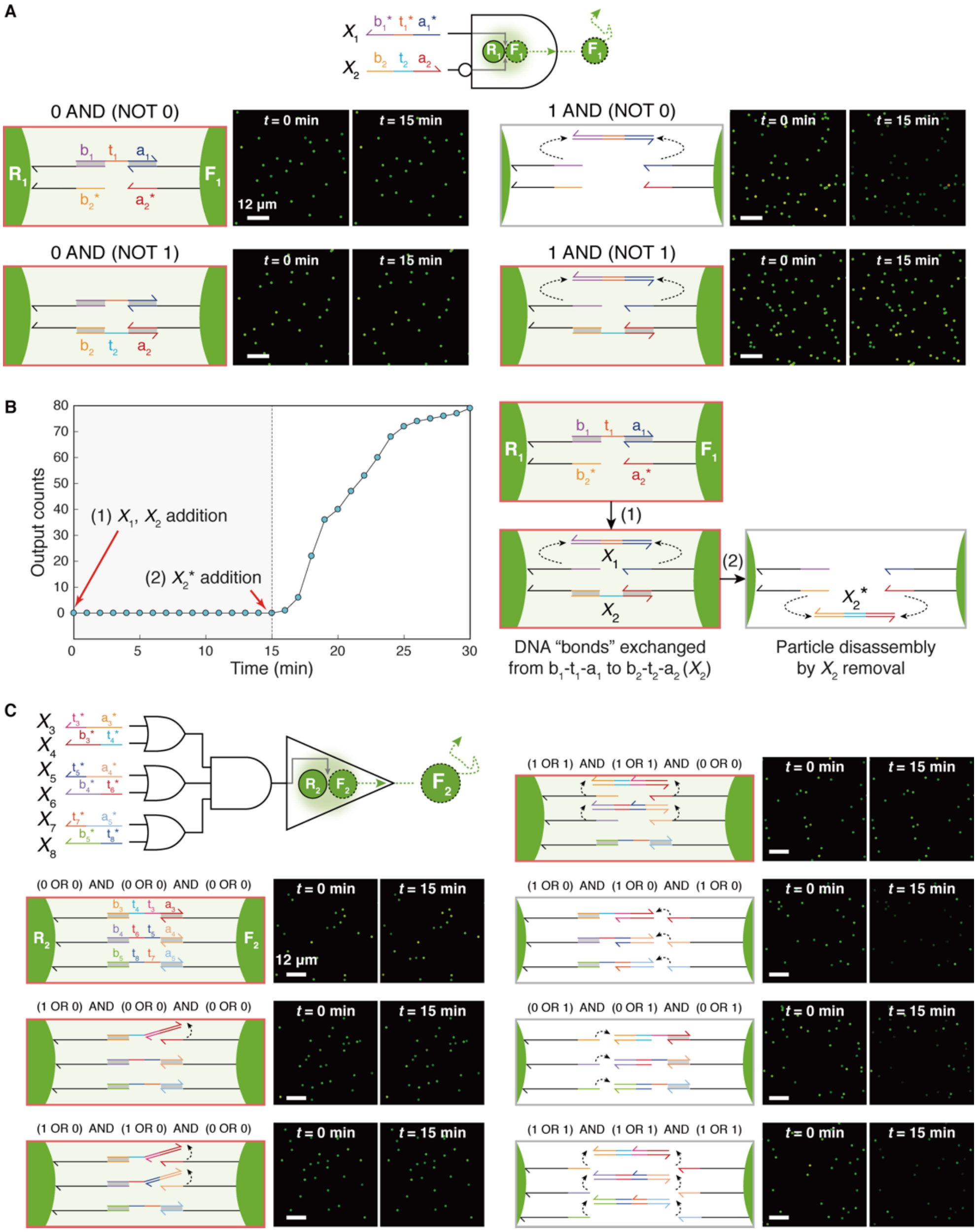

Fig. S13. Design and implementation of a Disassembly INHIBIT gate and a six-input Disassembly gates.

(**A**) Domain-level illustration (left) and reconstructed dark-field images (right) of a two-input Disassembly INHIBIT gate that evaluates X_1 AND (NOT X_2) logic. The reconstructed images provide only receptor signals. The disassembly reactions were observed only in the logical 1 AND (NOT 0) condition. (**B**) Characterization of strand displacement reactions in the Disassembly INHIBIT gate. According to the design, the DNA bond at an R_1–F_1 interface should change from b_1-t_1-a_1 to b_2-t_2-a_2 (X_2) upon the addition of the two inputs X_1 and X_2. If the bond exchange is effective at the receptor–floater interface, the disassembly reactions should occur upon the subsequent addition of X_2*. The time-versus-output plot shows that the INHIBIT gate operates as designed. DNA sequences and experimental conditions are listed in tables S2 and S3. See also movie S8. (**C**) Domain-level illustrations (left) and reconstructed dark-field images of the six-input Disassembly gate that processes (X_3 OR X_4) AND (X_5 OR X_6) AND (X_7 OR X_8) logic. DNA sequences and experimental conditions are listed in tables S2 and S3. See also movie S9.

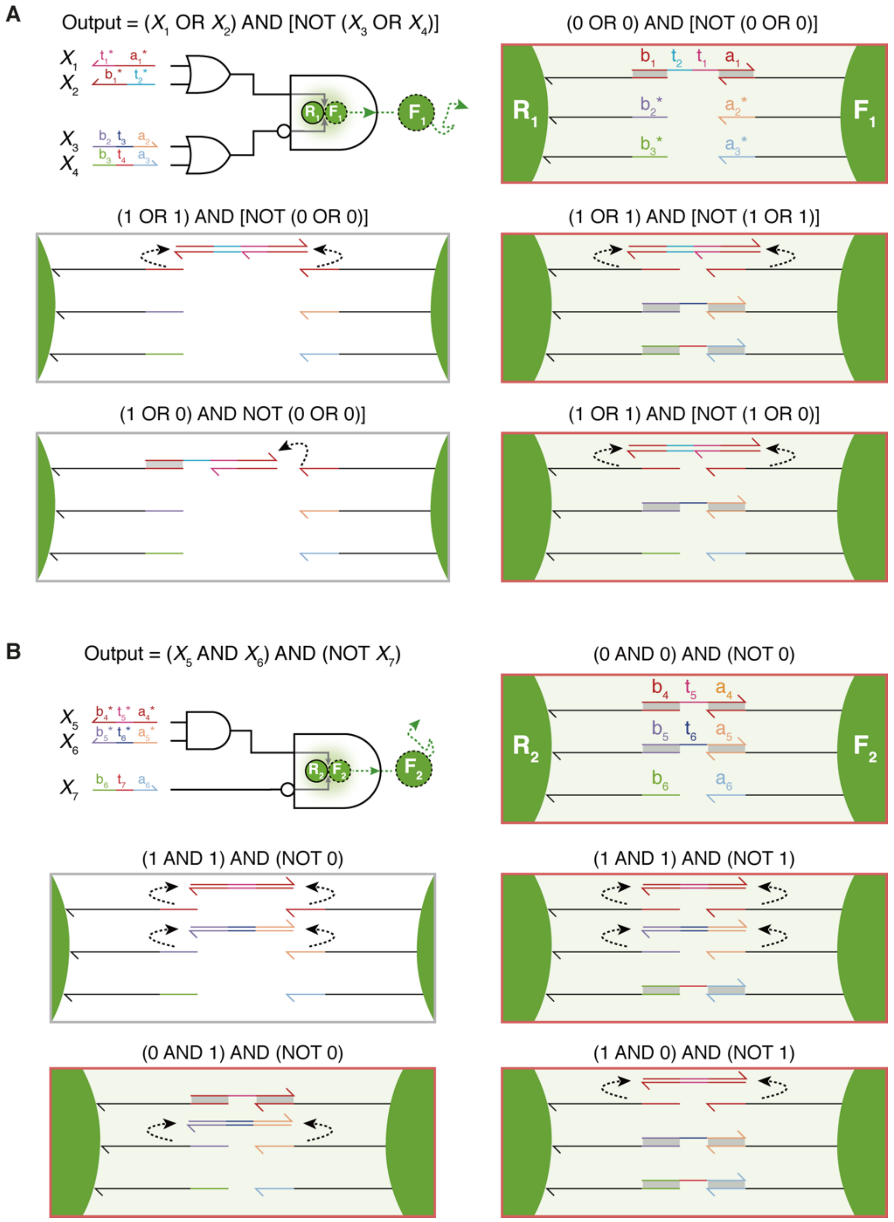

Figure S14. Complex multi-input Disassembly gates.

The approaches used to realize the INHIBIT logic and fan-in were combined to design Disassembly gates with more complex logic expressions. (**A**) A four-input Disassembly gate that processes (X_1 OR X_2) AND [NOT (X_3 OR X_4)] logic expression. In this design, either X_1 or X_2 can cleave a DNA bond (in a pre-formed R_1–F_1 dimer) and either X_3 or X_4 can form a bond within the dimer. In order for the dimer to disassemble, bond cleavage reactions should proceed in the absence of X_3 and X_4. (**B**) A three-input Disassembly gate that processes (X_5 AND X_6) AND (NOT X_7) logic. In order for the disassembly reaction to occur, X_5 and X_6 are required to remove the two different DNA bonds without additional bond formations by X_7.

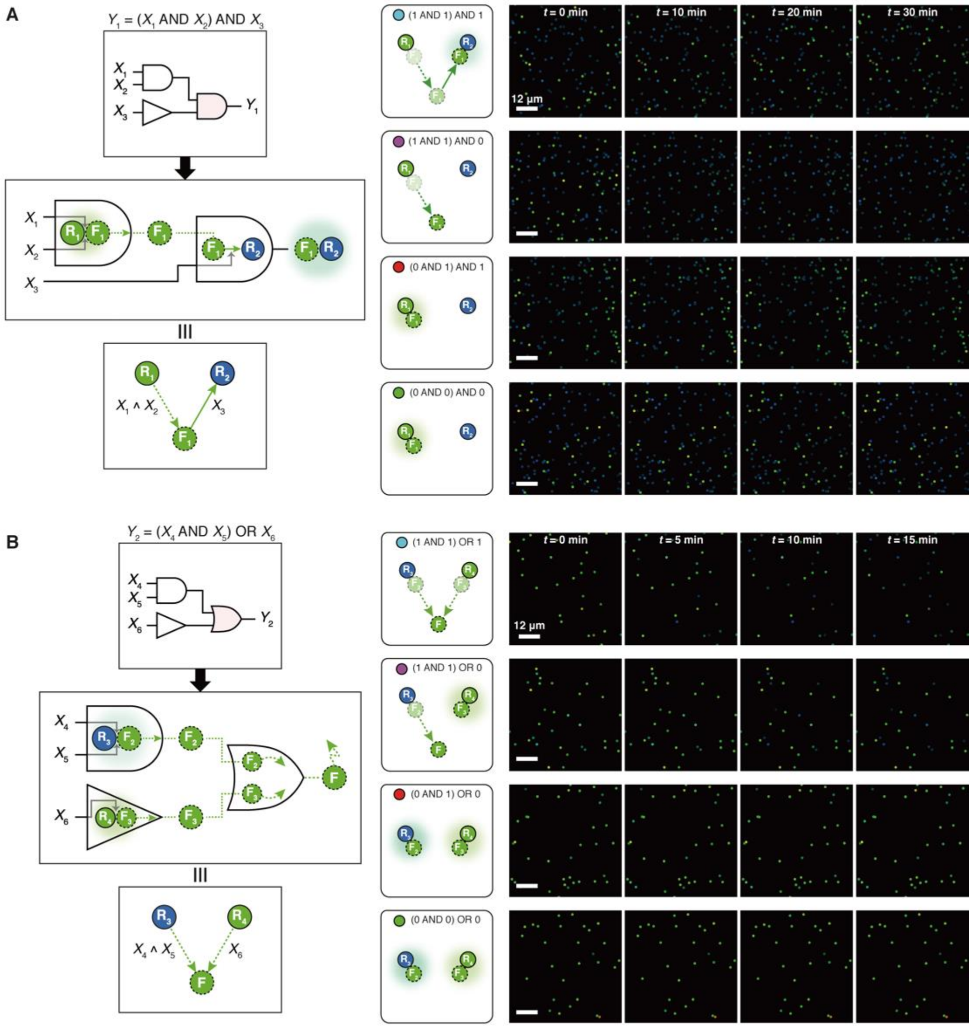

Figure S15. Dark-field snapshots of two-layer AND-AND and AND-OR cascade circuits.

(**A**) Two-layer AND-AND cascade circuit. The release of G-NFs (F_1) from G-NRs (R_1) is controlled by AND logic (X_1 AND X_2). The released F_1 can bind to R_2 only when the assembly input X_3 is present. The final circuit output is controlled by the three-input logic expression (X_1 AND X_2) AND X_3. In the first condition (1 AND 1) AND 1, the green intensity decreases in R_1 and increases in R_2, showing the successful cascading by the G-NFs (F_1). In the second condition (1 AND 1) AND 0, only the decrease in green intensity is observed. The lack of signal increase indicates that the released floaters (F_1) do not bind to other receptors. The bottom two conditions show no visible responses. (**B**) Two-layer AND-OR cascade circuit. The release of G-NFs (F_2) from B-NRs (R_3) is controlled by AND logic (X_4 AND X_5), and the release of different G-NFs (F_3) from G-NRs (R_4) is controlled by YES logic (X_6). The final circuit output is controlled by the three-input logic expression (X_4 AND X_5) OR X_6. In the first condition (1 AND 1) OR 1, the green intensity decrease from both R_3 and R_4, showing the successful release of the G-NFs from each receptor. In the second condition (1 AND 1) OR 0, the decrease in green intensity is only observed in B-NRs. This result indicates the dissociation of R_3–F_2 pairs are controlled by the AND logic operation. The bottom two conditions show no visible responses.

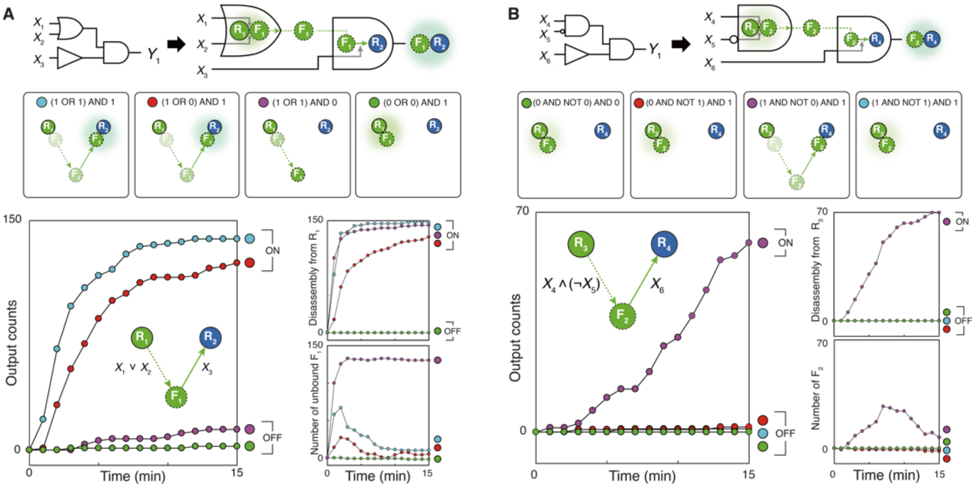

Fig. S16. Design and implementation of two-layer OR-AND and INHIBIT-AND cascade circuits.

(**A**) Two-layer OR-AND cascade circuit. The network-level AND wiring scheme is applied to construct a nanoparticle circuit that performs (X_1 OR X_2) AND X_3 logic operations. The circuit generates correct outputs that correspond to its logic, providing an ON/OFF level over 11-fold. The upstream Disassembly gate exhibited an ON/OFF level over 128-fold. As in the AND-AND cascade circuit shown in Fig. 4B, the population dynamics of G-NFs (F_1) was estimated in the circuit. The analysis showed that the G-NFs released from G-NRs (R_1) are bound to B-NRs (R_2) only when the input X_3 required for the assembly reaction is present. (**B**) Two-layer INHIBIT-AND cascade circuit. Disassembly reactions between G-NRs (R_3) and G-NFs (F_2) are controlled by (X_4 AND NOT X_5) logic, and the subsequent assembly reactions of F_2 with B-NRs (R_4) are mediated by input X_6. Generation of F_2-R_4 dimers is thus controlled by (X_4 AND NOT X_5) AND X_6 logic expression. The circuit carried out logic operations as designed, resulting in an ON/OFF level over 37-fold. The upstream INHIBIT gate provided an ON/OFF level over 70-fold. These results indicate that the released F_2 are bound to B-NRs only in the presence of input X_6. DNA sequences and experimental conditions are listed in tables S2 and S3.

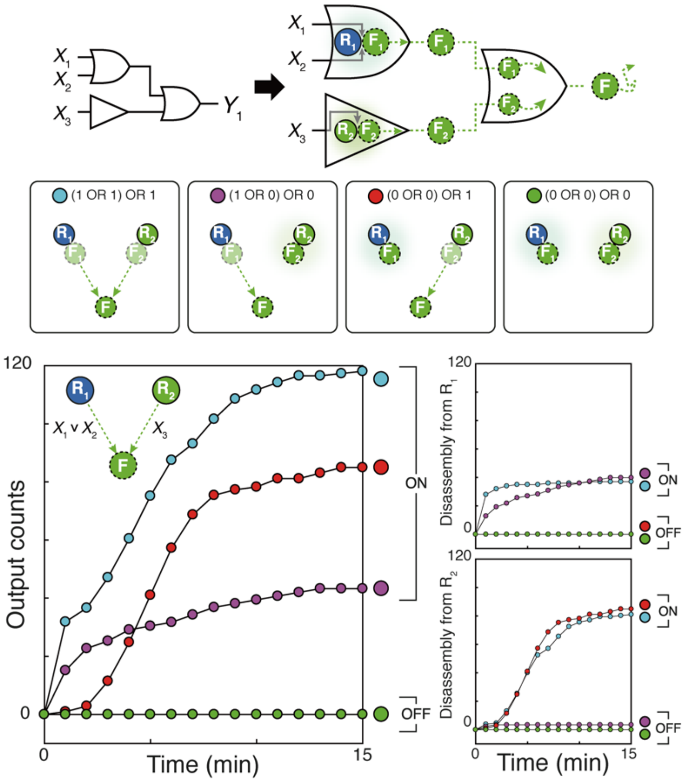

Fig. S17. Design and implementation of a two-layer OR-OR cascade circuit. The network-level OR wiring scheme is applied to construct a nanoparticle circuit that performs (X_1 OR X_2) OR X_3 logic operations. The circuit performs the computation as designed, resulting in an ON/OFF level over 43-fold. The upstream Disassembly OR gate and YES gate provided ON/OFF levels over 37-fold and 24-fold, respectively. DNA sequences and experimental conditions are listed in tables S2 and S3.

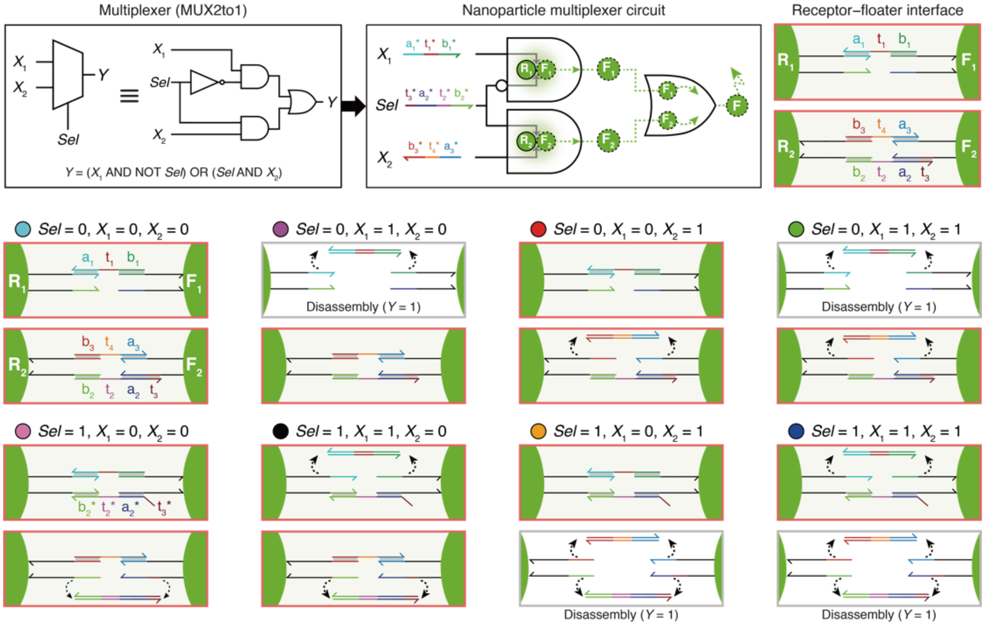

Fig. S18. Design and implementation of a nanoparticle multiplexer circuit. A multiplexer circuit was constructed by wiring a two-input Disassembly INHIBIT gate (R_1–F_1) and a two-input Disassembly AND gate (R_2–F_2) with OR logic. The circuit takes three inputs X_1, *Sel*, and X_2 and releases G-NFs as outputs. The nanoparticle surface ligands were designed in a way that two different receptor–floater pairs could simultaneously process the Selector (*Sel*) strands. In this design, spontaneous interactions between R_1 and R_2, as well as those between F_1 and F_2 could occur. However, these undesirable interactions were prevented by loading the nanoparticle circuit components in a specific order and by introducing the protection strand a_2. Domain-level illustration of the circuit operations is provided. DNA sequences and experimental conditions are listed in tables S2 and S3. See also movie S13.

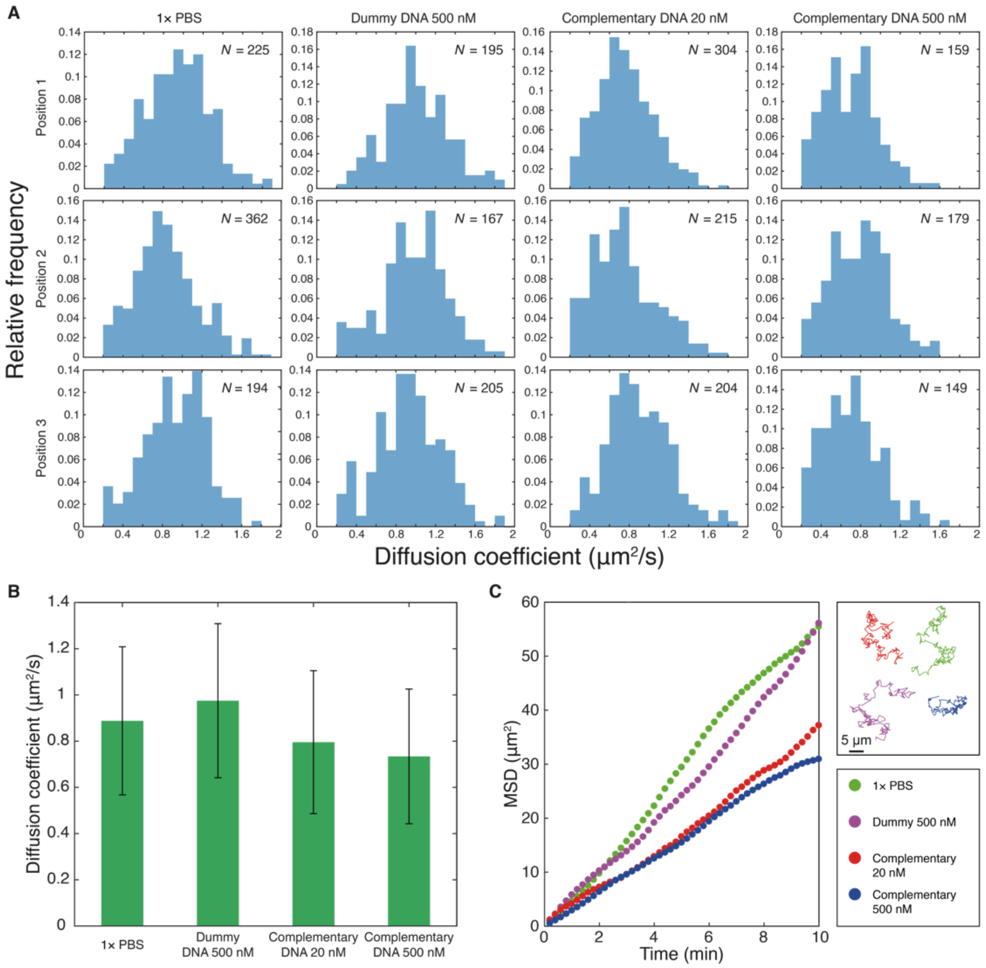

Fig. S19. Effect of DNA concentration on floater diffusion.

Diffusions of G-NFs were analyzed in various contexts, such as in 1× PBS buffer, with a high concentration (500 nM) of "dummy" DNA, with a low concentration (20 nM) of complementary DNA inputs, and with a high concentration (500 nM) of complementary DNA inputs. There was no complementarity between the surface ligands of the G-NFs and the dummy DNA (5'- GTTTAAGATTTATG GTTAAGCGTA GATTAAGTATTAAG -3'). The G-NFs used in the Assembly YES gate were used for analysis. In each solution, the diffusions of the floater were analyzed in three different positions. (**A**) Histograms of diffusion coefficients of the G-NFs under each condition. (**B**) Diffusion coefficient of the G-NFs. Error bars indicate standard deviation of the diffusion coefficients in each condition. (**C**) MSD versus time plots of the four representative diffusion trajectories. The analysis showed that the overall diffusive behaviors of G-NFs are robust to the chemical environments of the solution.

Table S1. Response rates (%) of four two-input logic gates.

Logic Circuit	Input condition			
	00	01	10	11
Two-input Assembly AND gate	2.80	7.78	17.74	84.31
Two-input Assembly OR gate	0.817	76.90	71.66	79.22
Two-input Disassembly AND gate	0	0.90	0	83.46
Two-input Disassembly OR gate	0	42.35	74.24	79.00

Table S2. DNA sequences of thiolated DNA strands used for functionalizing nanoparticles. *r*: a surface density of a thiolated DNA strand. Spacer for linker and ligand with 5’ thiol group: 5’- A_{15}–EG_6 -3’. Spacer for linker and ligand with 3’ thiol group: 5’- EG_6–A_{15} -3’.

Figure 1

Logic Circuit	NP	Ligand		Linker	
		Sequence	r (%)	Sequence	*r* (%)
Single-input Assembly YES gate	R (G-NR)	5’-CTATAAACTATTTC CTTTGCTATT–Spacer–SH -3’	65	5’- biotin–CTCTCTGCCTCGTTC AGACAAAACTCATCCTACT–Spacer–SH -3’	35
	F (G-NF)	5’-HS–Spacer–CGCAAAGACA CTAATAACAAATTC -3’	99.5	5’-HS–Spacer–TTACTACACTG TCACTGATCATCGCATGCTAT AC–biotin -3’	0.5

Single-input Disassembly YES gate	R (G-NR)	5’-CTATAAACTATTTC CTTTGCTATT–Spacer–SH -3’	65	5’-biotin–CTCTCTGCCTCGTT CAGACAAAACTCATCCTACT –Spacer–SH -3’	35
	F (G-NF)	5’-HS–Spacer– CGCAAAGACA CTAATAACAAATTC -3’	99.5	5’-HS–Spacer–TTACTACACT GTCACTGATCATCGCATGCT ATAC–biotin -3’	0.5

Figure 2

Logic Circuit	NP	Ligand		Linker	
		Sequence	*r* (%)	Sequence	*r* (%)
Two-input Assembly AND gate	R_1 (G-NR)	5’-HS–Spacer–ACTTCACAA AGTGTACTTGTAGATTC CAAATCTACTACAAGTAC ACT TTG -3’	65	5’-HS–Spacer–TTACTACACT GTCACTGATCATCGCATGCT ATAC–biotin -3’	35
	F_1 (G-NF)	5’-HS–Spacer–CTTCTAAAG TACACTTTGTAGGATTTC CAACTAACCTACAAAGT GTA CTT -3’	65	5’-HS–Spacer–TTACTACACT GTCACTGATCATCGCATGCT ATAC–biotin -3’	0.5
		5’-HS–Spacer–TTACTACA CTGTCACTGATCATCGCA TGCTATAC -3’	34.5		
Two-input Assembly OR gate	R_2 (G-NR)	5’-CAAATAACTAATAC ACATTCATCT–Spacer–SH -3’	32.5	5’-biotin–CTCTCTGCCTCGTT CAGACAAAACTCATCCTAC T–Spacer–SH -3’	35
		5’-CATAATCTATAATC ATCCTCATAA–Spacer–SH -3’	32.5		
	F_2 (B-NF)	5’-HS–Spacer– TACTCACTAT CTAAAAACAATTAC -3’	49.75	5’-HS–Spacer–TTACTACACT GTCACTGATCATCGCATGCT ATAC–biotin -3’	0.5
		5’-HS–Spacer– CTTAGCCTAA CATTTTCTAAATAC -3’	49.75		
Two-input DisassemblyAND gate	R_3 (B-NR)	5’-CAAATAACTAATAC ACATTCATCT–Spacer–SH -3’	25	5’-biotin–CTCTCTGCCTCGTT CAGACAAAACTCATCCTAC T–Spacer–SH -3’	50
		5’-CATAATCTATAATC ATCCTCATAA–Spacer–SH -3’	25		
	F_3 (G-NF)	5’-HS–Spacer– TACTCACTAT CTAAAAACAATTAC -3’	49.75	5’-HS–Spacer–TTACTACACT GTCACTGATCATCGCATGCT ATAC–biotin -3’	0.5
		5’-HS–Spacer– CTTAGCCTAA CATTTTCTAAATAC -3’	49.75		

Two-input Disassembly OR gate	R_4 (B-NR)	5'-CTATAAACTATTTC CTTTGCTATT–Spacer–SH -3'	50	5'-biotin–CTCTCTGCCTCGTT CAGACAAAACTCATCCTAC T–Spacer–SH -3'	50
	F_4 (B-NF)	5'-HS–Spacer–CGCAAAGA CA CTAATAACAAATTC -3'	99.5	5'-HS–Spacer–TTACTACA CTGTCACTGATCATCGCATG CTATAC–biotin -3'	0.5

Figure 3

Logic Circuit	NP	Ligand		Linker	
		Sequence	*r* (%)	Sequence	*r* (%)
Two-input Disassembly INHIBIT gate	R_1 (G-NR)	5'-CAAATAACTAATAC ACATTCATCT–Spacer–SH -3'	32.5	5'-biotin–CTCTCTGCCTCGTT CAGACAAAACTCATCCTA CT–Spacer–SH -3'	35
		5'-CATAATCTATAATC ATCCTCATAA–Spacer–SH -3'	32.5		
	F_1 (G-NF)	5'-HS–Spacer–TACTCACTATCTAAAAAC AATTAC -3'	49.75	5'-HS–Spacer–TTACTACACTG TCACTGATCATCGCATGCT ATAC–biotin -3'	0.5
		5'-HS–Spacer–CTTAGCC TAACATTTTCTAAATAC -3'	49.75		
Six-input Disassembly gate (fan-in)	R_2 (G-NR)	5'-CTATAAACTATTTC CTTTGCTATT–Spacer–SH -3'	22	5'-biotin–CTCTCTGCCTCGTT CAGACAAAACTCATCCTA CT–Spacer–SH -3'	34
		5'-CAAATAACTAATAC ACATTCATCT–Spacer–SH -3'	22		
		5'-CATAATCTATAATC ATCCTCATAA–Spacer–SH -3'	22		
	F_2 (G-NF)	5'-HS–Spacer–CGCAAAGA CA CTAATAACAAATTC -3'	33.2	5'-HS–Spacer–TTACTACACTG TCACTGATCATCGCATGCT ATAC–biotin -3'	0.4
		5'-HS–Spacer–TACTCACTAT CTAAAAACAATTAC -3'	33.2		
		5'-HS–Spacer–CTTAGCCTAA CATTTTCTAAATAC -3'	33.2		
Two-input Disassembly Gate with three	R_3 (G-NR)	5'-CAAATAACTAATAC ACATTCATCT–Spacer–SH -3'	32.5	5'-biotin–CTCTCTGCCTCGT TCAGACAAAACTCATCCT ACT–Spacer–SH -3'	35
		5'-CATAATCTATAATC ATCCTCATAA–Spacer–SH -	32.5		

outputs (fan-out)		3’			
	F$_3$ (R-NF)	5’-HS–Spacer–TACTCACTAT CTAAAAACAATTAC -3’	49.75	5’-HS–Spacer–TTACTACACT GTCACTGATCATCGCATG CTATAC–biotin -3’	0.5
		5’-HS–Spacer–CTTAGCCTAA CATTTTCTAAATAC -3’	49.75		
	F$_4$ (G-NF)	5’-HS–Spacer–TACTCACTAT CTAAAAACAATTAC -3’	49.75	5’-HS–Spacer–TTACTACACTG TCACTGATCATCGCATGCT ATAC–biotin -3’	0.5
		5’-HS–Spacer–CTTAGCCTAA CATTTTCTAAATAC -3’	49.75		
	F$_5$ (B-NF)	5’-HS–Spacer–TACTCACTAT CTAAAAACAATTAC -3’	49.75	5’-HS–Spacer–TTACTACAC TGTCACTGATCATCGCAT GCTATAC–biotin -3’	0.5
		5’-HS–Spacer–CTTAGCCTAA CATTTTCTAAATAC -3’	49.75		

Figure 4

Logic Circuit	NP	Ligand		Linker	
		Sequence	*r* (%)	Sequence	*r* (%)
AND-AND Cascade	R$_1$ (G-NR)	5’-CAAATAACTAATAC ACATTCATCT–Spacer–SH -3’	32.5	5’-biotin–CTCTCTGCCTCGTTC AGACAAAACTCATCCTACT –Spacer–SH -3’	35
		5’-CATAATCTATAATC ATCCTCATAA–Spacer–SH -3’	32.5		
	F$_1$ (G-NF)	5’-HS–Spacer–TACTCACTAT CTAAAAACAATTAC -3’	33.2	5’-HS–Spacer–TTACTACACTG TCACTGATCATCGCATGCTA TAC–biotin -3’	0.4
		5’-HS–Spacer–CTTAGCCTAA CATTTTCTAAATAC -3’	33.2		
		5’-HS–Spacer–CGCAAAGACA CTAATAACAAATTC -3’	33.2		
	R$_2$ (B-NR)	5’-CTATAAACTATTTC CTTTGCTATT–Spacer–SH -3’	50	5’-biotin–CTCTCTGCCTCGTT CAGACAAAACTCATCCTAC T–Spacer–SH -3’	50
AND-OR Cascade	R$_3$ (B-NR)	5’-CATAATCTATAATC ATCCTCATAA–Spacer–SH -3’	25	5’-biotin–CTCTCTGCCTCGTTC AGACAAAACTCATCCTACT –SH -3’	50
		5’-CATTATCATATAAC	25		

		TCAACGTCAC–Spacer–SH -3’			
	F$_2$ (G-NF)	5’-HS–Spacer–CTTAGCCTAA CATTTTCTAAATAC -3’	49.75	5’-HS–TTACTACACTGTCAC TGATCATCGCATGCTATAC–biotin -3’	0.5
		5’-HS–Spacer–AATCAGC ATCCTATTACATAATTC -3’	49.75		
	R$_4$ (G-NR)	5’-CTATAAACTATTTC CTTTGCTATT–Space–SH -3’	65	5’-biotin–CTCTCTGCCTCGTTC AGACAAAACTCATCCTACT –PEG$_6$–A$_{15}$–(CH$_2$)$_3$–SH -3’	35
	F$_3$ (G-NF)	5’-HS–Spacer–CGCAAAGACA CTAATAACAAATTC -3’	99.5	5’-HS–TTACTACACTGTCAC TGATCATCGCATGCTATAC–biotin -3’	0.5

Figure 5

Logic Circuit	NP	Ligand		Linker	
		Sequence	*r* (%)	Sequence	*r* (%)
Multiplexer	R$_1$ (B-NR)	5’-HS–Spacer–CGCAAAGACA CTAATAACAAATTC -3’	32.5	5’-HS–TTACTACACTGTCA CTGATCATCGCATGCTATAC –biotin -3	35
		5’-HS–Spacer–CTGCACATTA GTATTAGTTATTTG	32.5		
	F$_1$ (G-NF)	5’-CTATAAACTATTTC CTTTGCTATT–Spacer–SH -3’	49.75	5’-biotin–CTCTCTGCCTCGTT CAGACAAAACTCATCCTAC T–SH -3’	0.5
		5’-GTAATTGTTTTTAG TATTCTTCTC–Spacer–SH -3’	49.75		
	R$_2$ (G-NR)	5’-CAAATAACTAATAC ACATTCATCT–Spacer–SH -3’	32.5	5’-biotin–CTCTCTGCCTCGTTC AGACAAAACTCATCCTACT –SH -3’	35
		5’-CATAATCTATAATCATCCT CATAA–Spacer–SH -3’	32.5		
	F$_2$ (G-NF)	5’-HS–Spacer–TACTCACTAT CTAAAAACAATTAC -3’	49.75	5’-HS–TTACTACACTGTCA CTGATCATCGCATGCTATAC –biotin -3	0.5
		5’-HS–Spacer–CTTAGCCTAA CATTTTCTAAATAC -3’	49.75		

Figure S10B

Logic Circuit	NP	Ligand		Linker	
		Sequence	*r* (%)	Sequence	*r* (%)
Two-input Assembly AND gate	R_1 (G-NR)	5’-HS–Spacer–ACTTCACAA AGTGTACTTGTAGATTC CAAATCTACTACAAGTAC ACT TTG -3’	65	5’- HS–Spacer– TTACTACACTG TCACTGATCATCGCATGCTA TAC–biotin -3’	35
	F_1 (G-NF)	5’-HS–Spacer–CTTCTAAAG TACACTTTGTAGGATTTC CAACTAACCTACAAAGT GTACTT -3’	49.75	5’- HS–Spacer– TTACTACACTG TCACTGATCATCGCATGCTA TAC–biotin -3’	0.5
		5’-HS–Spacer– CTTAGCCTAA CATTTTCTAAATAC -3’	49.75		

Figure S10C

Logic Circuit	NP	Ligand		Linker	
		Sequence	r (%)	Sequence	r (%)
Two-input Assembly AND gate	R_1 (G-NR)	5’-CATAATCTATAATC ATCCTCATAA–Spacer–SH -3’	65	5’- biotin– CTCTCTGCCTCGTT CAGACAAAACTCATCCTAC T–Spacer–SH -3’	35
	F_1 (G-NF)	5’- HS–Spacer–CTTCTA AAG TAC ACTTTG TAGG ATTTC CAACT AA CCTA CAAAGT GTA CTT -3’	49.75	5’- HS–Spacer– TTACTACACTG TCACTGATCATCGCATGCTA TAC–biotin -3’	0.5
		5’- HS–Spacer– CTTAGCCTAA CATTTTCTAAATAC -3’	49.75		

Figure S12. Dual-rail NAND

Dual-rail NAND	NP	Ligand		Linker	
		Sequence	*r* (%)	Sequence	*r* (%)
Two-input Assembly OR (Y^0)	R_1 (B-NR)	5’-CATAATCTATAATC ATCCTCATAA–Spacer–SH -3’	25	5’- biotin– CTCTCTGCCTCGTT CAGACAAAACTCATCCTAC T–Spacer–SH -3’	50
		5’-CATTATCATATAACTCA ACGTCAC–Spacer–SH -3’	25		
	F_1 (G-NF)	5’- HS–Spacer– CTTAGCCTAA CATTTTCTAAATAC -3’	49.75	5’- HS–Spacer– TTACTACACTG TCACTGATCATCGCATGCTA TAC–biotin -3’	0.5
		5’-HS–Spacer–AATCAGCA TCCTATTACATAATTC -3’	49.75		

Two-input Disassembly OR (Y^1)	R_2 (G-NR)	5’-CTATAAACTATTTC CTTTGCTATT–Spacer–SH -3’	32.5	5’- biotin–CTCTCTGCCTCGTT CAGACAAAACTCATCCTACT–Spacer–SH -3’	35
		5’-CAAATAACTAATAC ACATTCATCT–Spacer–SH -3’	32.5		
	F_2 (G-NF)	5’- HS–Spacer–CGCAAAGAC A CTAATAACAAATTC -3’	49.75	5’- HS–Spacer–TTACTACACTG TCACTGATCATCGCATGCTATAC–biotin -3’	0.5
		5’- HS–Spacer–TACTCACTAT CTAAAAACAATTAC -3’	49.75		

Figure S16A. OR-AND Cascade

Logic Circuit	NP	Ligand		Linker	
		Sequence	*r* (%)	Sequence	*r* (%)
OR-AND Cascade	R_1 (G-NR)	5’-CATAATCTATAATC ATCCTCATAA–Spacer–SH -3’	65	5’- biotin– CTCTCTGCCTCGTT CAGACAAAACTCATCCTACT–Spacer–SH -3’	35
	F_1 (G-NF)	5’- HS–Spacer–CTTAGCCTAA CATTTTCTAAATAC -3’	49.75	5’- HS–Spacer–TTACTACACTG TCACTGATCATCGCATGCTATAC–biotin -3’	0.5
		5’-HS–Spacer–CGCAAAGA CA CTAATAACAAATTC -3’	49.75		
	R_2 (B-NR)	5’-CTATAAACTATTTC CTTTGCTATT–Spacer–SH -3’	50	5’- biotin– CTCTCTGCCTCGTT CAGACAAAACTCATCCTACT–Spacer–SH -3’	50

Figure S16B. INHIBIT-AND Cascade

Logic Circuit	NP	Ligand		Linker	
		Sequence	*r* (%)	Sequence	*r* (%)
INHIBIT-AND Cascade	R_1 (G-NR)	5’-CAAATAACTAATAC ACATTCATCT–Spacer–SH -3’	32.5	5’- biotin–CTCTCTGCCTCGTT CAGACAAAACTCATCCTACT–Spacer–SH -3’	35
		5’-CATAATCTATAATC ATCCTCATAA–Spacer–SH -3’	32.5		
	F_1 (G-NF)	5’-HS–Spacer–TACTCACTAT CTAAAAACAATTAC -3’	33.2	5’- HS–Spacer–TTACTACACTG TCACTGATCATCGCATGCTATAC–biotin -3’	0.4
		5’-HS–Spacer–CTTAGCCTAA CATTTTCTAAATAC -3’	33.2		
		5’-HS–Spacer–CGCAAAGA	33.2		

		CA CTAATAACAAATTC -3’			
	R_2 (B-NR)	5’-CTATAAACTATTTC CTTTGCTATT–Spacer–SH -3’	50	5’- biotin– CTCTCTGCCTCGTT CAGACAAAACTCATCCTAC T–Spacer–SH -3’	50

Figure S17. OR-OR Cascade

Logic Circuit	NP	Ligand		Linker	
		Sequence	r (%)	Sequence	r (%)
OR-OR Cascade	R_1 (B-NR)	5’-CATAATCTATAATC ATCCTCATAA–Spacer–SH -3’	50	5’- biotin– CTCTCTGCCTCGT TCAGACAAAACTCATCCTA CT–Spacer–SH -3’	50
	F_1 (G-NF)	5’-HS–Spacer–CTTAGCCTAA CATTTTCTAAATAC -3’	99.5	5’- HS–Spacer–TTACTACACTG TCACTGATCATCGCATGCTA TAC–biotin -3’	0.5
	R_2 (G-NR)	5’-CATTATCATATAAC TCA ACGTCAC–Spacer–SH -3’	65	5’- biotin– CTCTCTGCCTCGT TCAGACAAAACTCATCCTA CT–Spacer–SH -3’	35
	F_2 (G-NF)	5’-HS–Spacer–AATCAGC ATC CTATTACATAATTC -3’	99.5	5’- HS–Spacer–TTACTACACTG TCACTGATCATCGCATGCTA TAC–biotin -3’	0.5

Table S3. DNA sequences and experimental conditions used in logic circuit operations. Sequences are written in a 5’ → 3’ direction.

Figure 1

Logic Circuit	Input			Pre-dimerization	
	Name	Sequence	Condition	Sequence	Condition
Single-input Assembly YES gate	X_a	GAAATAGTTTATAG CTGCGACTGT GAATTTGTTATTAG	20 nM, 15 min	N/A	
Single-input Disassembly YES gate	X_d	CTAATAACAAATTC ACAGTCGCAG CTATAAACTATTTC	500 nM, 15 min	GAAATAGTTTATAG CTGCGACTGT GAATTTGTTATTAG	10 nM, 15 min

Figure 2

Logic Circuit	Input	Pre-dimerization

	Name	Sequence	Condition	Sequence	Condition
Two-input Assembly AND gate	X_1	AGTTGGAAAT CCTACAAAGTGTA	100 nM, 30 min	N/A	
	X_2	GATTTGGAAT CTACAAGTACACT	100 nM, 30 min		
	X_{ext} (Figure S10)	GATTATAGATTATG TGTTAGCTGTGTA TTTAGAAAATG	10 nM		
Two-input Assembly OR gate	X_3	GTATTAGTTATTTG TAGACGTAGG GTAATTGTTTTTAG	40 nM, 20 min	N/A	
	X_4	GATTATAGATTATG TGTTAGCTGTGTA TTTAGAAAATG	40 nM, 20 min		
Two-input Disassembly AND gate	X_5	CTAAAAACAATTAC CCTACGTCTACAA ATAACTAATAC	500 nM, 15 min	GTATTAGTTATTTG TAGACGTAGGGT AATTGTTTTTAG	40 nM, 15 min
	X_6	CATTTTCTAAATAC ACAGCTAACACAT AATCTATAATC	500 nM, 15 min	GATTATAGATTATG TGTTAGCTGTGTA TTTAGAAAATG	40 nM, 15 min
Two-input Disassembly OR gate	X_7	CTAATAACAAATTC CTCACGAACT	500 nM, 15 min	GAAATAGTTTATAG CTGCGACTGTAGT TCGTGAGGAATTT GTTATTAG	10 nM, 15 min
	X_8	ACAGTCGCAG CTATAAACTATTTC	500 nM, 15 min		

Figure 3

Logic Circuit	Input			Pre-dimerization	
	Name	Sequence	Condition	Sequence	Condition
Two-input Disassembly INHIBIT gate	X_1	CTAAAAACAATTAC CCTACGTCTA CAAATAACTAATAC	200 nM, 15 min	GTATTAGTTATTTG TAGACGTAGG GTAATTGTTTTTAG	10 nM, 15 min
	X_2	GATTATAGATTATG TGTTAGCTGT GTATTTAGAAAATG	100 nM, 15 min		
Six-input Disassembly	X_3	CTAATAACAAATTC CTCACGAACT	200 nM, 15 min	GAAATAGTTTATAG CTGCGACTGT	20 nM, 15 min

gate (fan-in)	X_4	ACAGTCGCAG CTATAAACTATTTC	200 nM, 15 min	AGTTCGTGAG GAATTTGTTATTAG	
	X_5	CTAAAAACAATTAC CCTACGTCTA	200 nM, 15 min	GTATTAGTTATTTG GAAGTGTATT TAGACGTAGG GTAATTGTTTTTAG	20 nM, 15 min
	X_6	AATACACTTC CAAATAACTAATAC	200 nM, 15 min		
	X_7	CATTTTCTAAATAC ACAGCTAACA	200 nM, 15 min	GATTATAGATTATG TGGGATCTGT TGTTAGCTGT GTATTTAGAAAATG	20 nM, 15 min
	X_8	ACAGATCCCA CATAATCTATAATC	200 nM, 15 min		
Two-input Disassembly Gate with three outputs (fan-out)	X_9	CTAAAAACAATTAC CCTACGTCTA CAAATAACTAATAC	500 nM, 15 min	GTATTAGTTATTTG TAGACGTAGG GTAATTGTTTTTAG	40 nM, 15 min
	X_{10}	CATTTTCTAAATAC ACAGCTAACA CATAATCTATAATC	500 nM, 15 min	GATTATAGATTATG TGTTAGCTGT GTATTTAGAAAATG	40 nM, 15 min

Figure 4

Logic Circuit	Input			Pre-dimerization	
	Name	Sequence	Condition	Sequence	Condition
AND-AND Cascade (X_1 AND X_2) AND X_3	X_1	CTAAAAACAATTAC CCTACGTCTA CAAATAACTAATAC	500 nM, 30 min	GTATTAGTTATTTG TAGACGTAGG GTAATTGTTTTTAG	40 nM, 15 min
	X_2	CATTTTCTAAATAC ACAGCTAACA CATAATCTATAATC	500 nM, 30 min	GATTATAGATTATG TGTTAGCTGT GTATTTAGAAAATG	40 nM, 15 min
	X_3	GAAATAGTTTATAG CTGCGACTGT GAATTTGTTATTAG	100 nM, 30 min	N/A	
AND-OR Cascade (X_4 AND X_5) OR X_6	X_4	CATTTTCTAAATAC ACAGCTAACA CATAATCTATAATC	500 nM, 15 min	GATTATAGATTATG TGTTAGCTGT GTATTTAGAAAATG	40 nM, 15 min
	X_5	CTATTACATAATTC TGCATTCTTC CATTATCATATAAC	500 nM, 15 min	GTTATATGATAATG GAAGAATGCA GAATTATGTAATAG	40 nM, 15 min
	X_6	CTAATAACAAATTC ACAGTCGCAG CTATAAACTATTTC	500 nM, 15 min	GAAATAGTTTATAG CTGCGACTGT GAATTTGTTATTAG	10 nM, 15 min

Figure 5

Logic Circuit	Input			Pre-dimerization	
	Name	Sequence	Condition	Sequence	Condition
Multiplexer	X_1	CTAATAACAAATTC ACAGTCGCAG CTATAAACTATTTC	200 nM, 15 min	GAAATAGTTTATAG CTGCGACTGT GAATTTGTTATTAG	10 nM, 15 min
	X_2	CATTTTCTAAATAC ACAGCTAACA CATAATCTATAATC	500 nM, 15 min	GATTATAGATTATG TGTTAGCTGT GTATTTAGAAAATG	40 nM, 15 min
	Selector	TACTCACTAT CTAAAAACAATTA C CCTACGTCTA CAAATAACTAATAC	500 nM, 15 min	GTATTAGTTATTTG TAGACGTAGG GTAATTGTTTTTAG ATAGTGAGTA (Sel*)	40 nM, 15 min
				GTAATTGTTTTTAG (F_2 protection)	20 nM, 15 min

Figure S10

Logic Circuit	Input			Pre-dimerization	
	Name	Sequence	Condition	Sequence	Condition
Two-input Assembly AND	X_1	AGTTGGAAATCCT ACAAAGTGTA	100 nM, 15 min	N/A	
	X_2	GATTTGGAATCTAC AAGTACACT	100 nM, 15 min		
	X_3 (Simple hybridization)	GATTATAGATTATG TGTTAGCTGT GTAT TTAGAAAATG	10 nM 15 min		

Figure S12. A dual-rail NAND gate.

Dual-rail NAND	Operation (input)			Pre-dimerization	
	Name	Sequence	Condition	Sequence	Condition
Two-input Assembly OR (Y^0)	X_1^1	GATTATAGATTATG TGTTAGCTGT GTATTTAGAAAATG	50 nM, 10 min	N/A	

	X_2^1	GTTATATGATAATG GAAGAATGCA GAATTATGTAATAG	50 nM, 10 min		
Two-input Disassembly OR (Y^1)	X_1^0	CTAATAACAAATTC ACAGTCGCAG CTATAAACTATTTC	500 nM, 10 min	GAAATAGTTTATAG CTGCGACTGT GAATTTGTTATTAG	40 nM, 15 min
	X_2^0	CTAAAAACAATTAC CCTACGTCTA CAAATAACTAATAC	500 nM, 10 min	GTATTAGTTATTTG TAGACGTAGG GTAATTGTTTTTAG	40 nM, 15 min

Figure S16A. OR-AND Cascade.

Logic Circuit	Input			Pre-dimerization	
	Name	Sequence	Condition	Sequence	Condition
OR-AND Cascade (X_1 OR X_2) AND X_3	X_1	CATTTTCTAAATAC ACAGCTAACA	500 nM, 15 min	GATTATAGATTATG TGGGATCTGT TGTTAGCTGT GTATTTAGAAAATG	10 nM, 15 min
	X_2	ACAGATCCCA CATAATCTATAATC	500 nM, 15 min		
	X_3	GAAATAGTTTATAG CTGCGACTGT GAATTTGTTATTAG	100 nM, 15 min	N/A	

Figure S16B. INHIBIT-AND Cascade

Logic Circuit	Input			Pre-dimerization	
	Name	Sequence	Condition	Sequence	Condition
INHIBIT-AND Cascade (X_4 AND NOT X_5) AND X_6	X_4	CTAAAAACAATTAC CCTACGTCTA CAAATAACTAATAC	200 nM, 15 min	GTATTAGTTATTTG TAGACGTAGG GTAATTGTTTTTAG	10 nM, 30 min
	X_5	GATTATAGATTATG TGTTAGCTGT GTATTTAGAAAATG	100 nM, 15 min	N/A	
	X_6	GAAATAGTTTATAG CTGCGACTGT GAATTTGTTATTAG	100 nM, 15 min		

Figure S17. OR-OR Cascade

Logic Circuit	Input			Pre-dimerization	
	Name	Sequence	Condition	Sequence	Condition
OR-OR Cascade (X_1 OR X_2) OR X_3	X_1	CATTTTCTAAATAC ACAGCTAACA	500 nM, 15 min	GATTATAGATTATG TGGGATCTGT TGTTAGCTGT GTATTTAGAAAATG	10 nM, 15 min
	X_2	ACAGATCCCA CATAATCTATAATC	500 nM, 15 min		
	X_3	CTATTACATAATTC TGCATTCTTC CATTATCATATAAC	500 nM, 15 min	GTTATATGATAATG GAAGAATGCA GAATTATGTAATAG	10 nM, 15 min

3.6. References

1. M. Prakash, N. Gershenfeld, *Science*. 315, 832–835 (2007).
2. M. P. Nikitin, V. O. Shipunova, S. M. Deyev, P. I. Nikitin, *Nat. Nanotechnol.* **9**, 716–722 (2014).
3. G. Gines *et al.*, *Nat. Nanotechnol.* **12**, 351–359 (2017).
4. R. Yashin, S. Rudchenko, M. N. Stojanovic, *J. Am. Chem. Soc.* **129**, 15581–15584 (2007).
5. Y. Benenson, *Nat. Rev. Genet.* **13**, 455–468 (2012).
6. E. Katz, V. Privman, *Chem. Soc. Rev.* **39**, 1835–1857 (2010).
7. G. Seelig, D. Soloveichik, D. Y. Zhang, E. Winfree, *Science*. **314**, 1585–1588 (2006).
8. L. Qian, E. Winfree, *Science*. **332**, 1196–1201 (2011).
9. A. A. Green *et al.*, *Nature*. **548**, 117–121 (2017).
10. G. Chatterjee, N. Dalchau, R. A. Muscat, A. Phillips, G. Seelig, *Nat. Nanotechnol.* **12**, 920–927 (2017).
11. M. N. Stojanovic, D. Stefanovic, **21**, 1069–1074 (2003).
12. A. J. Genot, J. Bath, A. J. Turberfield, *J. Am. Chem. Soc.* **133**, 20080–20083 (2011).
13. N. V. DelRosso, S. Hews, L. Spector, N. D. Derr, *Angew. Chem. Int. Ed.* **56**, 4443–4446 (2017).
14. W. Engelen, L. H. H. Meijer, B. Somers, T. F. A. de Greef, M. Merkx, *Nat. Commun.* **8**, 14473 (2017).
15. A. P. de Silva, S. Uchiyama, *Nat. Nanotechnol.* **2**, 399–410 (2007).
16. A. Kumar, S. Kim, J.-M. Nam, *J. Am. Chem. Soc.* **138**, 14509–14525 (2016).
17. H. Wang, D. W. Brandl, P. Nordlander, N. J. Halas, *Acc. Chem. Res.* **40**, 53–62 (2007).
18. B. Shi, B. Zhou, D. Jin, X. Liu, *Nat. Nanotechnol.* **10**, 924–936 (2015).
19. A. S. Urban *et al.*, *Nano Lett.* **9**, 2903–2908 (2009).
20. L. Liu, A. Corma, *Chem. Rev.* **118**, 4981–5079 (2018).
21. L. H. Reddy, J. L. Arias, J. Nicolas, P. Couvreur, *Chem. Rev.* **112**, 5818–5878 (2012).
22. Y. Yan, S. C. Warren, P. Fuller, B. A. Grzybowski, *Nat. Nanotechnol.* **11**, 603–608 (2016).
23. D. V. Talapin, J.-S. Lee, M. V. Kovalenko, E. V. Shevchenko, *Chem. Rev.* **110**, 389–458 (2010).
24. T. Song, H. Liang, *J. Am. Chem. Soc.* **134**, 10803–10806 (2012).
25. D. Liu *et al.*, *Angew. Chem. Int. Ed.* **50**, 4103–4107 (2011).
26. M. Motornov *et al.*, *Nano Lett.* **8**, 2993–2997 (2008).
27. G. von Maltzahn *et al.*, *J. Am. Chem. Soc.* **129**, 6064–6065 (2007).
28. J. Liu, Y. Lu, *Adv. Mater.* **18**, 1667–1671 (2006).
29. S. Angelos, Y.-W. Yang, N. M. Khashab, J. F. Stoddart, J. I. Zink, *J. Am. Chem. Soc.* **131**, 11344–11346 (2009).
30. R. Freeman, T. Finder, I. Willner, *Angew. Chem. Int. Ed.* **121**, 7958–7961 (2009).
31. D. Bray, *Nature*. **376**, 307–312 (1995).
32. D. Bray, *J. Theor. Biol.* **143**, 215–231 (1990).
33. Y. E. Antebi *et al.*, *Cell*. **170**, 1184-1196.e24 (2017).
34. K. Salaita *et al.*, *Science*. **327**, 1380–1385 (2010).
35. D. Y. Zhang, G. Seelig, *Nat. Chem.* **3**, 103–113 (2011).
36. S. Kim *et al.*, *J. Am. Chem. Soc.* **139**, 3558–3566 (2017).
37. R. Klajn, J. F. Stoddart, B. A. Grzybowski, *Chem. Soc. Rev.* **39**, 2203–2237 (2010).
38. M. Langecker, V. Arnaut, J. List, F. C. Simmel, *Acc. Chem. Res.* **47**, 1807–1815 (2014).
39. S. Ohta, D. Glancy, W. C. W. Chan, *Science*. **351**, 841–845 (2016).
40. C. Jung, P. B. Allen, A. D. Ellington, *Nat. Nanotechnol.* **11**, 157–163 (2016).
41. K. P. Adamala, D. A. Martin-Alarcon, K. R. Guthrie-Honea, E. S. Boyden, *Nat. Chem.* **9**, 431–439 (2017).

42. S. Regot *et al.*, *Nature*. **469**, 207–211 (2011).
43. H. Ba, J. Rodríguez-Fernández, F. D. Stefani, J. Feldmann, *Nano Lett.* **10**, 3006–3012 (2010).
44. D. Y. Zhang, A. J. Turberfield, B. Yurke, E. Winfree, *Science* **318,** 1121–1125 (2007).
45. D. Y. Zhang, in *DNA Computing and Molecular Programming*, Y. Sakakibara, Y. Mi, Eds. (Springer Berlin Heidelberg, 2011), pp. 162–175.
46. J. N. Zadeh et al., *J. Comput. Chem.* **32**, 170–173 (2011).
47. Y. K. Lee, S. Kim, J.-W. Oh, J.-M. Nam, *J. Am. Chem. Soc.* **136**, 4081–4088 (2014).

Chapter 4

Development of Nanoparticle Architecture for Biomolecular Arithmetic Logic Operation

Nanoparticle-based molecular computing could potentially be utilized to sophisticate nanodevices with their multi-functionality and biomodality. However, the current form of nanoparticle-based logic gate has no universal rules or design principle, which hampers scalable, modular architecture for building complex logic circuits. Here, we developed a two-dimensional nanoparticle computing platform and algorithm, a lipid nanotablet (LNT). Three types of plasmonic nanoparticles, a mobile floater, a memory receptor, and a reporting receptor, are tethered on lipid bilayer, acting data storage device and data processing unit like a silicon-based computer chip, a microprocessor. For an operation of LNT, the memory receptor stores biomolecular information of solution onto its surface ligand through specific and noncovalent Watson-Crick base pairing. Then, the addition of software solution, comprising trapping DNA which quenches the floater to the memory quickly if and only if the condition is not satisfied, and reporting DNA which generates output signal slowly when the floater is not trapped, will generate the result of arithmetic and logic operation. The lipid nanotablet architecture is universal and scalable to construct any arbitrary logic operations (YES, NOT, AND, XOR, etc) in a single chip and further application for arithmetic operation. This LNT shows the potential application of complex multicomponent biocomputing devices and smart diagnosis sensors.

The version presented in this chapter is not a final manuscript. This work is in preparation for submission.

4.1. Introduction

Biomolecular mechanism for information processing is fundamental and crucial for living cells to survive and interact with their environment. The synthetic biomolecular systems, especially with DNA, for biomolecular computing, has attracted great attention with their powerful programmability because of Watson-Crick base pairing, showing diverse bioapplication including Hamiltonian path finding, toe-hold displacement mediated logic circuit operation, and building an artificial neural network for molecular pattern recognition. (1-3) Recently, colloidal gold nanoparticles and quantum dots are introduced in molecular computing with their diverse physical, and optical properties. (4,5) However, the nanoparticle-based computing systems receive their input signal in the form of molecules, and generate output signal in the form of optical response. (6-9) This mismatched form of the input and the output signal significantly restrict the scalable design of logic circuits. Further, each logic gate requires a different form of molecular design, which also limits their boundary of computing performances.

Arithmetic logic unit (ALU) is a fundamental part of central processing unit (CPU) that carries out arithmetic and logic operations. Since the first development of single ALU chip in 1960s, modern silicon-based computer chips rely on powerful and complex ALU and the computing power has soared over the year. ALU performs specific logical or arithmetic operations based on the operation code, called opcode. The single chip can perform diverse operations including

AND, OR, XOR, add, and subtract according to the opcode signal.

Taking inspiration from ALU in computer, here, we develop a biomolecular calculator based on two-dimensional lipid bilayer-nanoparticle architecture for arithmetic logic operations, a lipid nanotablet (LNT). (Fig. 1) Three types of plasmonic nanoparticles, a mobile floater, a memory receptor, and a reporting receptor, are tethered on lipid bilayer, acting data storage device and data processing unit like a silicon-based computer chip, a microprocessor. For an operation of LNT, the memory receptor stores biomolecular information of solution onto its surface ligand through specific and noncovalent Watson-Crick base pairing. Then, the addition of software solution, comprising trapping DNA which quenches the floater to the memory quickly if and only if the condition is not satisfied, and reporting DNA which generates output signal slowly when the floater is not trapped, will generate the result of arithmetic and logic operation. The lipid nanotablet architecture is universal and scalable to construct any arbitrary logic operations (YES, NOT, AND, OR, XOR, etc) and arithmetic operations (add, subtract, etc) in a single chip. This LNT shows the potential application of complex multicomponent biocomputing devices and smart diagnosis sensors.

4.2. Experimental Section

Preparation of Small Unilamellar Vesicles (SUVs)

The lipid in chloroform solution was mixed to have 97.2 mol% dioleoylphosphatidylcholine (DOPC), 0.3 mol% biotinylated dioleoylphosphatidylethanolamine (DOPE), and 2.5 mol% 1k poly(ethylene glycol)−DOPE. The lipid mixture was evaporated with a rotary evaporator, and the lipid film was thoroughly dried under a stream of nitrogen. The dried mixture was resuspended in deionized (DI) water with 2 mg/mL concentration and followed by three freeze−thaw cycles. The solution was extruded 11 times through a polycarbonate membrane with 100 nm pores at 35 ℃.

Preparation of supported lipid bilayers

A flow chamber was made from a top slide glass and bottom cover glass and a Parafilm spacer. The top slide glass (Paul Marienfeld GmbH) with inlet and outlet holes was cleaned by sonication in DI water for 10 min and piranha etching for 10 min. After each cleaning procedure, glass substrates were washed with DI water and then passivated with 10 mg/mL of bovine serum albumin (BSA) in 150 mM NaCl phosphate buffered saline (1× PBS) to prevent SLB formation on the upper side of the chamber. The bottom cover glass (Paul Marienfeld GmbH) was cleaned by sonication in DI water for 10 min followed by piranha etching for 10 min. A two-ply Parafilm spacer (4 mm × 50 mm × 200 μm) was then placed between the two glass slides and heat-sealed at 105 ℃. The volume of the flow chamber is ~ 40 µL. The freshly extruded SUV solution was diluted to 1 mg/mL of lipid concentration in 0.5× PBS solution and sonicated for 15 min. The vesicle solution was introduced within flow chambers and form SLBs via the vesicle fusion method. The SLBs were formed by introducing the sonicated vesicle solution into the flow chamber at 30 ℃. After 60 min, the flow chamber was gently washed with DI water and 1× PBS. Defects in SLBs were then passivated with BSA (100 µg/mL) in 1× PBS for 45 min. Streptavidin (50 nM) in 1× PBS was then injected into the flow chamber to modify the biotinylated DOPE molecules. After 60 min, the flow chamber was washed with 1× PBS.

Synthesis and functionalization of Plasmonic Nanoparticles

Spherical gold nanoparticles (50 nm) were purchased from BBI Solutions (Cardiff, UK) for nanoparticles scattering green light. Blue scattering nanoparticles were gold/silver-core/shell nanoparticles. The 20-nm gold core nanoparticles were synthesized through seed-mediated growth. The seed was synthesized by mixing 5 mL of 0.5 mM $HAuCl_4 \cdot 3H_2O$ solution with 5 mL of 0.2 M cetyltrimethylammonium bromide (CTAB), followed by rapid injection of 600 µL of ice-cooled 0.01 M $NaBH_4$ solution. The seed solution was kept for 2 h after the reducing step. A 5 mL aliquot of 0.5 mM $HAuCl_4 \cdot 3H_2O$ solution was mixed with 5 mL of 0.2 M CTAB solution, and 250 µL of 4 mM $AgNO_3$ solution was added, followed by 70 µL of 78 mM ascorbic acid solution. The silver shell was formed by rapidly injecting ascorbic acid solution (50 µL, 100 mM) to mixture of NH_4OH (5 µL), CTAC (100 µL, 100 mM), 20-nm AuNP (5 µL), $AgNO_3$ (30 µL, 1 mM), and the color turned yellow immediately. The surfactant of synthesized gold/silver core-shell nanoparticle was exchanged from CTAB to 1% polyvinylpyrrolidone (PVP) for DNA modification.

Synthetic thiolated oligonucleotides (IDT, USA) were reduced with 100 mM dithiothreitol (DTT) in 100 mM pH 8.0 phosphate buffer (PB) solution for 1 h, and the DNA was separated with a size exclusive NAP-5 column (GE Healthcare, Buckinghamshire, U.K.). The detailed sequences of thiolated oligonucleotides attached on supporting table 1. The mixture of thiolated strands at a concentration of 1 μM were incubated with 50 pM plasmonic nanoparticles for 2 h at room temperature. The solution was adjusted to 10 mM PB and 0.1% (w/v) sodium dodecyl sulfate. Two aliquots of 1 M NaCl and 0.01% sodium dodecyl sulfate (SDS) solution were added with 1 h interval between each addition to achieve a final concentration of 0.3 M for floater, reporting receptor and 0.2 M for memory receptor. The mixture was sonicated for 10 s after each salt addition. The mixture was incubated overnight at room temperature. The suspension was washed by centrifugation, the supernatant removal, and particle redispersion in 10 mM PB solution three times.

Arithmetic logic operation on lipid nanotablets

A solution containing floaters and receptors (1 to 10 pM) was introduced to an SLB-coated flow chamber. The solution was incubated from 5 to 10 min to result in a desired particle density. After the particle loading, the LNT was washed with 1× PBS. Input DNA solution (50 nM) in 250 mM PBS were incubated in the flow chamber for 30 min for memory receptors to capture the molecular inputs onto their surface and washed with 250 mM PBS. The operation solution containing operating DNAs (NOT trap DNAs, YES trap DNAs, reporting DNA) was added into the flow chamber to monitor the logic circuit performance during dark-field imaging. The circuit operation and dark-field imaging was carried out at 25 ℃ by a commercial dark-field microscope (Zeiss, Germany) with a 40× objective lens (NA 0.75) and AxiCam HRC color camera on an optical table (Dail Systems, South Korea). Circuit performance was recorded during and after input injection with imaging interval of 6 s. Images obtained from time-lapse dark-field imaging were analyzed by custom MATLAB code described in Chapter 3 to quantify how nanoparticle circuits respond to molecular inputs.

4.3. Results and Discussion

A single chip of LNT can perform any arbitrary arithmetic and logic operations based on the biomolecular input signal (Fig. 1). An SLB offers dynamic two-dimensional surface for tethered plasmonic nanoparticles with controllable mobility. The plasmonic nanoparticles are modified with several types of short oligonucleotides to interact with software DNAs and to be tethered on SLB. Nano-receptors have multiple linkages with an SLB, showing immobile characteristics, while nano-floaters have one or few linkages with an SLB, showing highly mobile trajectories. There are three types of plasmonic nanoparticles based on their functions for arithmetic logic operation, i) a memory receptor ii) a nano-floater, and iii) a reporting receptor.

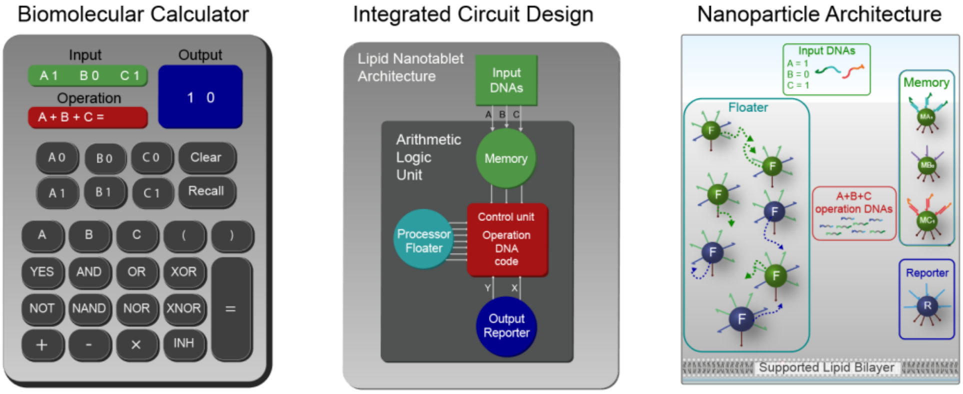

Fig. 1. Biomolecular calculator for arithmetic logic unit on lipid nanotablet (LNT). To operate biomolecular calculator, nanoparticles are encoded with specific functions, such as processor, data storage device, and output unit. Single LNT composed of floater, memory receptor and reporting receptor can perform arbitrary logic circuit based on the combinations of operation DNAs.

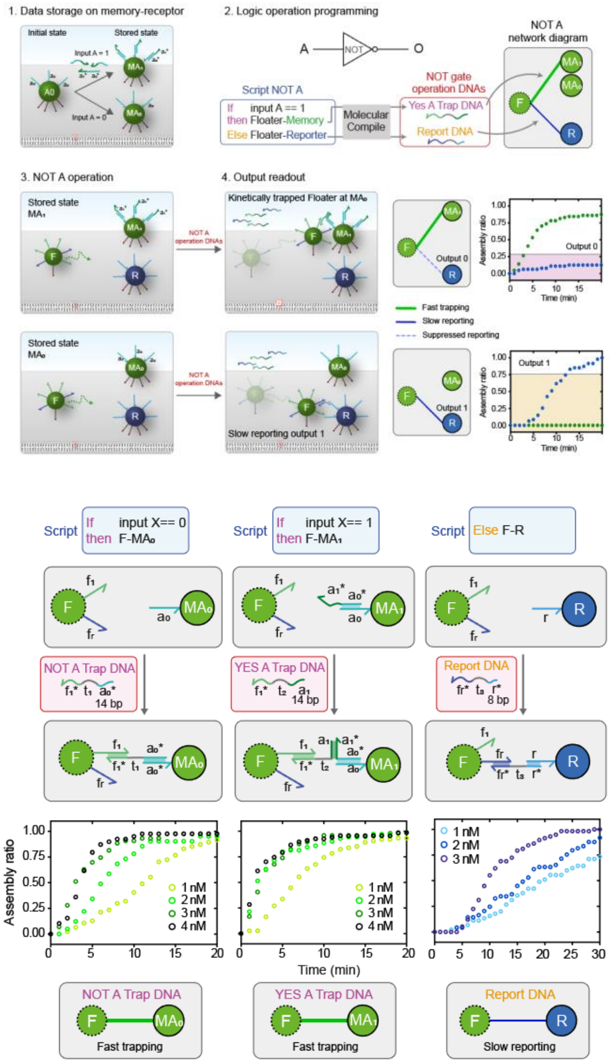

Fig. 2. ALU operation process. First, the molecular information on solution state are stored onto nanoparticle surface through specific Watson-Crick base pairing. Second, logic operations are encoded with if-then-else statement and the script is translated to molecular operation DNA state through molecular compile. Operation DNAs connects floters with receptors at specific logical state with different kinetics. The kinetic difference is induced by the number of DNA nucleotides. Trap DNAs, which binds floaters to memory, with 14 bases enable faster reaction than report DNA, which binds floaters to reporter, with 8 bases. The kinetic difference induces the first-searched condition (if statement) and the later searched condition (else statement) to result in specific operation.

On LNT, the memory receptors store the molecular information of the solution on the surface ligand of the memory receptors (Fig. 2). The memory receptors are modified with specific DNA sequences which can be partially hybridized to the specific DNA molecules, the inputs. If the solution containing input A is added to LNT, the single-stranded DNA domains of memory nano-receptors are changed from a0 to a1*. Through this domain representation, information processing occurs. The memory receptors are designed to stably hybridize with inputs in the reaction condition, by optimizing salting concentration and the domain length of 24 bases. (10)

After data storage, the processing nano-floater will interact with memory nano-receptor based on the added arithmetic logic operation program solution, which contains trapping DNAs and a report DNA (Fig. 2). The trapping DNA will hybridize processing nano-floater with memory nano-receptor with fast kinetics only when the trapping condition meets. For example, YES A trap DNA and NOT A trap DNA will consume more than 75% nano-floater within 5 min when input A is one and zero respectively (Fig. 2). If the logic condition is not satisfied, then there is no interaction between nano-floater and memory nano-receptor. Then the reporting DNA will slowly generate output signals of one, association event of nano-floaters and reporting nano-receptors, which can be identified by distinct scattering color change from blue to cyan.

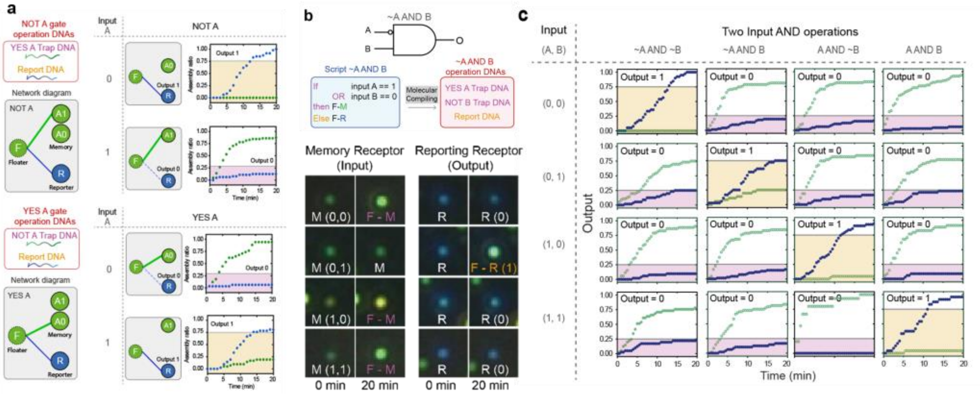

Fig. 3. (a) NOT and YES logic gate. NOT A gate operation DNAs are composed of YES A trap DNA and Report DNA and YES A gate operation DNAs are composed of NOT A trap DNA and Report DNA. If the condition is not satisfied, then the floaters are quickly consumed by memory-receptor, suppressing floater-reporting receptor interaction to yield FALSE output. (b) NOT A AND B logic gate result. Operation DNAs are composed of YES A trap, NOT B trap and report DNA. (c) Two-input AND logic gate result. Any AND logic gate can be modulary constructed by simply mixing trap and report DNAs.

Table 1. Operation DNA code for two-input logic circuit. A total of 16 logic circuits can be implemented through mixing nine operation DNAs.

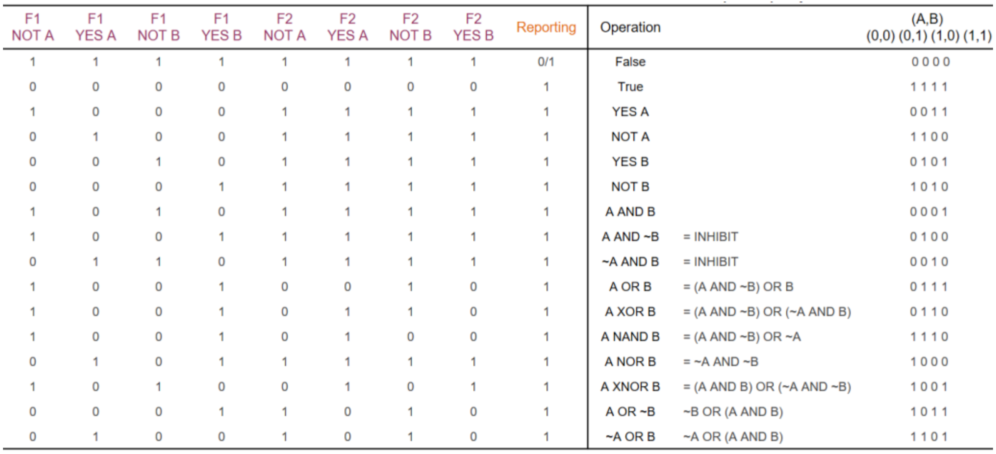

F1 NOT A	F1 YES A	F1 NOT B	F1 YES B	F2 NOT A	F2 YES A	F2 NOT B	F2 YES B	Reporting	Operation		(A,B) (0,0) (0,1) (1,0) (1,1)
1	1	1	1	1	1	1	1	0/1	False		0 0 0 0
0	0	0	0	0	0	0	0	1	True		1 1 1 1
1	0	0	0	1	1	1	1	1	YES A		0 0 1 1
0	1	0	0	1	1	1	1	1	NOT A		1 1 0 0
0	0	1	0	1	1	1	1	1	YES B		0 1 0 1
0	0	0	1	1	1	1	1	1	NOT B		1 0 1 0
1	0	1	0	1	1	1	1	1	A AND B		0 0 0 1
1	0	0	1	1	1	1	1	1	A AND ~B	= INHIBIT	0 1 0 0
0	1	1	0	1	1	1	1	1	~A AND B	= INHIBIT	0 0 1 0
1	0	0	1	0	0	1	0	1	A OR B	= (A AND ~B) OR B	0 1 1 1
1	0	0	1	0	1	1	0	1	A XOR B	= (A AND ~B) OR (~A AND B)	0 1 1 0
1	0	0	1	0	1	0	0	1	A NAND B	= (A AND ~B) OR ~A	1 1 1 0
0	1	0	1	1	1	1	1	1	A NOR B	= ~A AND ~B	1 0 0 0
1	0	1	0	0	1	0	1	1	A XNOR B	= (A AND B) OR (~A AND ~B)	1 0 0 1
0	0	0	1	1	0	1	0	1	A OR ~B	~B OR (A AND B)	1 0 1 1
0	1	0	0	1	0	1	0	1	~A OR B	~A OR (A AND B)	1 1 0 1

The nanoparticle network diagram represents the kinetics between nanoparticles. Green solid line shows fast trapping of floater to memory receptor, and blue solid line represents floaters' slow reporting to reporting receptor. If two reactions, trapping and reporting, occur together, then the slow reporting reactions are suppressed because of fast consumption of floater to memory-receptor, which cannot generate output signal. Using this kinetic difference, we can encode diverse logic operation, which generates output signal at specific logical conditions.

It is possible to program specific logic gates by the combination of trap DNAs and reporting DNA. The combination of NOT A trap DNA, NOT B trap DNA and reporting DNA will perform YES A AND YES B operation accordingly, generating output signal ("1") only when the (input A, input B) is equal to (1,1). This modular logic gate design can be examined with two-input AND gates, A AND B, and ~A AND ~B (Fig. 4). If the results of logic gate are zero, then the fast consumption of nano-floaters prohibits further generation of output signal ("1"). Although the slow reporting has suppressed by fast trapping, there is a minor leak of reporting signal that floaters assembled with reporting receptor before trapping on memory receptors.

In order to design logic gates with multiple output ("1") such as OR, XOR logic gates, OR wiring of multiple AND gates can be employed. XOR gate can be redesigned by OR wiring of (A AND ~B) and (~A AND B). On LNT chip, we can implement two different nano-floaters encoding each AND logic gate. In this case, only half of the floater will generate output one. Using this technique, any arbitrary logic circuits can be modularly designed using the multiple floaters and operation DNAs.

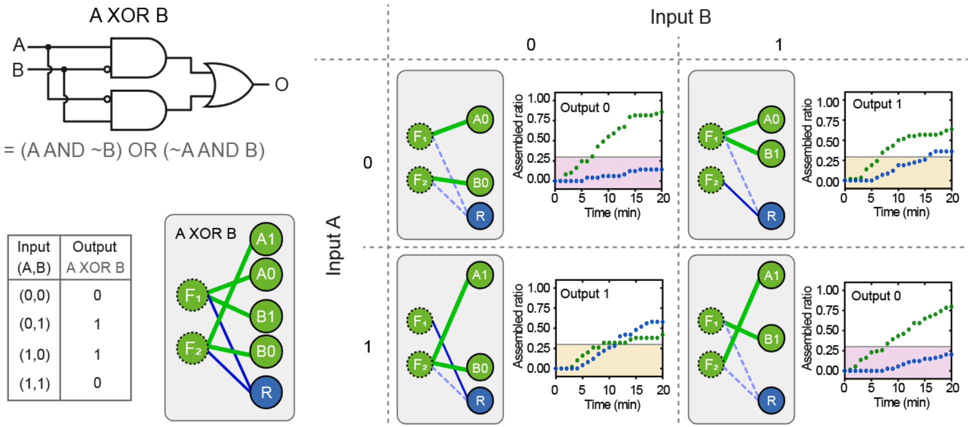

Input (A,B)	Output A XOR B
(0,0)	0
(0,1)	1
(1,0)	1
(1,1)	0

Fig. 4. XOR logic gate design based on OR wiring. The two floaters encode two AND gates, (A AND ~B), and (~A AND B), which generates output TRUE based on XOR logic operation. The combination of two different AND gates can encode any arbitrary two-input processing logic circuits.

4.4. Conclusion

In conclusion, the lipid nanotablet offers the two-dimensional platform for creating nanoparticle networks to solve logic gates and logic circuits. The clear difference between 2D nanoparticle chip of hardware and the DNA solution state of software enables the modular design of any arbitrary logic circuits in a single chip.

The n-bit molecular inputs have a total 2^n combinations of inputs, and the possible number of n-input logic circuits is 2^{2^n}. Here, I was able to operate 2^{2^2}(= 16) different logic circuit including XOR with a total of five types of nanoparticles on lipid bilayer (two floaters, two memory receptors, and one reporting receptor). This system can be readily expanded to n-input chip, composed of 2n-1 floaters, n memory receptors, and one reporting receptor, covering any logic circuit operation simply by changing the operation DNAs. The LNT system can further operate arithmetic operations such as addition, subtraction with additional floaters generating different optical signals. For example, the blue-scattering floater will generate one more output bit. The three-bit input two-bit output system can operate 2^{2n+1} numbers of arithmetic operations including full adder or full subtractor.

The reset function has been explored by DNA-based computing in solutions (11, 12), but the LNT has advantageous for reset and reoperation because of facile solution exchange on flow reaction chamber where the computing chips are tethered on the bottom surface. The logic operations and data storages depend on the non-covalent DNA hybridization, which enables reset and reuse by detaching all dangling DNAs on nanoparticles. By lowering the salt concentration and increase the temperature over DNA melting temperatures will detach all the DNAs and the LNT nanochip can easily reset to the initial state and reused for multiple times. The nanoparticle architecture has modular and scalable design that can further develop any operation with multiple times with diverse functions like electronic calculator, which can be further used for intelligent nano-computing device for diagnosis and prognosis.

4.5. References

1. Adleman, L. M.. *Science* **266**, 1021–1024 (1994).
2. Qian, L.; Winfree, E. *Science* **332**, 1196–1201 (2011).
3. Cherry, K. M.; Qian, L. *Nature* **559**, 370–376 (2018).
4. Song, T; Liang, H. *J. Am. Chem. Soc.* **134**, 10803–10806 (2012).
5. Nikitin, M. P. et al. *Nature Nanotechnol.* **9**, 716–722 (2000).
6. Yao, D.; Song, T.; Sun, X.; Xiao, S.; Huang, F.; Liang, H. *J. Am. Chem. Soc.* **137**, 14107–14113 (2015).
7. Claussen, J. C.; Hildebrandt, N.; Susumu, K.; Ancona, M. G.; Medintz, I. L., *ACS Appl. Mater. Interfaces* **6**, 3771–3778 (2014).
8. Song, T.; Liang, H., *J. Am. Chem. Soc.* **134**, 10803–10806 (2012)
9. Liu Y. et al., *Chem. Commun.* **50**, 12026 (2014).
10. Randeria, P. S. et al., *J. Am. Chem. Soc.* **137**, 3486−3489 (2015).
11. Elbaz, J.; Wang, Z.-G.; Orbach, R.; Wilner, I., *Nano Lett.* **9**, 4510–4514 (2009).
12. Guz, N. et al., *ChemPhysChem* **17**, 2247–2255 (2016).

초 록

지지형 지질 이중층은 친수성 기판 위에 조립된 2차원의 지질 이중층으로 2차원 상의 유동성을 가진다. 지지형 지질 이중층에 강한 산란 신호를 지니는 플라즈모닉 나노입자를 도입하면 수천 개의 나노입자와 그 상호작용을 단일 나노입자 수준으로 실시간 관찰이 가능하다. 본 학위논문에서는 나노입자-지질 이중층 플랫폼에서의 나노입자 종류 및 개질 방법을 확장하여 복잡한 나노입자 네트워크 시스템을 구성하고, 바이오 검지, 바이오 컴퓨팅 응용을 개발한다.

1장에서는 플라즈모닉 나노입자가 도입된 지지형 지질 이중층 플랫폼을 설명한다. 1절에서 플라즈모닉 나노입자의 광학적 특성과 산란신호를 이용한 바이오센싱 응용 연구를 소개하고 2절에서는 지지형 지질 이중층 플랫폼에 나노입자의 도입 방법, 특징, 장점, 분석방법 등을 소개한다. 2장에서는 빨강, 초록, 파랑 빛을 산란하는 플라즈모닉 나노입자를 합성하고, 지지형 지질 이중층에 도입하여 동시에 일어나는 9종류의 나노입자 결합 반응을 각각 구분할 수 있는 플랫폼을 개발한다. 이를 이용하여 세포 내 중요한 단백질 번역 조절물질이자 암 바이오마커인 마이크로RNA를 동시 다중 검지한다. 3장에서는 지지형 지질 이중층 상에 도입된 나노입자를 다종의 DNA로 기능화하여 특정 DNA 분자 입력 신호 인식, 논리회로 수행, 나노입자 결합/분리 출력 신호 생성하는

바이오 컴퓨팅 플랫폼을 개발한다. 나노입자의 계면을 DNA로 디자인하여 논리 회로를 구성하는 인터페이스 프로그래밍과 나노입자의 결합/분리 반응을 연결하여 네트워크를 디자인하여 논리 회로를 집적하는 네트워크 프로그래밍을 조합하여 복잡한 논리 회로를 설계하고 수행한다. 4장에서는 지지형 지질 이중층에 도입된 나노입자 표면에 용액상 분자 입력신호를 저장하는 정보 저장 장치를 개발하고 모든 종류의 산술논리연산을 수행할 수 있는 생분자 계산기을 개발한다. 나노입자-지질 이중층 플랫폼을 정보저장, 수행, 출력하는 매체인 하드웨어로 이용하고, DNA 분자 조합 용액을 산술논리회로 기능을 담고있는 소프트웨어로 구성한다. 바이오 컴퓨팅 칩은 DNA 정보로 프로그래밍된 산술논리회로를 인식하여 입력신호의 저장 상태에 따라 나노입자 결합 반응에 반응속도에 차이를 일으키고 결과를 출력한다.

주요어 : 지지형 지질 이중층, 플라즈모닉 나노입자, 다중 검지, 분자 컴퓨팅, 나노입자 네트워크

학 번 : 2013-20258